Charles University in Prague
Faculty of Mathematics and Physics

RIGOROUS THESIS

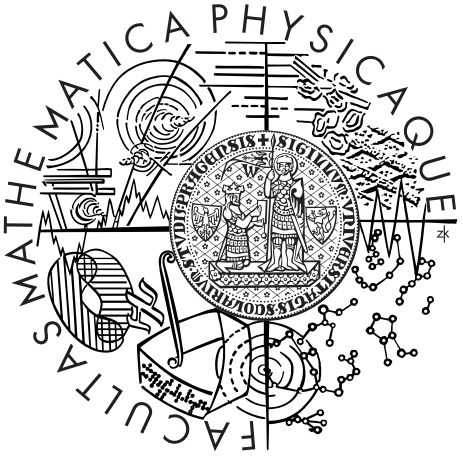

Hana Šustková

Viscoelastic properties of ferrofluid – Study of normal stresses differences

Department of Condensed Matter Physics

Supervisor of the rigorous thesis:

Study programme: Physics

Specialization: Physics of Condensed Matter and Materials

Prague 2013

I would like to thank heartfully to Mr. Doc. Ivan Krakovský, for the support, assistance and advice whenever it was needed. My great thanks belong as well to my university for the friendly help and advice of the teachers and reasearches of the Charles University in Prague whenever I asked. Even the creative environment at our university I would like to highlight for its unrepeatable value.

But next to that I would like to express my deepest thanks to the Technical University Dresden, especially to the Mr. Prof. Stefan Odenbach, Mr. Dr. Dmitry Borin and the whole Chair of the Magnetofluiddynamics, for the possibility to study, measure, work and finally develope my master thesis there. I cannot express my true thanks, pleasure and appreciation. The space offered by the Chair of the Magnetofluiddynamics and the scientific, study and friendly hinterland cannot be circumscribed by any words. Please accept my honest thanks to you.

I declare that I carried out this master thesis independently, and only with the cited sources, literature and other professional sources.

I understand that my work relates to the rights and obligations under the Act No. 121/2000 Coll., the Copyright Act, as amended, in particular the fact that the Charles University in Prague has the right to conclude a license agreement on the use of this work as a school work pursuant to Section 60 paragraph 1 of the Copyright Act.

In Prague the 22nd August 2013 signature

Název práce: Viskoelastické vlastnosti ferrokapaliny – Studium normálových napětí

Autor: Hana Šustková

Katedra/Ústav: Katedra fyziky kondenzovaných látek

Vedoucí rigorózní práce:

Konzultanti rigorózní práce:
Prof. Dr. rer. nat. habil. Stefan Odenbach
Dr.Dmitry Borin
Professur für Magnetofluiddynamik, Technische Universität Dresden

Abstrakt:
Od roku 1960 je známa ferrokapalina, specificky reagující na magnetické pole. Ferrokapalina je koloidní kapalina tvořená ferro- či ferrimagnetickými nanočásticemi rozptýlenými v základové kapalině. Základová kapalina bývá nejčastěji na bázi vody, oleje nebo organických rozpouštědel. Každá nanočástice s rozměry kolem 10-20 nm bývá pokryta ochrannou vrstvou proti shlukování částic. Ferrokapalina obvykle nezůstává zmagnetována po vypnutí vnějšího magnetického pole, proto se řadí spíše mezi superparamagnetika. Tato práce studuje viskoelastické vlastnost vybrané ferrokapaliny APG513a – vlastností v ustáleném stavu a dynamickém režimu v porovnání se standartní kapalinou (základová kapalina a pod.) a MR kapalinou. K provedení experimentu byla navržena a zkonstruována magnetická cela pro použitý reometr, celý systém byl zkalibrován a byly provedeny experimenty s ferrokapalinou, MR kapalinou a referenční kapalinou.

Práce se nejvíce zaměřuje na problematiku rozdílů normálových napětí (N1, N2) ve ferrokapalině, které doposud na této kapalině studovány nebyly. Dle odvozeného modelu pro použitou měřicí geometrii lze očekávat, že jsou průběhy N1 a N2 silně závislé na magnetickém poli; tyto vlastnosti byly také experimentálně ověřeny. Jedná se tedy o první práci tohoto druhu. Rozdíl normálových napětí byl zjištěn přímo nebo nepřímo pomocí aplikace Launova pravidla. Ferrokapalina se chovala velmi anizotropně pro různé směry měření pro smykový experiment. Vlastnost shear-thinningu ferrokapaliny v normálovém směru k prováděnému smykovému experimentu byla mnohem silnější než ve směru smyku. V dynamickém režimu ferrokapalina sleduje obdobu časově teplotní superpozice a stává se pro vyšší frekvence dle komplexní viskozity shear-thickening, což je v kontrastu s měřeními v ustáleném stavu. Creep obsahoval informace o delších relaxačních časech, které odpovídají relaxaci kratších segmentů řetězce v kapalině, vytvořeného působením magnetického pole. Viskozita odpovídala ustálenému smykovému experimentu.

Klíčová slova: viskoelasticita; ferrokapaliny

Title: Viscoelastic properties of ferrofluid – Study of normal stresses differences

Author: Hana Šustková

Department: Department of Condensed Matter Physics

Supervisor:

Consultants:
Prof. Dr. rer. nat. habil. Stefan Odenbach
Dr.Dmitry Borin
Professur für Magnetofluiddynamik, Technische Universität Dresden

Abstract:

Since 1960, a liquid becoming strongly magnetized in the presence of a magnetic field, called ferrofluid, is known. This colloidal liquid made of ferro- or ferrimagnetic nanoparticles, with diameter in range 10-20 nm, suspended in a carrier fluid. This work focuses on the study of the viscoelastic properties of a selected ferrofluid – the steady-state and dynamic properties of the fluid with comparison to a standard fluid (basis fluid, etc.) and a MR fluid. Rheological measurements are carried out using a commercial rheometer. A magnetic cell for this rheometer is designed and built. In this magnetic cell the experiments are realized, the whole system is calibrated and the experiments performed. The ferrofluid APG513a, MR-fluid and reference fluid were used.

Study of normal stresses differences (N1,N2) in liquids is carried out. According to derived theoretical model, the course of N1 and N2 should be strongly dependent on the field – this was studied directly by measuring of the normal forces or indirectly applying the Laun's rule. A good accordance of theory and experiment was found and an anisotropic behaviour of ferrofluid was studied. The shear-thinning ability of the ferrofluid in normal direction for shear experiment is found to be much stronger than in shear direction. In dynamical mode, the ferrofluid in magnetic field behaves similarly according to time-temperature superposition principle - a shift factor according to WLF theory can be found for time-magnetic field superposition. The fluid becomes shear-thickening according to complex viscosity for higher frequencies which is in contrast to steady-state measurements. A creep experiments contain an information about longer relaxation times which corellates with relation of shorter parts of the built chains. Viscosity in teh creep experiment was comparable to steady-state shear mode.

Keywords: viscoelasticity; ferrofluids

Contents

Introduction

Dating back to the 1960s, the dispersion of nanosized ($\approx$ 10 nm in diameter) ferromagnetic particles within a carrier liquid, generally referred to as a ferrofluid, has attracted great interest due to the inherent characteristics and formative character. The application of a discrete and moderate magnetic field results in an external force which affects the entire system of carrier liquid and nanoparticles and thus allows for a control of the flow property of the fluid. Ferrofluids are generally classified amongst magnetorheological fluids and are characterized by the fact that they remain in a flow state even under the action of saturated magnetic fields ($\approx$ 1 T). 50 years of ferrofluid synthesis and research along with the technical roll-out have provided a deeper insight into the properties which allow for the discovery of new applications, physical characteristics and rules.

Based on the relation between the external force and the direct fluid flow and due to the surface and thermal properties, the range of applications for liquids containing ferromagnetic nanoparticles is broadened even further. The application area of ferrofluids spans across the fields of engineering, physics, chemistry and medicine, where a new approach to cancer treatment is made possible. Ferrofluids are already used for a number of applications, e.g. for the design of loudspeakers, computer hard discs (using magnetorheological fluid as contrast agents (Kim et al., 2003, [9])), for magnetic drug targeting and magnetic hyperthermia used in cancer treatment (Rahn, 2009, [30]) or for filtration and membrane separation (Lesieur et al., 2003, [14]). Due to the nano-scale size of the particles suspended within the liquid, the macroscopic attributes of the resulting ferrofluid is strongly influenced by the particle size, the size distribution as well as the surface or particle-carrier liquid interaction. Furthermore, the viscosity of the system is dependent on e.g. the pH, the temperature or the general particle-carrier liquid compatibility alongside the choice of carrier liquid itself. The yielding behavior is thus easily manipulated.

To ensure a good usability, the ferrofluids need to be stable and the sedimentation issue is typically resolved by an appropriate selection of carrier liquid. This means, that water-based ferrofluids, as used for medical applications, are not expected to be stable over days, weeks or even years like those based on special kinds of polymeric liquid. In that case the nanoparticles have to be coated with a shell of a tailor-made material to avoid agglomeration. Therefore, it is possible to classify two types of ferrofluids: surfacted, which are coated by a surfactant molecule, and ionic, where the shell is on an electric base.

The resulting rheological properties of the ferrofluid play a central role in the design for application - the interests of physicians and engineers are combined here in a complex task. The foregoing explanations underline the vital role of rheological studies for ferrofluid research. As mentioned above, significant research efforts have already been conducted in this direction, e.g. Odenbach et al. in 2002 ([22]) and Pop et al. in 2004 ([24]) amongst others have studied the rheological properties using rotating rheometers while Dang et al. in 2000 ([6]) used a capillary rheometer for a yield stress measure of the ferrofluid. However, a number of questions remain open and provide the basis for future research.

To contribute to this, the thesis work presents a rheological approach to the study of

ferrofluids. In this experimental setup the ferrofluid will be studied in steady-state and dynamical shear mode. First, the matching rheological model for our experimental setup will be derived from known theory. Next, because the study will be held in a magnetic field, the magnetic cell used as measuring device will be designed. The central section then focuses on the normal stresses differences in homogenous magnetic fields. In addition, the viscosity behavior, range of applicability of the Cox-Merz and Laun rule will be obtained and the microstructure of the ferrofluid will be studied by means of rheological techniques.

1. Brief overview of physical ferrofluid characteristics

1.1 Stability

Ferrofluids are a stable suspension of ferri-/ferromagnetic particles in a liquid carrier. The magnetic particles exhibit a monodomain, while the solvent is non-magnetic. The stability must thereore be assured both against sedimentation due to gravity or magnetic force acting on the particles as well as the agglomeration.

The real ferrofluid is always polydisperse. The nanoparticle size distribution then varies depending on the technique of the preparation, very narrow distribution will be assumed.

The stability against sedimentation is given by particle thermal energy inequality to the energy of the acting field (gravitational, magnetic). The thermal energy of the particle must be greater than the energy of the field to allow the particle to move opposite to the gradient of that field. The potential energy of the particle in the gravitational field is

$$E_p = \frac{\Delta\rho\pi d^3}{6} gh \quad , \tag{1.1}$$

where $\Delta\rho = \rho_{particle} - \rho_{liquid}$ denotes the difference of densities, d is the diameter of the particle (approximated as a sphere), g the gravitational acceleration, while h denotes the vertical position of the particle within the sample.

The energy of the magnetic field is given by

$$E_M = \frac{\mu_0 M_0 \pi d^3}{6} H \quad , \tag{1.2}$$

where M_0 is the spontaneous magnetization and H is the acting field intensity.

Both of these energies must be balanced by the thermal energy given by the equipartition theorem

$$E_T = k_B T \tag{1.3}$$

with the Boltzmann constant k_B and temperature T.

Therefore, the critical diameter of the nanoparticles from the point of view of the gravitational field and magnetic field can be expressed by

$$d_{cG} = \left(\frac{6 k_B T}{gh\Delta\rho\pi} \right)^{1/3} \tag{1.4}$$

and

$$d_{cM} = \left(\frac{6 k_B T}{\mu_0 M_0 H \pi} \right)^{1/3} \quad , \tag{1.5}$$

respectively. For the formation of a stable suspension of magnetite-alike materials, the critical diameter is approximately 15 nm.

The ferrofluid could also be designed in such a way that the nanoparticle magnetic agglomeration (resulting in an overlap of the two previously determined critical diameters) is avoided. The energy of dipole-dipole interaction of two particles with magnetic moments $\vec{m}_{1,2}$ with a separation $\vec{r}$, is

$$E_d = \frac{1}{4\pi\mu_0}\left[\frac{\vec{m}_1 \cdot \vec{m}_2}{r^3} - \frac{3(\vec{m}_1 \cdot \vec{r})(\vec{m}_2 \cdot \vec{r})}{r^5}\right]. \tag{1.6}$$

Thus, when the two nanoparticle with $|m| = \dfrac{\mu_0 M \pi d^3}{6}$ collide, the energy of the interaction is

$$E_d = \frac{\mu_0 M^2 \pi d^3}{72}. \tag{1.7}$$

Again, by comparison with the thermal energy of one nanoparticle, the critical diameter yields

$$d_{cD} = \left(\frac{72 k_B T}{\mu_0 \pi M^2}\right)^{1/3}. \tag{1.8}$$

This result further reduces the critical diameter of the (magnetite-alike) nanoparticle for a stable fluid below 10 nm.

There are, of course, additional effects which can be considered. They are however of varying importance for partial ferrofluids, subjected to the coating used or not used for the fluid. Examples are van der Waals or steric interactions and long-range electrostatic interactions for ionic ferrofluids. For more detailed information, the reader is referred to textbooks, e.g. Scherer ([34]).

1.2 Particle relaxation and birefringence

Due to their size, the nanoparticles in the carrier liquid are single-domain and superparamagnetic, i.e. ferrimagnetic below the Curie temperature. These particles can relax by two relaxation mechanisms named after their developers L. E. F. Néel and W. F. Brown. The resulting dominating mechanism for the particle distribution in the fluid causes different macroscopic responses, as is clear from the relaxation characteristics.

First, in small nanoparticles, the magnetic moment vector can randomly flip normal to the easy axis of magnetization, thus exhibiting a thermal effect. The characteristic time between two flips, the Néel relaxation time, is determined by

$$\tau_N = \tau_0 \exp \frac{K'V}{k_B T}. \tag{1.9}$$

where K' denotes the anisotropy constant which, when multiplied with the volume V, provides the energy barrier, along which the magnetization flip takes place. The characteristic time τ_0 represents the attempt time, reciprocal to the Larmor frequency.

Second, all of the particles undergo Brownian motion. During this motion, the nanoparticles rotate freely resulting in a corresponding rotation of the magnetization direction. The viscous torque acts against this rotation, so the Brownian time of rotational diffusion is

$$\tau_B = \frac{3\eta V}{k_B T} \tag{1.10}$$

where η is the viscosity of the carrier fluid, V the hydrodynamic volume and $k_B T$ is the thermal energy of the particle.

If the nanoparticle is in the state where Brownian relaxation is quicker than Néel relaxation, it will dominate and therefore the nanoparticle moves in the liquid carrying a magnetic moment relative to itself along the same direction. From this point of view, the magnetic moment is "frozen" inside the particle and can interact with the field and build microstructures together with other particles within the fluid. If, however, the Néel relaxation mechanism dominates, the magnetic moments flip their direction quickly and the fluid is then in the ground state which is non-magnetic macroscopically. The total relaxation time τ_i can be easily calculated from the parallel processes to yield

$$\tau_i = \frac{\tau_N \tau_B}{\tau_N + \tau_B}. \tag{1.11}$$

In the experiments conducted by F. Gazeau et al. in 1997 ([7]) a wide spectrum of magnetization relaxation times was found. This was an indication of polydisperse nanoparticles while the viscosity and dynamic susceptibility response further indicated the formation of entire chains of nanoparticles. This will be discussed in more detail below.

Furthermore, when an external magnetic field is applied to this generally optically isotropic fluid, it exhibits induced birefringence (Raikher, Stepanov, 2003, [31]). This can be explained by the fact that the nanoparticles are not ideal spheres and the fluid, isotropic due the Brownian relaxation, becomes highly oriented under the acting field.

1.3 Phase separation and chain formation

The thermodynamical instability of the particles will plays its role, even in "stable fluids". This is caused predominantly by the dipole attraction which is marginalized by the applied field. This can lead to phase separation. According to Zubarev ([21]), chain-like structures are built and phase separation takes place even under weak magnetic fields. If, however, no such drops of separated material or chains would be present within the suspension, the interparticle interaction would still significantly influence the rheological properties of the fluid. The next theory introduced by Zubarev uses these approximations: monodisperse ferrofluid, no Néel relaxation, no interaction between the chains and the reaction of the chains to the magnetic field as entire aggregates. Under those conditions, the length of the chain is determined by the minimum of the free energy per unit volume

(Zubarev, [21]):

$$F = k_B T \sum_{nu=1}^{n_c} \left(g_n \ln \frac{g_n}{e} + g_n f_n(\boldsymbol{\kappa'}, \varepsilon') \right) \tag{1.12}$$

$$\boldsymbol{\kappa} = \frac{\mu_0 m}{k_B T} \boldsymbol{H}, \qquad \varepsilon = \frac{\mu_0 m^2}{16\pi a^3 k_B T} \tag{1.13}$$

where a is the hydrodynamical radius of the spheroid particles, m their magnetic moment, g_n is the number of the nu-particle chains in a unit volume of the fluid. Then n_c is the maximal number of the particles in one chain and f_n states for inner-structure free energy. The first term of the free energy F represents the entropy of the ideal gas of n-particle chains due to their translation motion, κ' and ε' are the dimensionless energies of the interaction of the magnetic particle with the field $\boldsymbol{H}$ and of the magnetodipole interaction between two neighbor particles in the chain. By minimizing this energy F and using the normalization condition for the maximum of the particle content in a unit volume $\sum_{nu=1}^{n_c} nu\, g_n = \dfrac{3\varphi}{4\pi a^3}$, where φ represents the hydrodynamical volume concentration of the nanoparticles, for equilibrated systems (ansatz $n_c = \infty$) one receives (Zubarev, [21])

$$g_n = \frac{x_0^{nu} \sinh \kappa' nu}{v \kappa' nu} \exp(-\varepsilon') \tag{1.14}$$

for

$$x_0 = \frac{2y \cosh \kappa' - \sinh \kappa' - \sqrt{(2y \cosh \kappa' - \sinh \kappa')^2 - 4y^2}}{2y}, \quad y = \kappa' \varphi \exp \varepsilon'. \tag{1.15}$$

We assume such approximation which takes only the nearest neighbor for the particle interaction into account and ignores the thermal fluctuation of the chains. Further, we assume that the chains build "straight rod-like" aggregates. This approximation leads to the theory of linear polymer chains and to the result 1.14. The mean particle number in the chain can thus be expressed as:

$$< nu >= \frac{\sum_{nu} nu\, g_n}{\sum_{nu} g_n} = \frac{\varphi}{v \sum_{nu} g_n}. \tag{1.16}$$

These results are important for the rheology of the ferrofluid. As stated before, ferrofluids are very likely to undergo chain formation and phase separation (which allows the observation of small dense droplets within the fluid) - this inhomogeneity and anisotropy influence the stress and flow in the fluid significantly. It is possible to determine a prefered length of the chains within the fluid and under the strain load, as shown by Zubarev ([21]), a maximal number of particles for one chain also exists - in fact, the higher the strain rate is, the more the inner structure is loaded and subsequently destroyed.

The next important parameter is the so-called interaction parameter λ^*:

$$\lambda^* = \frac{\mu_0 M_0^2 V_p}{24 k_B T} \left(\frac{d''}{d + 2s} \right)^3 \tag{1.17}$$

for M_0 the spontaneous magnetization, d'' and V_p the mean magnetic diameter and the volume of the particles, respectively, while s expresses the size of the surfactant layer. The interaction parameter describes the possibility of the ferrofluid particles to form a chain by dipole-dipole interaction. For $\lambda^* > 1$ the dipole-dipole energy is greater than the thermal energy and chains can be formed.

According to the phase separation and chain formation, a huge magnetoviscous effect (the increase of the viscosity with the increasing magnetic field) is found, much more significant than that expected by model of single, non-chain-forming spherical particles distributed in the fluid.

1.4 Rheology of ferrofluids

The ferrofluid is rather complex, since due to the microstructure, it is necessary to apply the theory of polar continuum. Magnetization of the used nanoparticles was considered to be collinear with the external magnetic field in the early works but the answer to the extern magnetic field seems to be more complex.

According to Rosenweig [33], a central set from the system of basic equations for the ferrofluid (13 equations in total) is given by:

- **The equation of continuity**

$$\frac{\partial \rho}{\partial t} + \nabla \cdot (\rho \vec{v}) = 0 \tag{1.18}$$

where ρ is the density of the fluid, $\vec{v}$ its velocity. The fluid is considered to be compressible in general.

- **The equation of motion**

$$\rho \left(\frac{\partial \rho}{\partial t} + \vec{v} \cdot \nabla \vec{v} \right) = -\nabla p + (\eta + \lambda) \nabla (\nabla \cdot \vec{v}) + \eta \Delta \vec{v} + \nabla \times [2\zeta(\vec{\omega} - \vec{\Omega})] + \rho_e \vec{E} + \vec{j} \times \vec{B} + (\vec{P} \cdot \nabla)\vec{E} + (\vec{M} \cdot \nabla)\vec{H} + \vec{P} \times (\nabla \times \vec{E}) + \vec{M} \times (\nabla \times \vec{H}) + \rho \vec{b} \tag{1.19}$$

where $\vec{P}$ is electric polarization vector, $\vec{E}$ electric field vector, $\vec{M}$ is magnetisation, $\vec{H}$ magnetic field vector, p is a pressure-like variable defined as

$$p = p_0(\varrho, T) + \int_0^E \left(\frac{\partial \vec{v} \vec{P}}{\partial \vec{v}} \right)_{T,H,E}^{(e)} dE^{(e)} + \int_0^H \left(\frac{\partial \vec{v} \vec{M}}{\partial \vec{v}} \right)_{T,H,E}^{(e)} dH^{(e)} \tag{1.20}$$

(for further details refer to the original article, Rosenweig, [33]), η is shear viscosity, ζ vortex viscosity, κ third viscosity coefficient, λ is bulk viscosity defined as $\lambda = \frac{\kappa - 2\eta}{3}$, ω angular velocity of the fluid, Ω angular velocity of the nanoparticles, ρ_e is charge density, $\vec{j}$ is the electric current density, $\vec{b}$ is the body force per unit mass.

- **Balance equation of angular momentum**

$$I\frac{d\vec{\Omega}}{dt} = (\lambda' + \eta')\nabla(\nabla \cdot \Omega) + \eta'\Delta\Omega - 4\zeta(\vec{\omega} - \vec{\Omega}) + \vec{M} \times \vec{H} + \vec{P} \times \vec{E} + \rho\mathbf{I} \qquad (1.21)$$

  where I is the moment of inertia per unit volume,λ' the bulk coefficient of spin viscosity, η' the shear coefficient of spin viscosity. Spin viscosity is the viscosity 'as seen' from the frame connected with the rotating particles.

The other 10 equations completing the system of basic equations for ferrofluids can be found in Rosenweig, [33], p. 77.

Rosenweig also notes that, for a special system with negligible angular acceleration, spin diffusion, electric polarization, and distant source of body couple, Eq. (1.21) simplifies to

$$\vec{\Omega} = \frac{1}{4\zeta}(\vec{M} \times \vec{H}) + \vec{\omega}. \qquad (1.22)$$

This is a very important conclusion, if we would like to derive the shape of the stress tensor in our experiment. It allows us to not only use according procedures for the measurement itself, but to provide qualitative predictions as well as to fit the data accordingly to reveal interesting properties of the fluid hidden in the experiment.

2. Derived rheological model

Based on the specific rheology of ferrofluids introduced in Chapter 1 I can derive a ferrofluid behaviour directly for our experiment. Starting with the work of Rosenweig, [33], it is possible to derive basic equations relating to our experiment. In the following, a parallel plate geometry (cylindrical coordinates r, θ, z) is assumed.
At this point, a short summary of the used notation proves meaningful:

$\mathbf{T}$	complete stress tensor
$\mathbf{T}_v$	viscous stress tensor, its symmetric and antisymmetric parts (s) and (a), respectively
$\mathbf{T}_m$	Maxwell type stress tensor for the polarizable fluid
$\mathbf{D}^{(v)}$	strain rate tensor
p	pressure-like scalar, presents a combination of ordinary pressure and field influences
$\vec{M}$	magnetization
$\vec{H}$	magnetic field intensity
$\vec{B}$	magnetic flux density
$\vec{E}$	electric field intensity
$\vec{P}$	polarization
$\vec{\omega}$	fluid rate of rotation: one-half the fluid vorticity
$\vec{\Omega}$	average angular velocity of particles with respect to their own center
η	shear viscosity
ζ	vortex viscosity
κ	third viscosity coefficient
$\lambda = \frac{\kappa - 2\eta}{3}$	bulk viscosity

For a starting point for the considerations concerning the experiment it is possible to use Eq. 1.22:

$$\vec{\Omega} = \frac{1}{4\zeta}(\vec{M} \times \vec{H}) + \vec{\omega} \tag{2.1}$$

because the conditions mentioned, for which this simplification holds, are satisfied in our case. A second important relation can be obtained by considering the form of the viscous stress tensor $\mathbf{T}_v$ ([33], eq. (82), (83) and (84) on p. 75):

$$\begin{aligned} (\mathbf{T}_v^t)^{(s)} &= 2\eta \mathbf{D}^{(v)}, \\ (\mathbf{T}_v^t)^{(a)} &= -2\zeta \vec{\epsilon} \cdot (\vec{\omega} - \vec{\Omega}), \\ tr(\mathbf{T}_v^t) &= \kappa(tr(\mathbf{D}^{(v)})). \end{aligned} \tag{2.2}$$

As we easily see from 2.1, we can express the difference of angular velocities $\vec{\omega} - \vec{\Omega}$ as

$$4\zeta(\vec{\omega} - \vec{\Omega}) = \vec{M} \times \vec{H} \tag{2.3}$$

which can be inserted into Eq. $(2.2)_2$ -

$$(\mathbf{T}_v^t)^{(a)} = -\frac{1}{2}\vec{\epsilon} \cdot (\vec{M} \times \vec{H}). \tag{2.4}$$

2.1 Stress tensor

It is now possible to rewrite the entire stress tensor step-by-step:

$$\mathbf{T}_v = \mathbf{T}_v^{(s)} + \mathbf{T}_v^{(a)} + \frac{1}{3}\mathbf{I}tr\mathbf{T}_v \tag{2.5}$$

$$\mathbf{T}_v = 2\eta\mathbf{D}^{(v)} - \frac{1}{2}\vec{\epsilon}\cdot(\vec{M}\times\vec{H}) + \frac{1}{3}\mathbf{I}\gamma(tr\mathbf{D}^{(v)}) \tag{2.6}$$

$$\mathbf{T}_v = \eta[\nabla\vec{v} + (\nabla\vec{v})^t] - \frac{1}{2}\vec{\epsilon}\cdot(\vec{M}\times\vec{H}) + \lambda(\nabla\cdot\vec{v})\mathbf{I} \tag{2.7}$$

$$\mathbf{T}_m = -\left(\frac{\varepsilon_0 E^2}{2} + \frac{\mu_0 H^2}{2}\right)\mathbf{I} + \vec{D}\vec{E} + \vec{B}\vec{H} \tag{2.8}$$

$$\mathbf{T} = -p\mathbf{I} + \mathbf{T}_m + \mathbf{T}_v \tag{2.9}$$

Recalling Eq. (1.20)

$$p = p_0(\varrho, T) + \int_0^E \left(\frac{\partial\vec{v}\vec{P}}{\partial\vec{v}}\right)^{(e)}_{T,H,E} dE^{(e)} + \int_0^H \left(\frac{\partial\vec{v}\vec{M}}{\partial\vec{v}}\right)^{(e)}_{T,H,E} dH^{(e)} \tag{2.10}$$

with a superscript (e) denoting the equilibrated state and the conventional pressure p_0 within the fluid.

Finally we arrive at the following equation for the stress in the fluid:

$$\mathbf{T} = -\left(p + \frac{\varepsilon_0 E^2}{2} + \frac{\mu_0 H^2}{2} - \lambda(\nabla\cdot\vec{v})\right)\mathbf{I} + \eta[\nabla\vec{v} + (\nabla\vec{v})^t] - \frac{1}{2}\vec{\epsilon}\cdot(\vec{M}\times\vec{H}) + \vec{D}\vec{E} + \vec{B}\vec{H}. \tag{2.11}$$

Therefore, if we are able to define the ordinary pressure in the fluid, the electromagnetic fields as well as the velocities and shear viscosity in the fluid, we can compute the complete shear stress tensor (or its components) and make theoretical predictions for the experimental results.

For work which takes the entire stress tensor into account, further simplification of the relation is proposed. This is due to the fact, that the pressure-like quantity p is rather complex as well the bulk viscosity term as, which we understand should be rather small. A decomposition of the tensor into its trace and the symmetric and antisymmetric parts correlates well with the measurement technique.

In the following, the trace of $\mathbf{T}$ will be denoted as Π, it can be considered the energy content in form of a 'specific electromagnetic-hydrostatic pressure', and the symmetric part and antisymmetric parts as Υ and $\mathbf{A}$, respectively:

$$\Pi = -\left(p + \frac{\varepsilon_0 E^2}{2} + \frac{\mu_0 H^2}{2} - \lambda(\nabla\cdot\vec{v})\right)\mathbf{I} + tr\vec{D}\vec{E} + tr\vec{B}\vec{H} \tag{2.12}$$

$$\Upsilon = \eta[\nabla\vec{v} + (\nabla\vec{v})^t] + \left(\vec{D}\vec{E}\right)^{(s)} + \left(\vec{B}\vec{H}\right)^{(s)} \tag{2.13}$$

$$\mathbf{A} = -\frac{1}{2}\epsilon\cdot(\vec{M}\times\vec{H}) + \left(\vec{D}\vec{E}\right)^{(a)} + \left(\vec{B}\vec{H}\right)^{(a)} \tag{2.14}$$

2.2 Stress tensor derivative

It is now possible to determine the change of the stress tensor with change in the shear deformation rate $\frac{v_\theta}{\partial r} = \dot{\gamma}$:

$$\Pi_{,\dot{\gamma}} = (\lambda_{,\dot{\gamma}}(\nabla \cdot \vec{v}))\,\mathbf{I} + tr\vec{P}_{,\dot{\gamma}}\vec{E} + tr\vec{M}_{,\dot{\gamma}}\vec{H} \tag{2.15}$$

$$\Upsilon_{,\dot{\gamma}} = \eta_{,\dot{\gamma}} + \left(\vec{P}_{,\dot{\gamma}}\vec{E}\right)^{(s)} + \left(\vec{M}_{,\dot{\gamma}}\vec{H}\right)^{(s)} \tag{2.16}$$

$$\mathbf{A}_{,\dot{\gamma}} = -\frac{1}{2}\epsilon \cdot (\vec{M}_{,\dot{\gamma}} \times \vec{H}) + \left(\vec{P}_{,\dot{\gamma}}\vec{E}\right)^{(a)} + \left(\vec{M}_{,\dot{\gamma}}\vec{H}\right)^{(a)} \tag{2.17}$$

The magnetization and polarization can vary with changes in the shear rate which is caused by the physical position change of the nanoparticles or possibly even by changes in the viscosity, which is inner-field-dependent. The tensor Π, however, behaves much more friendly in this form even if the bulk viscosity is still inner-field-dependent.

Therefore, a measurement of the normal stresses provides information about the bulk viscosity and thus the compressibility of the fluid as well as the vortex viscosity rate, which can not be measured directly.

With the given relations, it is possible to use the full part Υ for measurement and model comparison and the derivative of the pressure part Π for vortex viscosity rate estimation from the experiment. Knowledge of the magnetization and polarization shear rate dependence are, however, still required for this.

For the theoretical model, we would need the electromagnetic response of the fluid, in order to simulate the stress response in the system for specific shear rates. This was accomplished using a VSM device (Vibrating sample magnetometer), and the results of such measurements are provided in Fig. (4.3). There, the shear viscosity function, which we have measured in our experiments, is required. This shear viscosity function is, however, a slightly more complicated and should be handled carefully.

2.3 Stress tensor for shear experiment

This section deals with the steady-state situation. For the discussion of the shear experiment, the use of cylindrical coordinates (r, θ, z) is appropriate. Taking into account that in our case $\vec{B} \,||\, \vec{H}$, yields the following equations for

$$\Pi = -\left(p + \frac{\mu_0 H_z^2}{2} - \lambda v_{\theta,\theta}\right)\mathbf{I} + \left(\vec{B}\vec{H}\right)_{zz} \tag{2.18}$$

$$\Upsilon = 2\eta\mathbf{D}^{(v)} \tag{2.19}$$

where the strain rate tensor is given by:

$$\mathbf{D}^{(v)} = \frac{1}{2}\frac{\partial v_\theta}{\partial r}\begin{pmatrix} 0 & 1 & 0 \\ 1 & 0 & 0 \\ 0 & 0 & 0 \end{pmatrix} \tag{2.20}$$

and the antisymmetric part

$$\mathbf{A} = 0 \tag{2.21}$$

It is interesting to note, that the magnetic field influence is seen 'directly' only in the trace tensor Π (which can cause the volume changes and the second normal stress difference N_2 should change faster than first normal stress difference N_1, even for shear thinning fluids, because of this field in z-direction), there is no antisymmetric part and in the deviatoric stress Υ the role of the magnetic field is hidden in the shear viscosity function (for Π, shear viscosity is further hidden in bulk viscosity λ). An exact reconstruction of the deviatoric stress tensor Υ gives

$$\Upsilon = \eta \frac{v_\theta}{\partial r} \begin{pmatrix} 0 & 1 & 0 \\ 1 & 0 & 0 \\ 0 & 0 & 0 \end{pmatrix} \tag{2.22}$$

and the derivation of those tensors with respect to $\dfrac{v_\theta}{\partial r} = \dot{\gamma}$ results in:

$$\Pi_{,\dot{\gamma}} = \left(\frac{1}{3} \left(\kappa_{,\dot{\gamma}} - 2\eta_{,\dot{\gamma}} \right) v_{\theta,\theta} \right) \mathbf{I} + \left(\vec{M}_{,\dot{\gamma}} \vec{H} \right)_{zz} \tag{2.23}$$

$$\Upsilon_{,\dot{\gamma}} = 2\eta_{,\dot{\gamma}} \mathbf{D}^{(v)} + 2\eta \mathbf{D}^{(v)}_{,\dot{\gamma}} \tag{2.24}$$

where

$$\mathbf{D}^{(v)}_{,\dot{\gamma}} = \frac{1}{2} \begin{pmatrix} 0 & 1 & 0 \\ 1 & 0 & 0 \\ 0 & 0 & 0 \end{pmatrix} \tag{2.25}$$

and the antisymmetric part is still zero

$$\mathbf{A}_{,\dot{\gamma}} = 0 \tag{2.26}$$

We can write $\Upsilon_{,\dot{\gamma}}$ as

$$\Upsilon_{,\dot{\gamma}} = \left(\eta_{,\dot{\gamma}} \dot{\gamma} + \eta \right) \begin{pmatrix} 0 & 1 & 0 \\ 1 & 0 & 0 \\ 0 & 0 & 0 \end{pmatrix} \tag{2.27}$$

which is the direct derivation of eq. 2.19.

2.3.1 Shear experiment and theory application

Having laid down the theoretical framework, we can turn to the experimental results. For the experiments the sample fluid was exposed to shear deformation. If the fluid is exposed to a magnetic field, this magnetic field causes a constant term in the trace tensor Π, which is connected with volume changes of the fluid and therefore with the forces acting in the direction normal to its surface. Therefore we can expect two processes contributing to the estimation of normal stresses differences. The N_1 part changes according to the

dependence of the viscosity on the field and the shear rate, while N_2 will 'feel' the same influence of the viscosity change, but there is also a additional constant term at any time and shear rate. This term will modify the shear rate dependence of normal stresses differences. The stress tensor has no antisymmetric part, so the changes in dynamics are only displacement-like. The deviatoric stress Υ is influenced by the magnetic field through the shear viscosity function and is therefore expected to experience different behaviors of shear stress, depending on the magnetic field strength. However,the shear viscosity function is not known in detail. It is the goal of the experiments, which will be described below, to fill this void.

The result for the derivation of the stress tensor with respect to the shear rate $\dot{\gamma}$, can be used along with the known shear viscosity function and a fit for the N_1 term, to find the derivative of the third viscosity coefficient $\kappa_{,\dot{\gamma}}$. Alternatively, it is possible to use the measured functions and fit them into Υ, to determine the correlation of measurement and theory.

3. Viscoelastic Measurements

Some approximations of ferrofluid rheology behavior could be seen in viscoelastic fluids. This approximation is based on the fluid microstructure and the responses known for these fluids. But the behavior of the fluid strongly depends on the carrier liquid nature.

Viscoelasticity was introduced by W. Kelvin, J. Maxwell and L. Boltzmann in the 18th/19th century. Viscoelasticity models suppose that the total stress response to loading can be split into an elastic and memory part and that the memory part does not contribute to their equilibrium stress. The simple materials described by the theory of viscoelasticity behave generally like an elastic solid in short time scales and like a viscous fluid in long scales. In our work, the fluid changes its behavior under the magnetic field influence.

Such materials/fluids may be shear-thinning ones (this is very common property), this means, that the shear stress increases in some shear rate window slower than linearly with the shear rate. The viscosity of such material can decrease orders of magnitude for relatively narrow shear rate change. Or the viscoelastic fluid may be shear-thickening, the opposite behavior to shear-thinning one, thixotropic or rheopectic (changing its viscosity with the time scale) and so one.

In our work, the viscoelastic behavior of the ferrofluids will be studied for comparison. Our measurements are carried out in shear strain mode.

The carrier liquids is characterized by its own strain attributes but with the nanoparticles suspended in it these attributes are shifted. When the nanoparticle chains are built, caused by magnetic field, the fluid becomes anisotropic, oriented, and its flow behavior is dramatically changed. For the assessment of these attributes and their change several ways of measurements were developed. This will be introduced next.

The works of Barnes [1] and Tropea [37] will be used in these sections.

3.1 Shear Strain

3.1.1 Steady mode

Shear in the fluid means that the individual equiplanes in the liquid move to each other during the strain process - such case arises for example when bodies rotate and translate in the fluid, during mutual sliding of two surfaces on the fluid layer presence between them, etc.

The relation between stress and deformation in viscoelasticity is a constitutive relation, generally written as

$$\overset{\leftrightarrow}{\tau} = \mathfrak{F}\left\{\mathbf{F}, \mathbf{D}^{(v)}, ...\right\} \tag{3.1}$$

where $\overset{\leftrightarrow}{\tau}$ is the stress tensor, $\mathfrak{F}\{...\}$ means a functional, $\mathbf{F}$ is a strain tensor and $\mathbf{D}^{(v)}$ is the strain rate tensor (first time derivative of strain tensor), which can be written as

$$\mathbf{D}^{(v)} = \frac{1}{2}\left(\nabla\vec{v} + (\nabla\vec{v})^T\right) \tag{3.2}$$

where $\vec{v}$ is the velocity of the fluid and ^{T} denotes the transposition.

The stress tensor can depend further on higher derivation orders of the strain tensor (elastic solids depend on the strain tensor intself), on the temperature, pressure etc.

We neglect the thermodynamical pressure term hidden in the stress tensor and write only the second part, called viscous stress. The shear part of the viscous stress tensor, τ_{21}, further denoted simply as τ, is proportional to the strain rate tensor as

$$\tau = \eta \mathbf{D}^{(v)} \tag{3.3}$$

where τ is the shear stress in the fluid and η its viscosity. This proportion can be written as

$$\tau = \eta \dot{\gamma} \tag{3.4}$$

where we use the well-known form of strain rate tensor in shear (Eq. 2.20). The $\dot{\gamma}$ is the shear rate, η viscosity and τ shear stress.

For non-Newtonian fluids is the constitutive relation not so easy and therefore the classification is richer.

We can use the experimental measurement of the so-called flow curves, the shear stress τ dependence on the shear rate $\dot{\gamma}$. In many cases is the shear stress for low-enough shear rates proportional to the applied shear stress - the fluid behaves like Newtonian fluid, (3.4). This Newtonian behavior can be for many fluids be seen in the high-enough region of shear rates, where the shear stress is proportional to the shear rate again. For these regions can be estimated appropriate viscosities in accordance to the eq. (3.4): for the low-shear-rate region we can estimate the viscosity and use the symbol η_0 for it. In the high-shear-rate region we denote the estimated viscosity as η_∞.

In the intermediate region, where the law for Newtonian fluids is not fulfilled, a good approximation for its behavior is possible. As we mentioned before, the fluids can behave in this region for example as shear-thinning ones (the viscosity in eq.(3.4) would not be constant anymore and would be shear-rate dependent. $\eta(\dot{\gamma})$ would decrease with an increasing shear-rate) - this is a very common property for many fluids and polymer solutions. Alternatively, the fluid can be shear-thickening (the viscosity $\eta(\dot{\gamma})$ would increase with increasing shear-rate) and so one.

The dependence of the viscosity on the shear deformation rate applied to the fluid can be approximated by the so-called Cross equation in many cases. This equation describes the entire shear rate region, both the Newtonian one and the intermediate region, which no longer corresponds with eq. (3.4). This model can also be applied to the fluids examined for this thesis work. We can express the Cross model for the coefficients of the flow curves in terms of the viscosities:

$$\frac{\eta - \eta_\infty}{\eta_0 - \eta_\infty} = \frac{1}{1 + (K\dot{\gamma})^n}, \tag{3.5}$$

with a constant stress consistency factor K with the dimension of time and a dimensionless material constant, power-law index n for the specific fluid. If shear deformation is applied to the fluid, its shear rate is $\dot{\gamma}$ and the response of the system can be described by the

viscosity η. The constants η_0 and η_∞ are viscosities for sufficiently low and sufficiently high shear rates $\dot{\gamma}$, where the fluid behaves like a Newtonian fluid.

In many cases, $\eta_0 \gg \eta_\infty$, $K\dot{\gamma} \gg 1$ and η_∞ is small. Then the Cross model is reduced to the power-law model (expressed in viscosites as well):

$$\eta = k\dot{\gamma}^{n-1}. \tag{3.6}$$

k is referred to as the consistency with the unit [Pa.s^n], n is the power-law index and the range of well-approximated results of this model is 2-3 decades of the shear-rate.

If we would like to express the power-law model for shear stress, we get:

$$\tau = K\dot{\gamma}^n. \tag{3.7}$$

where K is identical to the same term in the Cross equation (3.5), as is the power-low index with respect to (3.6).

Further, we denote the linear viscoelasticity which is based on a superposition principle. As a consequence of this principle (response is at any time directly proportional to the value of the initiation), the guiding differential equation, which results from the constitutive equations, assumes a linear form. To develop the theory for a pure ferrofluid liquid we would need to use the constitutive equations for ferrofluids, which can be found in Rosensweig, [33].

The Williams-Landel-Ferry equation expresses the superposition principle, and is provided here for shear modulus:

$$G(T, a_T f) = G(T_0, f) \tag{3.8}$$

where G is the shear modulus of the sample, f is the frequency and a_T is a shift factor, defined as

$$\log a_T(T) = \frac{-c_1(T - T_0)}{c_2 + T - T_0} \tag{3.9}$$

where T_0 is the reference temperature and c_1 and c_2 are two fit coefficients.

In the following, the basic steady-state stress responses will be distinguished: these are relaxation (stress relaxation) and creep. Subsequently, the dynamic response is described.

Stress Relaxation

Stress relaxation is associated with the action of a constant shear strain to the fluid. The response to the strain γ_0 is tension within the liquid, which relaxes with time to a lower value. The basic features of fluid viscoelastic relaxation are reflected in the Maxwell model (Fig. 3.1), which consists of a serial connection between a Hooke-like spring of elastic modulus G and a dashpot with a viscous liquid of viscosity η. The modulus G is defined

$$G(t) = \frac{\tau(t)}{\gamma_0}. \tag{3.10}$$

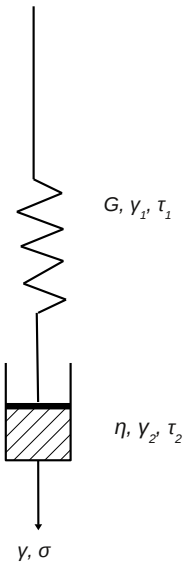

Figure 3.1: Maxwell model (Tropea et al. [37])

For viscoelastic fluids which fall under this rule, the shear stress monotonically decreases with time: $\tau(t) \searrow 0 \quad \text{for} \quad t \to \infty$. Due to the serial connection of the spring and dashpot, the following is applicable

$$\gamma_1 + \gamma_2 = \gamma_0, \tag{3.11}$$

$$\tau_1 = \tau_2, \tag{3.12}$$

and further

$$\tau_1 = G\gamma_1, \qquad \tau_2 = \eta \frac{\mathrm{d}\gamma_2}{\mathrm{dt}} \tag{3.13}$$

while for the time derivative one arrives at

$$\frac{1}{G}\frac{\mathrm{d}\tau}{\mathrm{dt}} + \frac{\tau}{\eta} = 0. \tag{3.14}$$

The solution :

$$\tau(t) = G\gamma_0 e^{-\frac{t}{\eta/G}}, \tag{3.15}$$

can be modified to

$$\tau(t) = \tau_0 e^{-\frac{t}{t_\tau}}, \tag{3.16}$$

where $t_\tau = \eta/G$ symbolizes the relaxation time, which comes from the Maxwell model for the fluid.

In real systems, a slightly different relaxation of tension is observed - it is thus necessary to introduce a correction of Maxwell's model, which exhibits a better correlation with the observations. This is based on a parallel combination of units from the Maxwell model, which have multiple relaxation times. This, more accurate, Maxwell-Weichert model is displayed in Fig. 3.2. The modulus of elasticity of the fluid is then given by

$$G(t) = \sum_{k=1}^{N} G_k e^{-\frac{t}{t_\tau}}, \tag{3.17}$$

where the elastic modules G_k correspond to single base units of the Maxwell model.

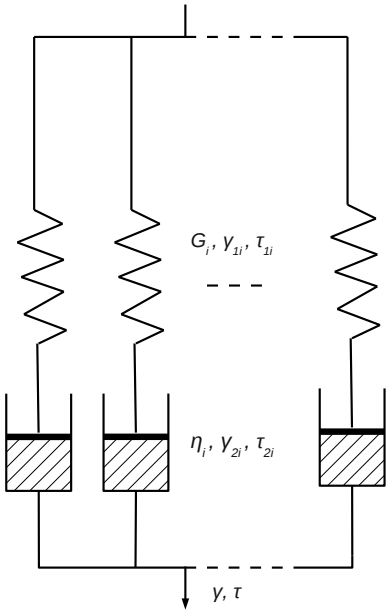

Figure 3.2: Maxwell-Weichert model: schematically for N Maxwell units, parallel connection (Tropea et al. [37])

Creep

If a constant shear stress acts on the fluid, the fluid reaction is known as creep. In this case, in contrast to the former, the shear strain is an increasing function of time. The shear compliance is equal to

$$J(t) = \frac{\gamma(t)}{\tau_0}. \tag{3.18}$$

While strain acts, the Boltzmann rule of superposition is applicable. Therefore, a different model, the Burgers model is designed for creep. It describes the behavior of fluids under

shear tension (fig. 3.3). The model results from the Voigt-Kelvin model (the parallel connection of a dashpot carrying a viscous liquid and a Hooke-alike spring), which provides a good approximation of the behavior of matter with connection, e.g. for rubbers. In addition, in the Burgers model, the the Voigt-Kelvin model is supplemented by a serial connection with the Maxwell model. The following applies for the Burgers model (the strain and tension are depicted in fig. 3.3)

$$\gamma = \gamma_1 + \gamma_2 + \gamma_3 \qquad \tau = \tau_1 + \tau_2, \tag{3.19}$$

$$\gamma_1 = \frac{\tau}{G} \qquad \gamma_2 = \frac{\tau}{G_1}\left(1 - e^{-\frac{t}{t_\tau}}\right), \tag{3.20}$$

$$\frac{\mathrm{d}\gamma_3}{\mathrm{dt}} = \frac{\tau}{\eta}. \tag{3.21}$$

The final relation for time dependence of shear strain has the form:

$$\gamma(t) = \tau_0\left(J + J_1[1 - e^{-\frac{t}{t_\tau}}] + \frac{t}{\eta}\right), \tag{3.22}$$

$$\gamma(t) = \tau_0 J(t), \tag{3.23}$$

where the time-dependent shear compliance $J(t)$ was introduced.

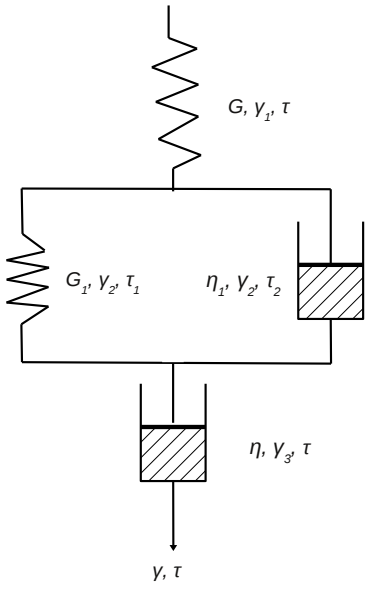

Figure 3.3: Burgers model (Tropea et al. [37])

3.1.2 Dynamical mode

Besides creep and stress relaxation, dynamical measurements are also amongst the most widely employed techniques for the determination of material properties. This is evident, because the dynamical experiments contribute not only to the knowledge of the viscoelastic behavior but to also provide a deeper insight into the structure-mechanical properties of the system.

In the following, the complex unit i will be used.

In a dynamical experiment, the sample is exposed to periods of varying stress or strain to apply a load. Again, assumung a linear viscoelasticity, the response to the load (e.g. strain)

$$\gamma(t) = \gamma_0 e^{i\omega t} \tag{3.24}$$

will be given by the equilibration harmonic with the amplitude γ_0 and a phase term $e^{i\omega t}$, which contains the angular velocity of the acting stress ω.

If we further assume an elastic sample:

$$\tau(t) = G\gamma_0 e^{i\omega t} \tag{3.25}$$

then the shear stress $\tau(t)$ is equal to the product of the steady-state shear modulus G and the shear deformation $\gamma(t)$ from eq. (3.24).

Similarly, for a viscous sample the relation yields:

$$\tau(t) = \eta i\omega\gamma_0 e^{i\omega t} \tag{3.26}$$

and the shear stress $\tau(t)$ is equal to the product of the viscosity of the fluid η and time derivation of the shear deformation $\gamma(t)$ from eq. (3.24). This means that the stress response in the elastic material is in phase with the load while, in contrast, the viscous one is shifted by a half-phase. Therefore, if the material is viscoelastic and both of those properties are thus present, then the material response will be general, with different amplitudes and a shift δ

$$\gamma^*(t) = \gamma_0 e^{i\omega t} \qquad \rightarrow \qquad \tau^*(t) = \tau_0 e^{i(\omega t+\delta)} \tag{3.27}$$

where $\gamma^*(t)$ is the complex shear deformation and $\tau^*(t)$ is the complex shear stress. These two functions can be related using the complex shear modulus G^*:

$$\tau^*(t) = G^*\gamma^*(t) \tag{3.28}$$

$$G^* = G' + iG'' = \frac{\tau_0}{\gamma_0} e^{i\delta} \tag{3.29}$$

where G' is the elastic (storage) and G'' is the viscous (loss) part of the modulus. As can be seen from these relations, the storage and loss modules are connected by the loss tangent δ:

$$G' = \frac{\tau_0}{\gamma_0}\cos\delta \qquad G'' = \frac{\tau_0}{\gamma_0}\sin\delta, \tag{3.30}$$

$$\tan\delta = \frac{G''}{G'}. \tag{3.31}$$

It is now possible to state the complex compliance J^*:

$$J^* = \frac{1}{G^*} = J' - iJ'' = \frac{\gamma_0}{\tau_0} e^{i\delta}, \tag{3.32}$$

where J' and J'' are the real and imaginary part of the complex compliance, respectively, G^* is the complex shear modulus, γ_0 is the amplitude of complex shear strain and τ_0 the amplitude of complex shear stress. Further, the complex viscosity η^* can be given by

$$\eta^* = \frac{\tau^*}{\dot{\gamma}^*} = \eta' - i\eta'' = \frac{G''}{\omega} - i\frac{G'}{\omega}. \tag{3.33}$$

where η' and η'' are the real and imaginary part of the complex viscosity, respectively, G' and G'' the real and imaginary part of shear modulus, γ^* the complex shear rate and τ^* the complex shear stress. ω is the angular velocity of the deformation.

Every single function state above fully describes the viscoelastic behavior during the shear strain but they also depend on the history of the load. For a linear response - the response of the system to the disconcerting is linear and causal - the Boltzmann principle of superposition can be applied. Then the stress response becomes

$$\tau^*(t) = \int_{-\infty}^{t} G(t - t_\tau) \frac{d\gamma^*(t_\tau)}{dt_\tau} dt_\tau \tag{3.34}$$

where $\tau^*(t)$ is the time-dependent complex shear stress, G is the steady-state shear modulus. This equation expresses the Boltzmann principle of superposition as a convolution of the shear modulus and the time derivation of the complex shear rate over the time from $-\infty$ to now. The complex shear stress then depends on the entire deformation history of the sample. Similarly, the complex shear modulus from eq. (3.29) and (3.27)

$$G^*(t) = \frac{\tau^*(t)}{\gamma^*(t)} = i\omega \int_0^{\infty} G(t) e^{-i\omega t} dt \tag{3.35}$$

depends on the entire history of deformation and on the entire spectrum of corresponding steady-state shear moduli.

Table 3.1: Trag Flow Measuring Instruments, see Macosko, [16]

Geometry	**Basic Characteristics**
Couette flow cylindrical	rotating concentric cylinders, usable for low viscosity and high shear rates
Couette flow plane	two parallel plates, homogeneous shear, for high viscosity, problem with the load and gap height
Rotating cone and plate	homogeneous shear, non-Newtonian fluids normal stresses measurable sensitive on the accurate alignment, problems with loads
Rotating parallel plates	inhomogeneous shear varying with gap height, but no problem with loading
Oscillating body	in the low viscosities, ideal for liquid metals
Falling body	usable in high temperatures and pressures, simple model: not usable for viscoelastic fluids

3.1.3 Measurement of the shear viscosity

When the fluid is subjected to shear strain/stress, the measurement of its viscosity or other responses is possible. It is necessary to develop measurement geometries which maximise the accuracy of shear strain and stress measurements. The problem is thus reduced to achieving as simple flow kinematics as possible, ideally an isometric flow in one dimension. This leads to a direct shear strain rate determination and eliminates the dependence on the fluid type. Nevertheless, the flow kinematics are never ideal nor isometric in reality.

Several geometries for rheological measurements have been developed, each having a ideal region for usability. According to Macosko, [16], it is possible to divide the various geometries into several groups: most commonly trag or pressure flow types along with specialized techniques such as ultrasonic measurements. The instruments based on trag flow set the flow of the measured fluid by motion of the instrument boundary or the surface itself and deal with the external force (i.e. gravitational force). Meanwhile, the pressure flow instruments set the flow of the fluid in the motion in fixed instrument geometry and deal with the external pressure. In the tables (3.1) and (3.2), taken from Macosko, [16], a brief overview of the geometries being used nowadays is displayed.

The range of errors or effects which may be encountered when using the specified measurement geometries, is very wide. Examples are introduced below.

One very common problem is the effect of ends and edges or other losses of energy together with an unideal geometry. When moving surfaces are present during the rheometry, the free sample surfaces, typically in contact with air or another gas, must be taken into account. Surface irregularities may also be a factor for cone and plate or parallel

Table 3.2: Pressure Flow Measuring Instruments, see Macosko, [16]

Geometry	**Basic Characteristics**
Poiseuille flow	long capillary, high shear, wide range of measurements, inhomogeneous shear, long lasting experiment
Orifice/Cup	short capillary, only relative viscosity, only Newtonian fluids
Slit pressure flow	parallel plates, capillary flow alike not easy to clean
Axial annulus pressure flow	capillary flow alike, shear uniformity problems with eccentricity

plates geometry. All of these effects cause energy losses or discrepancies and because of the unideal geometry itself the next inaccuracy must be uncounted as well. Other effects, such as a secondary flow effect for the Non-Newtonian fluids during the non-isothermal flows, vortexes or other unwanted flow kinematics, which are increasing with the increasing Re number, may be present within the geometry. Secondary flows, amongst others, leads to non-zero normal stresses; e.g. one can observe the Weissenberg effect. During the experiment the elastic effects, surface tension role, etc. could also affect the results and must be dealt with according to specific situations.

An important process which affects the properties of the measured sample is temperature variation, caused by the environmental influences or by the viscous heating itself. As mentioned earlier, the viscosity is by nature, very sensitive to temperature variations and can influence the experiment output in the spatial and time frame as well.

In our application with a cone-and-plate geometry, the relevant model for viscoelastic fluid was introduced by Olagunju et al., [25]. For the spherical coordinate system (r, ϕ, θ), where $\phi = 1/2\pi - \alpha\psi$, α is the cone angle and $\psi = 0$ at the plate and $\psi = 1$ on the surface of the cone,

$$\nu = \delta(\frac{T}{T_0} - 1) \tag{3.36}$$

$$\delta = \frac{T_0}{\eta_{00}} |\frac{\partial \eta}{\partial T}|_{T=T_0} \tag{3.37}$$

$$\nu = \nu_p + \frac{1}{2} r^2 \psi(1 - \psi + 2\mu) \frac{\eta_{00} \delta R^2 \omega^2}{k T_0} e^{-\nu_p} \tag{3.38}$$

$$\chi = \frac{k' T_0}{\eta_{00} \delta R^2 \omega^2} < \nu - \nu_p > e^{\nu_p} \tag{3.39}$$

where R is the plate radius, ω the angular velocity of the cone, η_{00} is the zero-shear-rate viscosity at the reference temperature T_0, k' the thermal conductivity, μ denotes the temperature discrepancy between plate and cone (we suppose, that only the plate is

tempered and thus the cone could exhibit a different temperature) and ν_p is the scaled temperature at the plate. $< . >$ denotes a radially averaged quantity.

From eq. 3.39 a graph of the temperature deviation from the isothermal value can be determined for the experimental setup, and is displayed in figure 3.4.

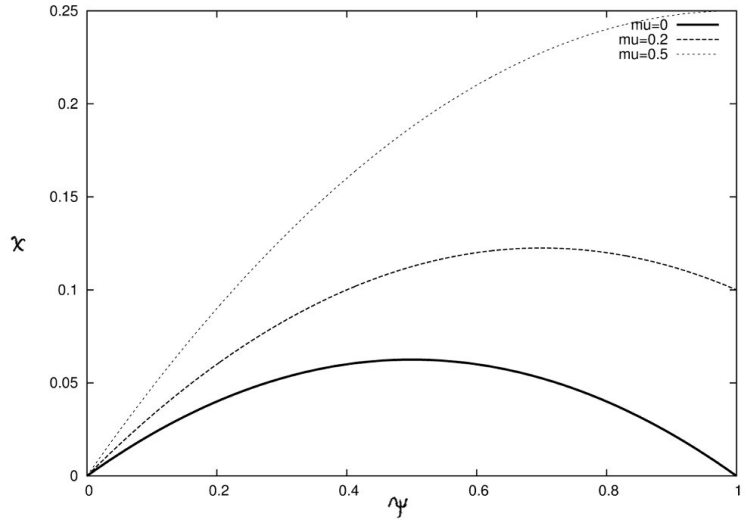

Figure 3.4: The temperature deviation from its isothermal value according to 3.39

Further reading can be found in e.g. Papathanasiou [27] (planar Couette flow), Pinarbasi [28] (Poiseuille flow). It is clear, that for well-conducting fluids the viscous heating affect the results - our measured fluid (see below) are shear-thinning and this effect amplifies with temperature.

As described, a careful measurement is necessary for our non-Newtonian fluid - the non-isothermality of the process is rather typical for polymer fluids (which are in focus for this work as the base fluids) and the appearance of secondary flows (connected with the normal stress in these fluids) is rather predictable. For example, Olagunju [26] showed this effect for the parallel plate geometry, considering the Oldroyd-B model. The Oldroyd-B model, according to the work of S. Musacchio [18], is a simple linear viscoelastic model, used for dilute polymer solutions as measured for the thesis work, which is based on the Dumbbell model:

$$\tau_{ij} = R_0^{-2} \langle R'_i R'_j \rangle, \tag{3.40}$$

for R' the end-to-end vector of the polymer molecule and the radius of the gyration of the molecule R_0. The average is over thermal noise or a small volume V with plenty of molecules. The stress tensor is symmetric and positive definite by definition so its trace includes the measure of the square polymer elongation. According to the Dumbbell model

$$\dot{R}' = (R' \cdot \nabla)v - \frac{1}{t_\tau} R' + \sqrt{\frac{2r_0^2}{t_\tau}} \zeta \tag{3.41}$$

with the polymer relaxation time t_τ

$$t_\tau = \frac{\zeta''}{K_0} = \frac{\zeta R_l^2}{k_B T} \, . \tag{3.42}$$

where R_l is the elongation, ζ'' the friction coefficient changing with the size of the molecule and K_0 the Hook modulus changing with R_l. This leads to the following equation for the single molecule in the Oldroyd-B model

$$\partial_t \tau + (v \cdot \nabla)\tau = (\nabla v)^T \cdot \tau + \tau \cdot (\nabla v) - \frac{2}{t_\tau}(\tau - 1), \tag{3.43}$$

with the matrix of velocity gradients $(\nabla v)_{ij} = \partial_i v_j$. The fluid described by the Oldroyd-B model can, for instance, exhibit the Weissenberg effect, which we need in our model (to determine the normal stresses). Olagunju showed the secondary strem flows in an Oldroyd-B model fluid: for casual experimental conditions as necessitated by our model, where the ratio $\alpha = \frac{h}{R}$ (h: separation of the plates; R: radius) is much smaller than one ($\alpha << 1$), the strength of the secondary flow cannot exceed the $O(\sqrt{\alpha})$ (in our case $\alpha \approx 0.025$).

According to Olagunju [26], the resulting stream function for $\alpha = 0.25$ is displayed in Fig. 3.5 (r and z are cylindrical coordinates scaled as nondimensional):

We will now introduce the measurement geometries, which we use in our experiment. We will use the simplified equation of motion

$$\nabla \cdot \overleftrightarrow{\tau} + \rho \overleftrightarrow{b} = 0 \tag{3.44}$$

for $\overleftrightarrow{\tau}$ the stress tensor and body forces $\overleftrightarrow{b}$. We neglect the inertial forces and allow only the body forces $\overleftrightarrow{b}$, which include gravitational acceleration. This part is based on the work of Tropea, [37].

Parallel plate rheometer

In this case, the two plates are of the form of two circular plates, one of them is rotated about its z-axis. This disc is separated by a distance h from the other one and the fluid, which is to be measured, is placed in the gap. If the gap $h \ll R$, i.e. the radius of those discs, then the outer boundary can be neglected and further equations apply. The shearing planes are plan-parallel planes/discs in this case. The upper plate, casually, rotates with the angular velocity Ω_0. The geometry is displayed in Fig. 3.6. We use cylindrical coordinates r,θ, z again.

The equations of motion under shear deformation in a parallel plate rheometer are in the form

$$\frac{\partial \tau_{rr}}{\partial r} = \frac{N_1 + N_2}{r} \tag{3.45}$$

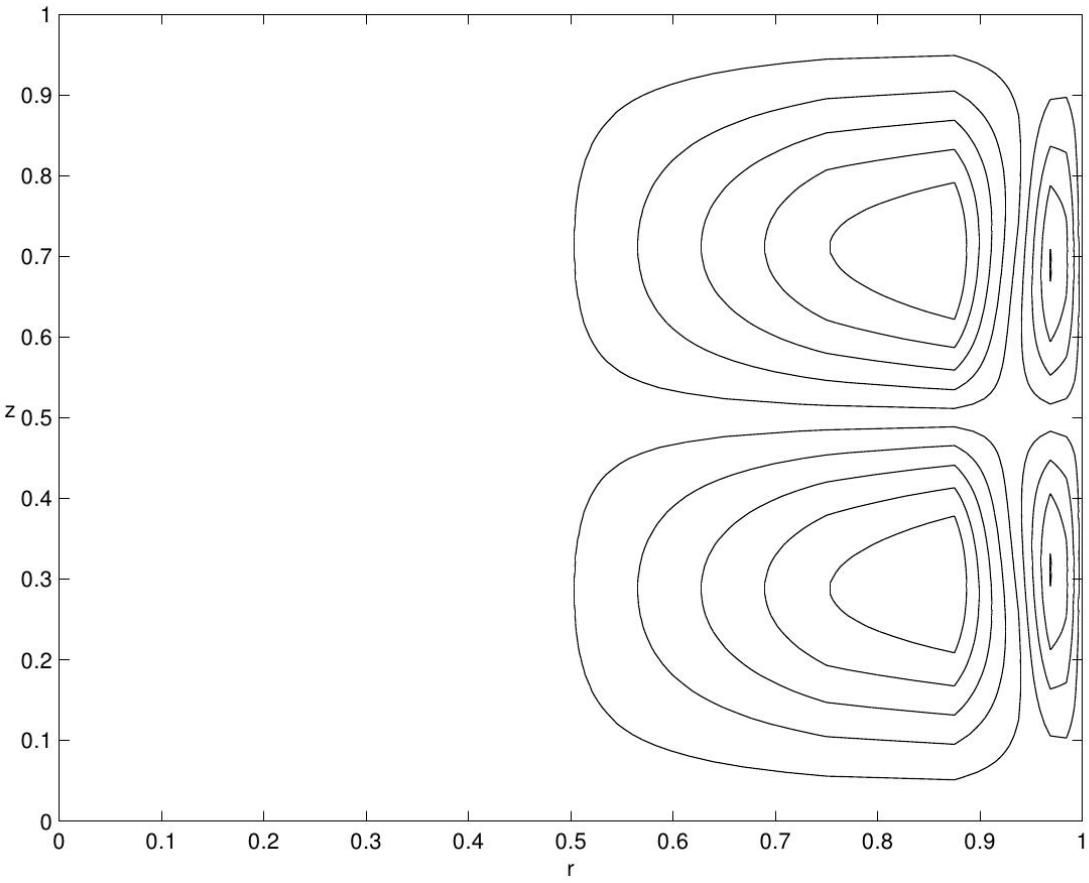

Figure 3.5: Secondary flow in a shear experiment between parallel plates (cit. Olagunju, [26])

$$\frac{\partial \tau_{\theta z}}{\partial z} = 0 \tag{3.46}$$

$$\frac{\partial \tau_{zz}}{\partial z} = \rho g \tag{3.47}$$

where τ_{ij} are the components of the stress tensor $\overleftrightarrow{\tau}$, $N_1 = \tau\theta\theta - \tau_{zz}$ and $N_2 = \tau zz - \tau_{rr}$ are the first and second normal stress differences , respectively, ρ is the density of the sample and $g = |\vec{g}|$ the gravitational acceleration in the z-direction.

The shear rate for such system is given by

$$\dot{\gamma} = r\frac{d\Omega}{dh}, \tag{3.48}$$

where $\dot{\gamma}$ is the shear rate, h is the distance between plates and Ω is the angular velocity at that point. This equation means that the shear rate is not constant along the radius line and thus such a geometry is not the best choice for investigation of fluids which exhibit shear-rate dependent properties.

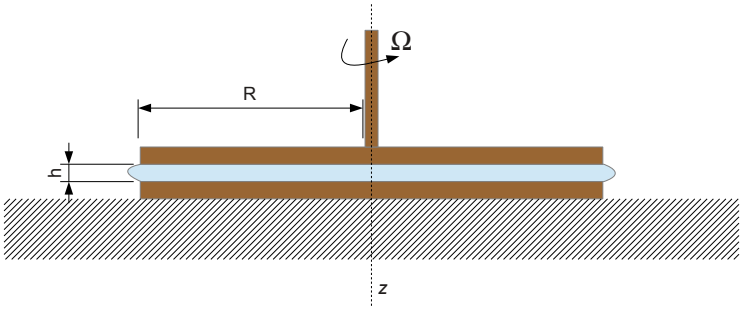

Figure 3.6: Couette flow - parallel plates

Fortunatly, according to eq. 3.46, the shear rate is independent of z and seems to be linear to r:

$$\dot{\gamma}(r) = r\frac{\Omega_0}{h} \tag{3.49}$$

where $\dot{\gamma}(r)$ is the shear rate dependent only on the r-coordinate and Ω_0 is the angular velocity of the moving plate.

In this geometry, the viscosity can be expressed as

$$\eta = \frac{3hC}{2\pi R^4 \Omega} \tag{3.50}$$

where η is the viscosity of the fluid, h the distance between plates, C is the coefficient describing the physical geometry, R the radius of the plates and Ω the angular velocity of the fluid.

Cone and plate rheometer

In this geometry, the cone with a wide top angle, typically larger than 170° is used together with circular plate, so that the angle between plate and cone is given by $\Delta\Theta$ in degrees ($1^o, 2^o, 5^o$,..). In order to get rid of friction between the top of the rotating cone and the fixed plate, the top of the cone is usually truncated and the area is thus only virtual. For this case, the shearing planes have the form of coaxial cones. The cone rotates with an angular velocity Ω_0 and counterclockwise when observed from above. We again refer to spherical coordinates r,θ, ϕ.

Equations of motion for this geometry are

$$\frac{\partial \tau_{rr}}{\partial r} - \frac{N_1 + 2N_2}{r} = -\rho g \cos\theta \tag{3.51}$$

$$\frac{1}{r}\frac{\partial \tau_{\theta\theta}}{\partial \theta} - \frac{N_1}{r}\cot\theta = \rho g \sin\theta \tag{3.52}$$

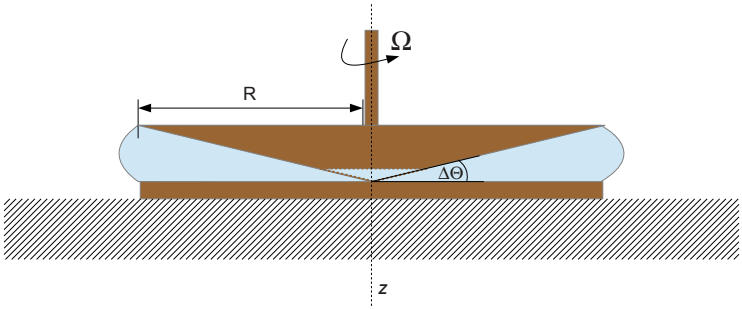

Figure 3.7: Cone and plate geometry

$$\frac{1}{r}\frac{\partial \tau_{z\theta}}{\partial \theta} + \frac{2\tau_{\theta z}}{r}\cot\theta = 0 \tag{3.53}$$

where τ_{ij} are the components of the stress tensor $\overleftrightarrow{\tau}$, $N_1 = \tau_{\phi\phi} - \tau\theta\theta$ and $N_2 = \tau\theta\theta - \tau_{rr}$ are the first and second normal stress differences, respectively, ρ is the density of the sample and $g = |\vec{g}|$ the gravitational acceleration in the z-direction.

Integrating the equation (3.53) we get the constant stress tensor component $\tau_{\theta z}(\theta)$ in the θ-direction - this is the shear stress on the plate. It is possible to set $\tau_{\theta z}(\theta) = \tau_{\theta z}(1/2\pi) = C$ so that the torque moment T_M on the plate yields

$$T_M = \int_0^R r\tau_{\theta z}\left(\frac{\pi}{2}\right) 2\pi r\, dr = \frac{2\pi}{3}CR^3 \tag{3.54}$$

where T_M is the torque moment, R is the radius of the cone and C is a constant corresponding to $\tau_{\theta z}(\theta)$. Therefore, we can extract the stress tensor component $\tau_{\theta z}$ from the equation

$$\tau_{\theta z} = \frac{3T_M}{2\pi R^3} \tag{3.55}$$

The shear rate for the cone and plate geometry is (according to Tropeau)

$$\dot{\gamma} = sin\theta\frac{d\Omega}{d\theta} \tag{3.56}$$

where $\dot{\gamma}$ is the shear rate, Ω is the angular velocity of the fluid and $\Delta\Theta$ is the angle between the cone and plate. Therefore, the shear rate is simply constant in the sample (according to Tropeau, sinθ varies between 1 and 0.996):

$$\dot{\gamma}_0 = \frac{\Omega}{\Delta\Theta} \tag{3.57}$$

where $\dot{\gamma}_0$ is a linearised shear rate from eq.(3.56), Ω is the angular velocity of the fluid and $\Delta\Theta$ is the angle between the cone and plate.

Using this relation for the shear rate, we arrive at a relation for the viscosity

$$\eta = \frac{\tau_{\theta z}}{\dot{\gamma}_0} \approx \frac{3T_M \Delta\Theta}{2\pi R^3 \Omega_0} \tag{3.58}$$

where η is the viscosity, $\dot{\gamma}_0$ is the linearised shear rate from eq.(3.57), Ω is the angular velocity of the fluid, $\Delta\Theta$ is the angle between the cone and plate, T_M is the torque moment, R the radius of the cone and Ω_0 is the angular velocity of the cone.

We do not use a concentric cylinder geometry which is commonly used, because this device demands greater amounts of fluid and our supply was limited. We do not use it even for the normal stress differences for the same reason. Furthermore, due to technical reasons we had to employ the parallel plate for the majority of our experiments, although the cone and plate geometry offers some advantages. As we can see later, however, the two techniques are complementary for the measurement of normal stress and can provide more complex information when used in parallel.

3.1.4 Measurement of normal stresses

Different measurement geometries offer different methods and even levels of measurability for the normal stresses. In our work, the parallel plate and cone and plate geometry was used - also for the flow curves (shear stress dependence on shear rate).

The parallel plate geometry allows a determination of $N_1 - N_2$ (with this geometry the problem remains, that a uncertainty arises for the viscosity, which can be shear dependent) and we can further determine the stress $\tau_{z\phi}$ from the torque. According to this the viscosity in these case can be explored via $\eta = \tau_{z\phi}/\dot{\gamma}$.

$$N_1(\dot{\gamma_R}) - N_2(\dot{\gamma_R}) = \frac{F_n}{\pi R^2}\left(2 + \frac{d\log F_n}{d\log \Omega_0}\right) \tag{3.59}$$

where τ_{ij} are the components of the stress tensor $\overleftrightarrow{\tau}$, $N_1 = \tau\theta\theta - \tau_{zz}$ and $N_2 = \tau zz - \tau_{rr}$ are the first and second normal stress differences, respectively, R is the radius of the plates, Ω_0 the angular velocity of one of them (the second plate does not rotate) and F_n is the normal force which acts on the plates. The stress is

$$\tau_{z\phi}(\dot{\gamma_R}) = \frac{T_M}{2\pi R^3}\left(3 + \frac{d\log T_M}{d\log \Omega_0}\right) \tag{3.60}$$

with the same quantities as stated above.

The cone and plate geometry offers the possibility of $N_1 + 2N_2$ measurements - directly from the equations of motions.

$$r\frac{\partial \tau_{rr}}{\partial r} = N_1 + 2N_2 \tag{3.61}$$

where τ_{ij} are the components of the stress tensor $\overleftrightarrow{\tau}$, $N_1 = \tau_{\phi\phi} - \tau\theta\theta$ and $N_2 = \tau\theta\theta - \tau_{rr}$ are the first and second normal stress differences, respectively. The cone was approximated by a plate (using $\cos(\theta) = 0$). Alternatively, the term $N_1 + 2N_2$ can be obtained from the slope of the plot $\tau_{\theta\theta}$ versus $\ln(r/R)$, where R is the radius of the cone, because the normal stress differences are dependent on the shear rate $\dot{\gamma}$ (and, for the cone and plate geometry is independent of $\dot{\gamma}$ in the r-direction). Therefore the partial derivations are exchangeable. One obtains from the (3.61) by the exchange $\partial\tau_{rr}/\partial r \rightarrow \partial\tau_{\theta\theta}/\partial r$

$$\tau_{\theta\theta}(r) = \tau_{\theta\theta}(R) + (N_1 + 2N_2)\ln(r/R). \tag{3.62}$$

where R is the radius of the cone, $N_1 = \tau_{\phi\phi} - \tau\theta\theta$ and $N_2 = \tau\theta\theta - \tau_{rr}$ are the first and second normal stress differences, respectively. This result yields in the common experiment with low viscous fluids and tubes over the rotating cone (more see Fig. 3.8).

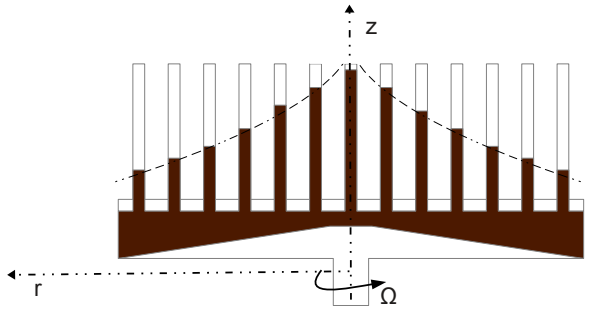

Figure 3.8: The cone and plate geometry with tubes, in those the low viscous fluid shows the measurable normal stress $\tau_{\theta\theta}(r)$ as a function of radius.

From the total force acting on the plate we can get the first normal stress difference from

$$\tau_{\theta\theta}(R) = N_2 \tag{3.63}$$

where $N_2 = \tau\theta\theta - \tau_{rr}$ is the second normal stress difference. Together with 3.62

$$F_n := -2\pi \int_0^R r\tau_{\theta\theta}(r)dr = \frac{\pi}{2}R^2(N_1 + 2N_2) - \pi R^2\tau_{\theta\theta}(R), \tag{3.64}$$

where F_n is the normal force acting on the cone, R radius of the cone, $N_1 = \tau_{\phi\phi} - \tau\theta\theta$ and $N_2 = \tau\theta\theta - \tau_{rr}$ are the first and second normal stress differences, respectively and τ_{ij} are the components of the stress tensor in the fluid. Furthermore we have,

$$N_1 = \frac{2F_n}{\pi R^2}, \qquad \dot{\gamma} = \frac{\Omega}{\alpha} \tag{3.65}$$

for a spherical sample of fluid, with Ω the angular velocity of the fluid, F_n the normal force, R the radius of the cone and $N_1 = \tau_{\phi\phi} - \tau\theta\theta$ the first normal stress difference.

For every measurement geometry, special care must be taken, especially for lower viscous non-Newtonian fluids like polymers. The role of inertia begins to play a role for higher shear rates. The fluids own inertia causes a normal force acting against the elastic one for high rotation rates. One can correct the results (for cone and plate geometry) by using (Kulicke, Kiss, 1977, [10]):

$$F_{inertia} = -0.075\pi\rho\Omega^2 R^4. \tag{3.66}$$

where ρ is the density of the fluid, Ω is the angular velocity of the fluid and R the radius of the cone/plate.

According to the empirical observation, a Cox-Merz rule was introduced in 1958. This rule comes from the observation, that for many polymer melts, the viscosity measured in static shear stress correlates with the complex viscosity measured dynamically. Viscosity for samples that show edge fracture or other elastic flow instabilities at high deformation rates. The Cox–Merz rule is, however, often not succeesful for such fluids exhibiting deformation-dependent microstructures (suspensions, hydrogen-bonded polysaccharides,..), and for high frequencies as well (Al-Hadithi, [8]).

$$|\eta^*(\omega)| \equiv \eta(\dot{\gamma})|_{\dot{\gamma}=\omega} \tag{3.67}$$

where η is the viscosity of the fluid in steady-state mode, $\dot{\gamma}$ is the shear rate in the steady-state mode, ω is the angular velocity in the dynamical mode and η^* the complex viscosity in the dynamical mode.

The possibility to combine these two measurements attracted strong attention from theoreticians and experimentalists in the subsequent years. Theories for this phenomenon were provided by several researchers, e.g. Milner in 1996 ([17]). But in 1986, the connection between the first normal stress difference $N_1(\dot{\gamma})$ measured using steady shear flow and the storage and loss modulus $G'(\omega)$, $G''(\omega)$ measured in oscillatory shear was observed by Laun ([13]):

$$N_1(\dot{\gamma})|_{\dot{\gamma}=\omega} \cong 2G'(\omega)\left(1 + \left(\frac{G'(\omega)}{G''(\omega)}\right)^2\right)^n \tag{3.68}$$

where N_1 is the first normal stress difference, the storage and loss modulus are $G'(\omega)$, $G''(\omega)$, respectively, ω is the angular velocity of the acting deformation and n is a power-law coefficient of the fluid (see eq. (3.6)). This rule was found to be usable for many polymer melts and concentrated solutions and highlighted the relation of linear and nonlinear response of polymers. The power-law coefficient n is mainly chosen according to the polymer and lies within the casual range $n \in (0.5, 0.7)$.

According to Böhme, [3], the normal stresses are connected with the normal stress coefficients, as well:

$$N_{1,2} = \nu_{1,2}(\dot{\gamma})\dot{\gamma}^2 \tag{3.69}$$

where $N_{1,2}$ are the first and second normal stress differences, respectively, $\dot{\gamma}$ is the shear rate and $\nu_{1,2}$ are the normal stresses coefficients. The normal stresses coefficients usually exhibit a strong dependence on the shear rate and thus the zero normal stress coefficients

are introduced:

$$\nu_{1,2}^{0} = lim_{\dot{\gamma}\to 0}\nu_{1,2}(\dot{\gamma}) \tag{3.70}$$

where $\dot{\gamma}$ is the shear rate in the steady-state regime. Although, the fluid behaviour is classified within the range of viscoelasticity, it is good to mention the Neo-Hookean model, where the first normal stresses coefficient N_1 is in connection with the shear stress modulus:

$$N_1 = G\gamma^2 \tag{3.71}$$

where G is the steady-state shear modulus and γ is the strain of the fluid.

This can be useful in the glassy state regime of the fluid.

4. Experimental

The experimental work for this thesis has two objectives. The first aim was to design and employ a magnetic measuring cell, which allows us to measure the flow curves and the differences of normal stresses in ferrofluids. The design will be described in this chapter. The second task, the actual characterization of the ferrofluid, was then conducted using this cell after it has been calibrated and tested. This will be described in the next chapter 4.

4.1 Materials

The rheological measurements were conducted using the measurement apparatus described above. We have examined several fluids, PEO aqueous solution 5 wt% (poly ethylene oxide), magnetofluid Lord MRF 140CG, and a ferrofluid APG513a, of which the first production line was used and which will be referred to as OLD in the following.

The PEO 5 wt% aqueous solution was prepared from the poly(ethylene oxide) $(-CH_2CH_2O-)_n$ with viscosity average of molecular weight $M_v = 900\,000\,\mathrm{g\cdot mol^{-1}}$. It was supplied as a powder by the company Sigma Aldrich. This fluid was chosen as a testing fluid for the magnetic cell and normal stress evaluation. The PEO aqueous solutions is well known to exhibit a quite strong Weissenberg effect which I would like to show with my cell and measurement geometry. The aqueous solution was prepared in our laboratory and should be comparable with commercial available liquid POLYOX WSR-1104.

LORD magnetorheological fluids (MRF) are also known as good normal stresses exhibitors. The MRF 140CG set is a several years old hydrocarbon-based magnetorheological fluid, which (according to the producer) is used nowadays primarily for shocks, dampers and brakes. The fluid consists of micron-sized, ferromagnetic particles in a carrier fluid (non-magnetic oil). They are covered by a protective cover to avoid agglomeration. In a magnetic field the particles create a chain similar to the observation in ferrofluids - MRF also exhibits the magnetorheological effect. The response of the fluid to the magnetic field is simply a sudden transformation from a liquid to a semi-solid state with a controllable yield strength. In absence of a magnetic field, MRF 140CG behaves like Newtonian fluids and does not exhibit yield stress (which is caused by the chain formation).

Table 4.1: properties of LORD MRF-140CG, according to Wiśniewski, [38]

Solids content [wt%]	85.44
Density [g/cm^3]	3.64 ± 0.1
Flash point [^{o}C]	>150

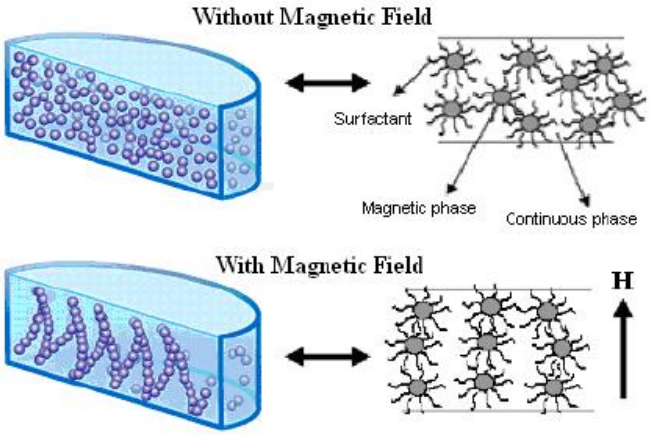

Figure 4.1: Chain formation inside the magnetorheological fluids, cit. [38]

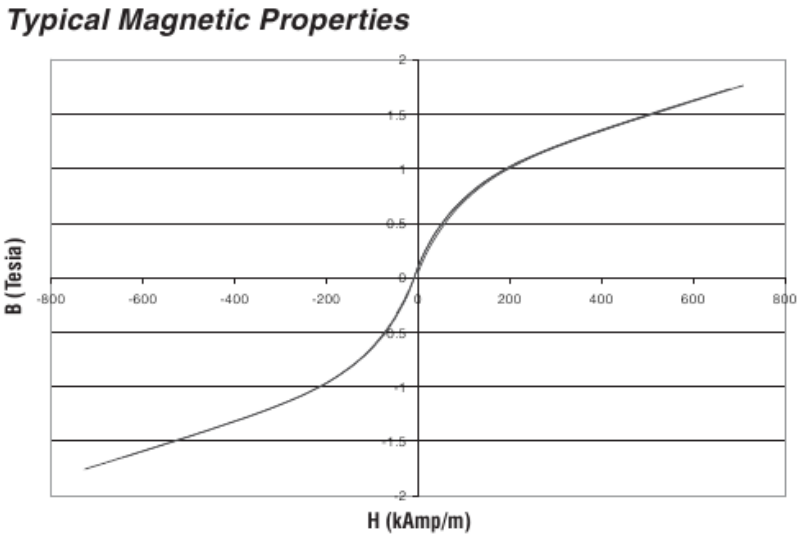

Figure 4.2: The magnetic properties (magnetisation curve including sample magnetic flux density as a function of applied magnetic field intensity) of new MRF 140CG, as provided by the producer ([15]).

The main interest of this work focuses on the ferrofluid sample. I have tested APG513a samples from the company Ferrotec. The fluid sample was several years old, belonging to an older product line. The particle size dispersion culminates (according to VSM measurements) to about 9 nm. According to the producer, the carrier liquid is a di-ester, the particles are from magnetite and the concentration of magnetite is $7,2\%$ (v/v). The ferrofluid includes nanoparticles with a polymer cover of a thickness of about 2 nm. The

APG fluid family was designed for loudspeaker applications but the APG513a is no longer in production.

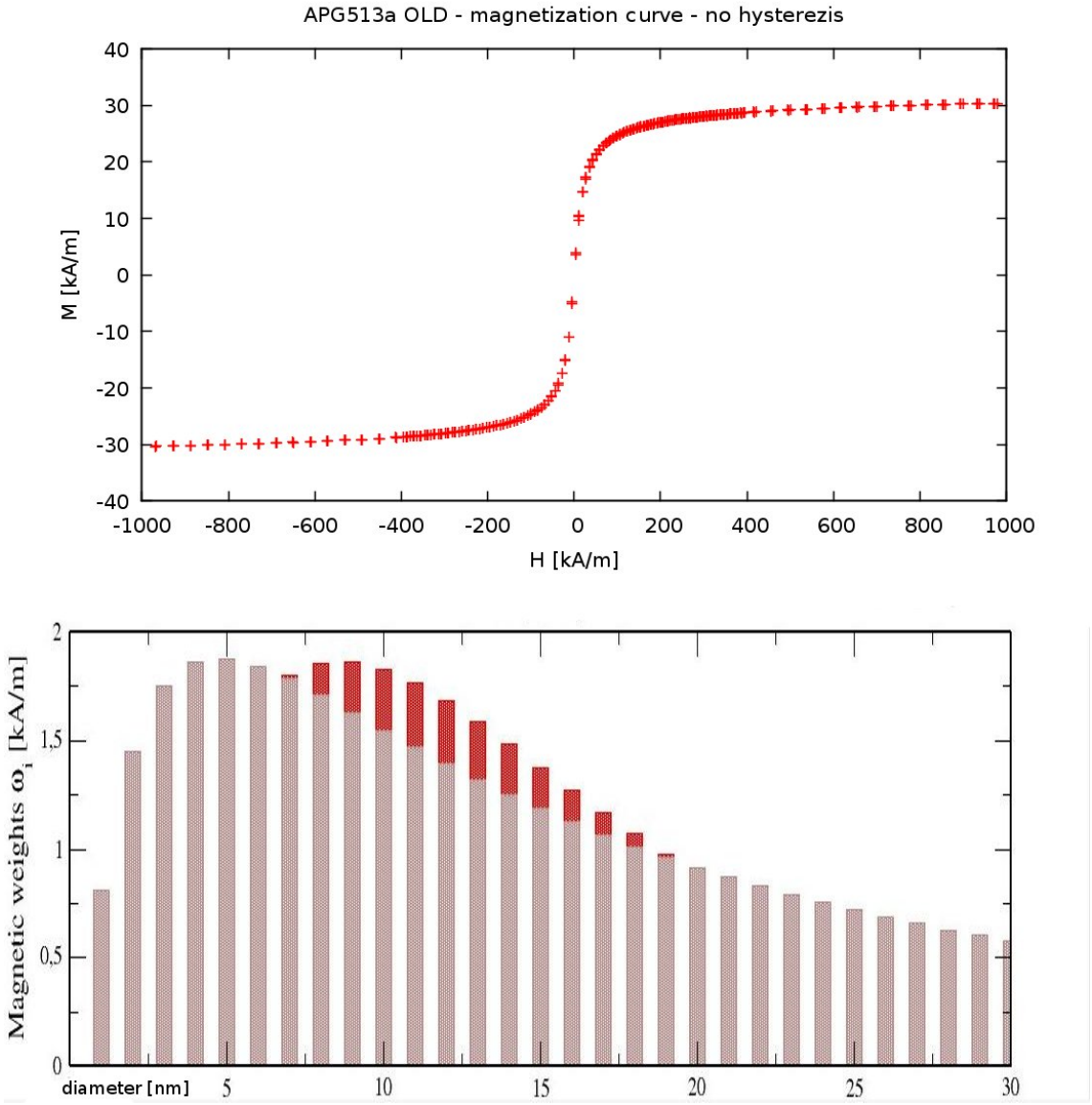

Figure 4.3: Magnetisation curve (sample magnetic flux density in dependence on applied magnetic field intensity) obtained by VSM measurement (upper), its regularization using the software Regmag: particle diameter distribution (lower)

The magnetization curve in Fig. (4.3) was fitted with the Langevin function:

$$M(H) = A\,\mathrm{cotgh}(bH) - \frac{1}{bH} \tag{4.1}$$

with parameters

$$A = 29520 \pm 60$$

$$b = (7.505 \pm 0.128) \cdot 10^{-5}$$

These parameters can be used in a comparison of measurement and theory as in Chapter 2 (for example see eq. (2.18)) since the magnetisation required in the trace part of the stress tensor, Π is known.

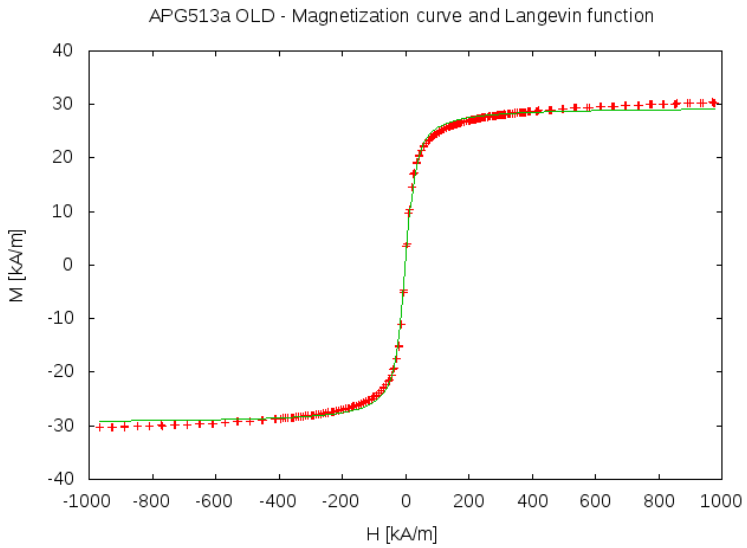

Figure 4.4: Magnetization curve (sample magnetization M in dependence on applied magnetic field intensity H) obtained by VSM measurement. The experimental $M(H)$ curve is then fitted with Langevin function, eq. (4.1).

4.2 Instruments

For the measurement presented in this work a magnetic cell was designed and used. This magnetic cell was custom-made according to our design in the workshop at TU Dresden and was subsequently completed by ourselves. The cell was used in combination with the commercial rheometer Haake Mars III and a custom-made parallel plate geometry, the aspects of which were adjusted to fit with the magnetic cell.

The goal was to build an experimental apparatus which is able to measure normal stresses and to proceed with dynamical measurements in a varying magnetic field. For the available rheometer, it is possible to consider several different solutions. For example, an electromagnetic cell with one solenoid or Helmholtz coils, a magnetic cell with permanent magnets or a coil with a core in various shapes (coil can be external to the rheometer). The solution with permanent magnets was chosen here because of the limited space inside the measurement area of the rheometer, the thermal stability, the low costs and high usability

(since it is not necessary to use an electric source which would create secondary magnetic fields).

4.2.1 Rheometer

The Haake Mars III rheometer was developed by the company Thermo Scientific, a part of Thermo Fisher Scientific Germany. The Haake Mars III modular rheometer platform presents, according to the producer, a "Modular Advanced Rheometer System". The rheometer platform has the form of a two-column stand with different flow of forces in comparison to conventional commercial rheometers (the forces act in one plane).

The Haake Mars III works in the "CS" (controlled stress), and "CD" (controlled deformation) modes in rotation and in CS and CD modes in oscillation and can re-calculate values for "CR" (controlled rate) mode. The pressure forces lie within a range from -50 N to +50 N. The measuring head is equipped with the air bearing. The measuring area can be tempered by electric or Peltier elements at temperatures between -150 °C and +600 °C.

The rheometer is modular; the following components are exchangeable: the temperature control unit, the measurement geometries, the measuring head, and the electronic system. It is possible to purchase additional cells for this rheometer, but for this work a custom-tailored magnetic cell was developed.

Figure 4.5: Haake Mars III - 1. Display and control panel, 2. Holder for tempering units, 3. Electric temperature-module TM-EL-P, 4. Electric temperature-module TM-EL-H, 5. Holder for measuring head, 6. Measuring head; (see the *Instruction Manual Haake Mars III*, Thermo Scientific, Ver. 1.5, p. 40)

4.2.2 Measurement geometries

For the measurement conducted for the thesis work, the measuring geometries called 'cone and plate' and 'parallel plates' (which were introduced in the chapter above) were used. In both cases a custom aluminum bottom plate was used, which reaches the needs of its height in the magnetic cell - the bottom plate was produced on according to our design by the workshop at TU Dresden. The plate has two plateaus because of the fixative ring, which has a constrained height. The upper part of the plate has (68.0 ± 0.5) mm in diameter and has a thickness of (11.0 ± 0.5) mm, the bottom part has (72.0 ± 0.5) mm in diameter and a thickness of(3.0 ± 0.5) mm.

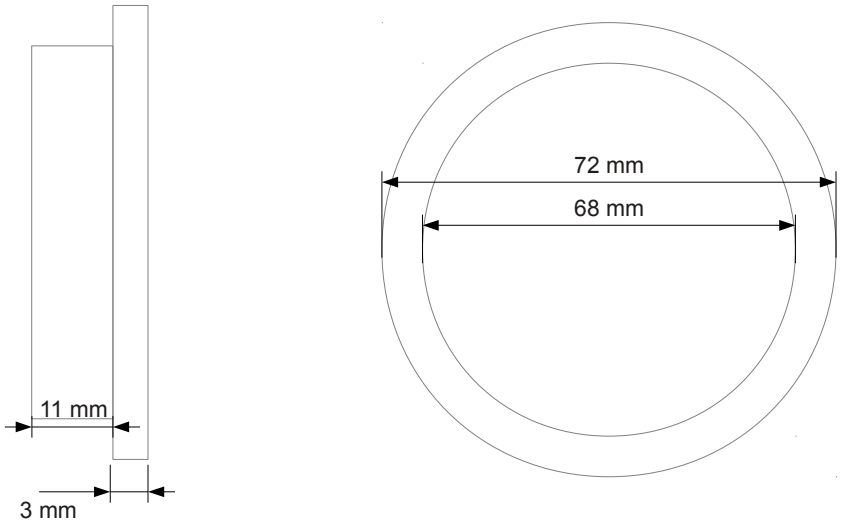

Figure 4.6: The bottom plate for the cone and plate and parallel plate measurement geometry

For the cone and plate measurement a commercial Haake Mars C60 1^o Ti cone was used (cone fabricated from titan with the diameter (60.0 ± 0.5)mm and the plate-cone angle 1°),primarily as a comparative geometry for the results and for the calibration of the new geometry. For the parallel plate geometry the upper plate was custom-made according to our design by Thermo Scientific. It is made of titan as well and the diameter is (19.840 ± 0.005)mm. The thickness of the plate is (2.000 ± 0.005) mm.

The parallel plate geometry, called MR, was calibrated with by measurement with the cone C60 1° Ti (shortly C60) and with the Baysilone Oil M 0.100 and Baysilone Oil M 1.000 at the temperatures 23°C and atmospheric pressure. Both geometries, MR and C60, were used to measure the flow curves of both oils and it was subsequently to determine the calibration constants A and M by the method of least squares in the L_2 norm. For

custom-made geometry MR these were determined to (h=0.5 mm was used):

$$A = (615900 \pm 5800)\,\mathrm{Pa/Nm}$$

$$M = (19.84 \pm 0.4)\,\mathrm{s}^{-1}$$

Then, the results were compared with the method described in the instruction manual to Haake Mars III ver. 1.5, page 120-121.

$$A = \frac{2}{\pi R^3} = 676\,397\,\mathrm{Pa/Nm} \tag{4.2}$$

with the R radius of the plate, and

$$M = \frac{R}{h} = 19.87\,\mathrm{s}^{-1} \tag{4.3}$$

with the set distance h of the plates.

Evidently, for the coefficient M the results are comparable within the error intervals. For the coefficient A they are slightly different and the calculated ones were used for measurements. The MR testing flow curves of the Baysilone 0.100 were found to be in good agreement with the flow curves gained with C60.

4.2.3 The magnetic cell

This chapter serves to describe the magnetic cell design and the test of its usability. The idea of a temperature stable magnetic cell with the field strength up to approx. 100 mT for the measurement of strength temperature-dependent ferrofluids with the Haake Mars III rheometer was fulfilled with the cell containing three permanent magnets. These ring magnets have a variable distance from the measuring plate and the magnetic field in the measuring region is thus easily variable. The permanent magnets do not require cooling and therefore do not contribute to the environmental temperature influences described in chapter 2. Three permanent magntets were employed. Two large ferrite magnets labeled as F30 (rings 220 x 110 x 20 mm), produced by ENES Magnesy Pawel i Tomasz Zientek Sp. k. in Poland, and one smaller neodymium magnet N35 (ring 100 x 90 x 20 mm), produced by Magsy s r.o. in the Czech Republic, were chosen, in order to cover the entire range of the magnetic flux density. The magnetic remanence of the ferrite F30 is stated as 330 mT while it amounts to 1.20 T for the neodymium N35. The geometry of the cell was chosen according to the idea of a long solenoid, in order to establish a homogeneous vertical magnetic field in the center of the cell axis. The geometry is displayed in Fig. 4.7. Both an analytical and FEM model have been computed (see below) for this geometry first, for the F30 and N35 magnets plugged in with the same orientation of the magnetization vector and second, for both F30 magnets with an orientation of the magnetization vector opposed to that of the N35 magnet in the middle. Subsequently, the field in the center was computed for the N35 magnet alone and for the two F30 magnets alone, once with the same orientation of the magnetization vector, and once with the opposite orientations.

In conclusion, such a geometry can cover a wide range of magnetic flux density in the cell center on the rotational axis of the cell.

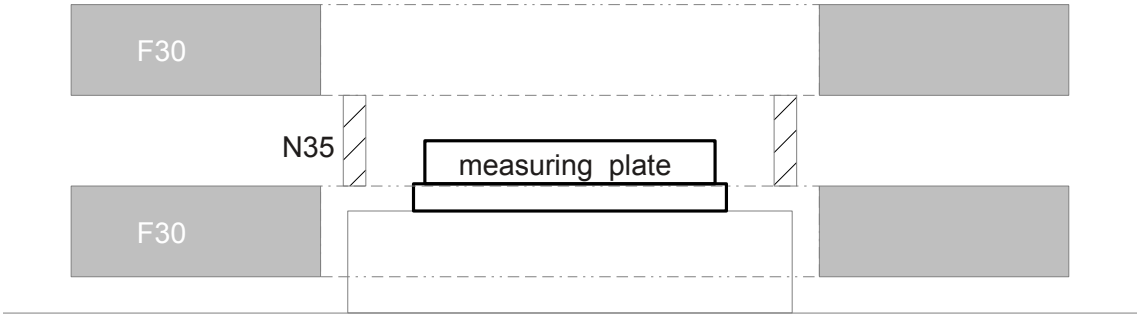

Figure 4.7: Three ring magnets from the side - schema of the geometry

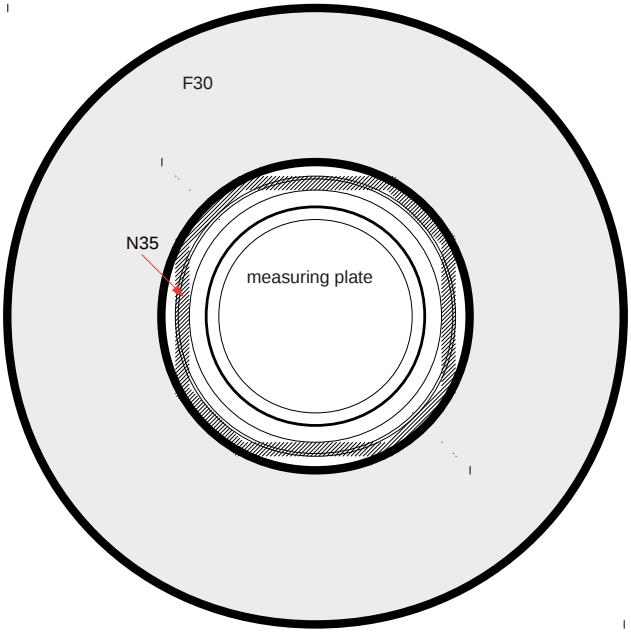

Figure 4.8: Three ring magnets from the top - schema of the geometry

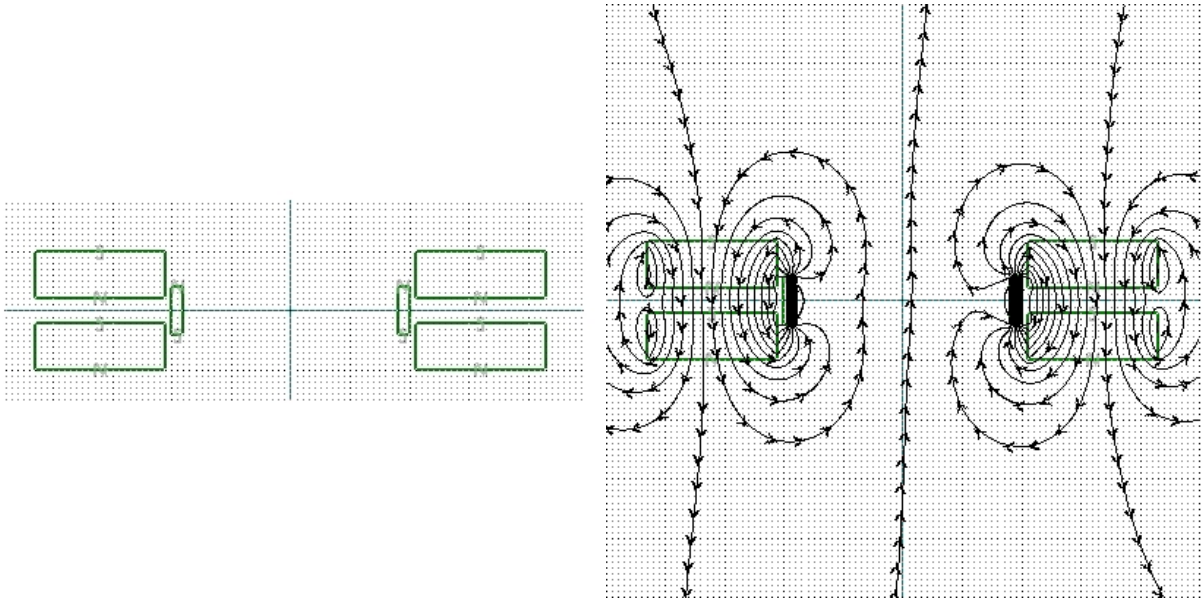

Figure 4.9: Simple 2D simulation of the magnet geometry in Vizimag 1.39 - top the geometry, bottom: with field lines (F30 positive magnetization direction, N35 negative direction of magnetization)

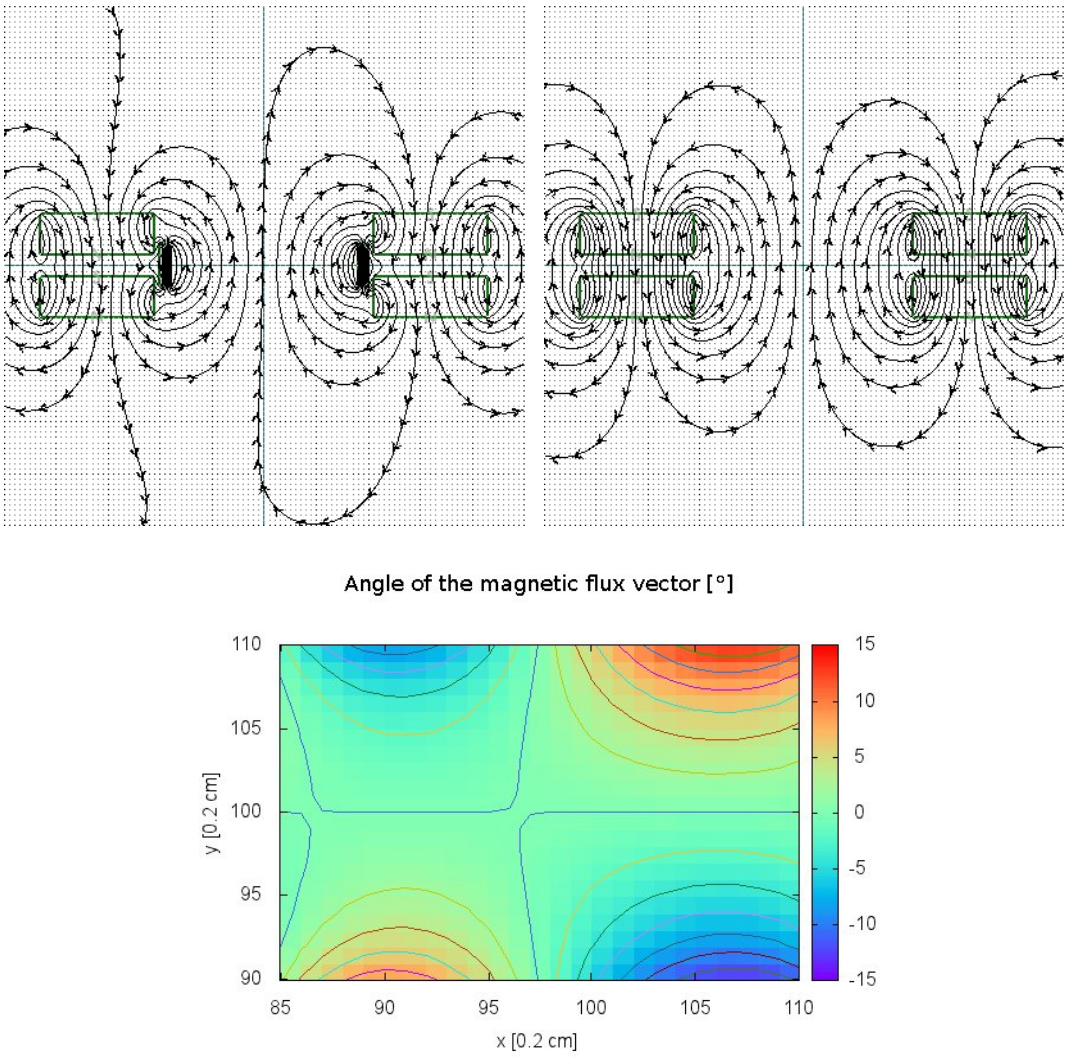

Figure 4.10: From left to right: a) 2D Vizimag simulation - field lines for both N35 and F30 magnets with the same orientation of magnetization, b) 2D Vizimag simulation - field lines for only the F30 magnets with the same orientation of magnetization, c) 3D Femlab simulation - N35 positive, F30 negative: the vector of the B-field on the xy-plane (z=0)

This was also the reason for usage of both neodymium and ferrite magnets - the ferrite magnets itself can cover the middle range of the magnetization (positive and opposite orientation of the vector of the magnetization) and together with the strong N35 magnet can also cover the range around zero very well (both F30 magnetization vectors in the opposite orientation to that of the N35 magnet) or higher values (all the magnetization vectors with identical orientation).

The full overview is provided in Tab. 4.2. Only the promising orientations of those magnets are computed and displayed - based on the field form in the measurement area -

magnet name	d_o x d_i x h[mm]	B_r [T]	material
N35	100 x 90 x 20	1.20	neodymium
F30	220 x 110 x 20	0.33	ferrite

for instance, the assembly with no N35 magnet and both F30 magnets, with an opposite orientation of the magnetization vectors does not promise a sufficiently wide homogeneous vertical field (as computed using Vizimag and FemLab).

For the magnet geometry a holder frame was proposed. The final design of the frame was carried out by Mr. Ulf Neumann. Non-magnetic materials were used for the frame, combining the austenitic steel (screw-able frame for the N35 magnet, screw bolts, nuts), copper (screws, nuts) and aluminum (holder plates for the F30 magnets). The purchased magnets were then combined together on the holder frame (the parts were processed by the workshop at TU Dresden). The holder frame is depicted in Fig. 4.11 and 4.12. The whole magnetic cell together with the holder frame was simulated using FemLab 3.1 in 3D, the geometry of simple magnets according to Fig. 4.7 was simulated by the Vizimag 3.19. Some of these results are displayed in Fig. 4.9 and 4.10.

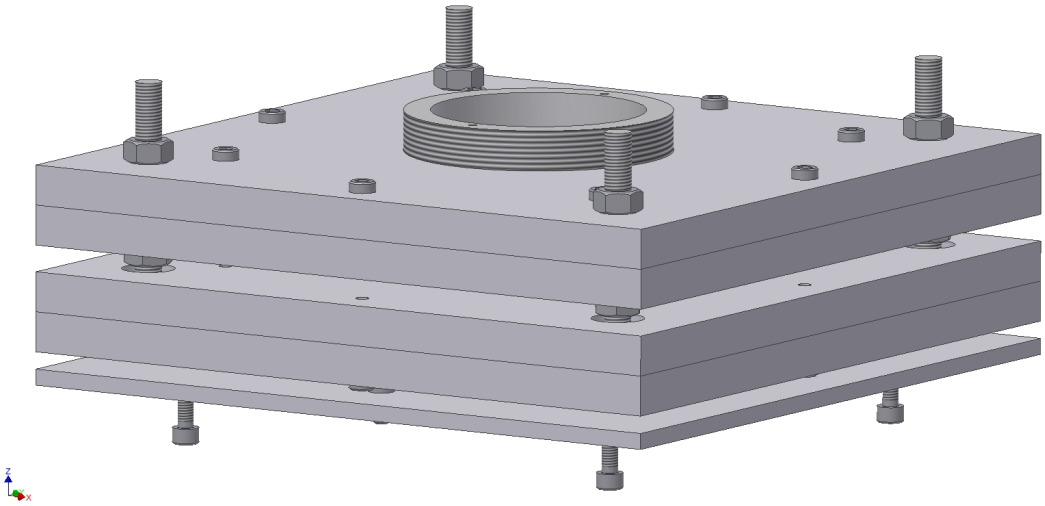

Figure 4.11: The magnetic cell - overview (3D model produced by Mr Ulf Neumann, Lehrstuhl für Magnetofluiddynamik, TU Dresden (MFD))

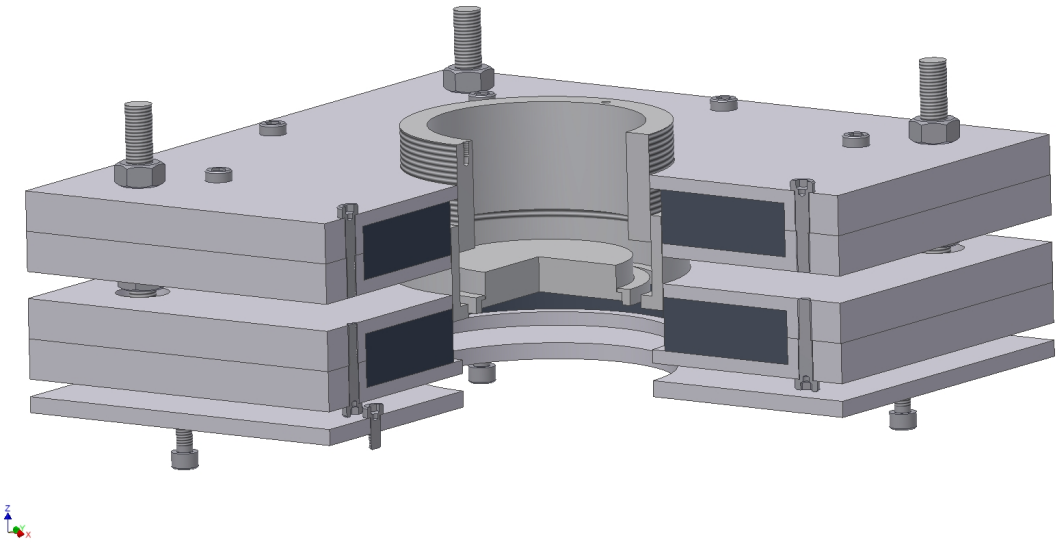

Figure 4.12: The magnetic cell - cut (3D model produced by Mr Ulf Neumann, MFD)

Next, an analytical model was prepared for the magnet geometry. The analytic model was based on the following equations (simple Ampére Law):

$$B_{z_1}(B_{r_1}, R_1, R_2, h, x) = \frac{B_{r_1}}{2}\left(\left[\frac{x+h}{\sqrt{(x+h)^2+R_2^2}} - \frac{x-h}{\sqrt{(x-h)^2+R_2^2}}\right] - \left[\frac{x+h}{\sqrt{(x+h)^2+R_1^2}} - \frac{x-h}{\sqrt{(x-h)^2+R_1^2}}\right]\right) \tag{4.4}$$

$$B_{z_2}(B_{r_2}, R_{1a}, R_{2a}, h_a, x) = \frac{B_{r_2}}{2}\left(\left[\frac{x+h_a}{\sqrt{(x+h_a)^2+R_{2a}^2}} - \frac{x-h_a}{\sqrt{(x-h_a)^2+R_{2a}^2}}\right] - \left[\frac{x+h_a}{\sqrt{(x+h_a)^2+R_{1a}^2}} - \frac{x-h_a}{\sqrt{(x-h_a)^2+R_{1a}^2}}\right]\right) \tag{4.5}$$

Table 4.2: The achievable range of magnetic flux density according to the orientation of the magnetization vector - computed from the analytical model (the flux density range is limited by the physical size of the magnets, the holder frame and the space available in the measuring area of the rheometer)

	F30	N35	magnetic flux density range [mT]
direction:	positive	positive	44 - 64
	positive	no magnet	19 - 39
	positive	negative	-14 - 0

$$
\begin{aligned}
B_{z_3}(B_{r_2}, R_{1a}, R_{2a}, h_a, x, d) = \frac{B_{r_2}}{2} \Bigg(& \left[\frac{x + 2h_a + d}{\sqrt{(x + 2h_a + d)^2 + R_{2a}^2}} - \frac{x + d}{\sqrt{(x + d)^2 + R_{2a}^2}} \right] - \\
& \left[\frac{x + 2h_a + d}{\sqrt{(x + 2h_a + d)^2 + R_{1a}^2}} - \frac{x + d}{\sqrt{(x + d)^2 + R_{1a}^2}} \right] - \\
& \left[\frac{x - 2h_a - d}{\sqrt{(x - 2h_a - d)^2 + R_{2a}^2}} - \frac{x - d}{\sqrt{(x - d)^2 + R_{2a}^2}} \right] - \\
& \left[\frac{x - 2h_a - d}{\sqrt{(x - 2h_a - d)^2 + R_{1a}^2}} - \frac{x - d}{\sqrt{(x - d)^2 + R_{1a}^2}} \right] \Bigg)
\end{aligned}
\tag{4.6}
$$

These equations describe the z-component of magnetic flux density for three ideal magnets (B_{z_1} is the z-component of the magnetic flux density for the N35 magnet, B_{z_2} and B_{z_3} are the z-components of the magnetic flux density for the F30 magnets) without end effects in the assembly as introduced in Fig. 4.7. h and h_a stand for half of the height of the magnets N35, F30 respectively, d denotes half of the distance between the F30 magnets. The following values were used:

$$B_{r_1} = 1.20\,\mathrm{T}; \mathrm{R_1} = 0.05\,\mathrm{m}; \mathrm{R_2} = 0.045\,\mathrm{m}; \mathrm{h} = 0.01\,\mathrm{m};$$

$$B_{r_2} = 0.33\,\mathrm{T}; \mathrm{R_{1a}} = 0.11\,\mathrm{m}; \mathrm{R_{2a}} = 0.055\,\mathrm{m}; \mathrm{h_a} = 0.01\,\mathrm{m}.$$

The magnetic cell was calibrated by LakeShore Gaussmeter and the results were compared with all of the models. The calibration measurement was carried out in the measurement position lying on the rheometer plate. In Fig. 4.13, the analytical model and the measured values are compared. It is evident, that the measured values for the situation with the F30 magnet positive and N35 magnet negative are slightly higher than those predicted by the model, this could be due to the overall contraction of the entire green-blue-red band caused by the magnetic parts of the rheometer. But the main problem is the size of the Hall probe which is installed on the top of the LakeShore Gaussmeter. The accuracy is not very high and the effect is enhanced by the error made by measuring in the 3D space.

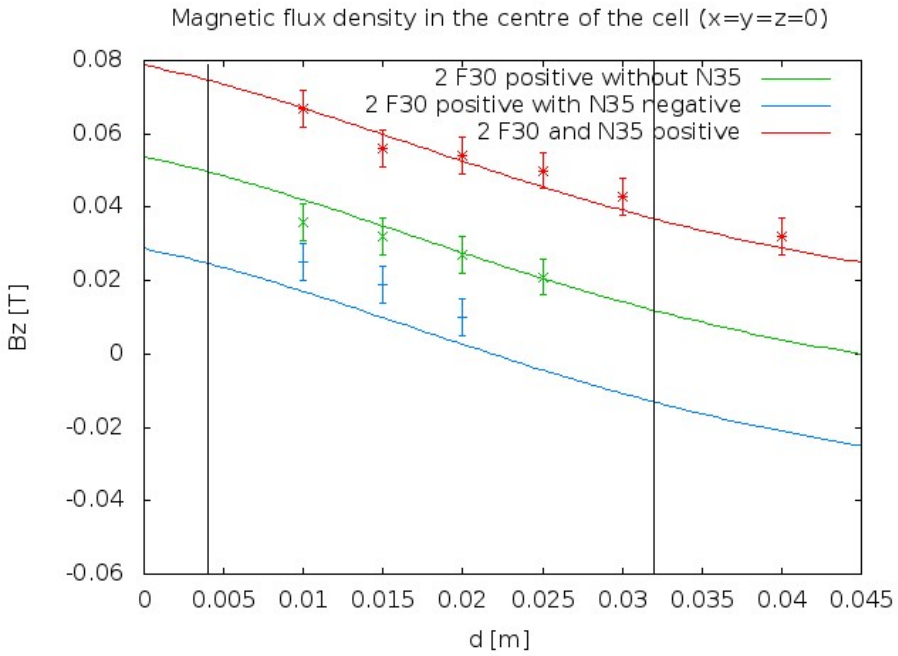

Figure 4.13: Dependence of the z-component of the magnetic flux density, B_z, at half the distance between both F30 magnets, denoted as d. The vertical lines denote the range of magnetic flux densities, which can be achieved with our magnetic cell.

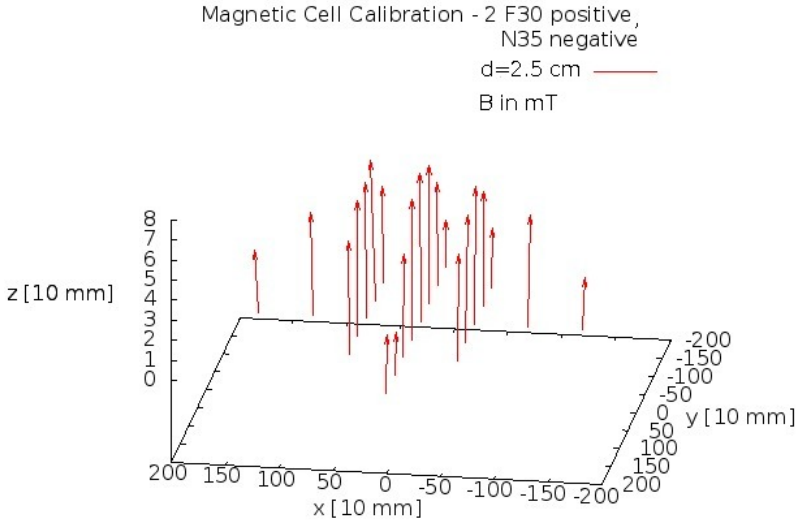

Figure 4.14: Magnetic flux density for the two magnets F30 and N35 with an opposite orientation of magnetization in the holder frame - xy plane for z=0 cm and d=2.5 cm

Based on these results, the vector of the magnetic flux in the xy plane (z-component varies from -2 to 2 cm) is comparable with the model results within the range of error (which is rather rough) and the magnetic cell was found to be sufficiently accurate for the characterization of the magnetofluids and primary ferrofluids.

Subsequently, the magnetic cell was tested with Baysilone Oil M 0.100 and 1.000 with the MR measurement geometry. The flow curves of the following setups have been compared: a. the commercial titan under-plate P60 and cone C60 b. the base plate P60 and measurement plate MR c. the custom-made aluminum base plate and measurement plate MR and d. the custom-made aluminum base plate and measurement plate MR for various magnetic fields in the magnetic cell. This comparison showed a good agreement of the results which means that the data obtained from the magnetic cell are usable also in comparison to other experiments outside this cell (the ability of the rheometer to measure correctly in the magnetic field was confirmed by these experiments).

Note

The entire system suffers from an accuracy problem - the measurement geometry MR was not built with sufficient precision (it was fabricated by Thermo Scientific as a sample only) and during rotation the measurement plate undergoes precessive and nutative movements. Therefore as a result, one obtains for well-defined torque measurement a harmonic signal in a constant state. In accordance with that, all the measured data was recorded over a sufficiently long time period to receive the entire signal information (entire periods of the harmonic signal) and to be able to find the ground state value of the measured one. This causes a significant increase in the required measurement efforts and also proves detrimental to the precision of all measurements. Calibration could only be carried out for a given precision. Additionaly, the precession and nutation require a minimal parallel plate distance (which influences the thermal stability of the sample and the accuracy of the normal stresses measurement).

5. Results and discussion

After the calibration of the magnetic cell a set of shear, creep and dynamic experiments have been conducted for each of investigated fluids. Hereby, 5 wt% aqueous solution of poly ethylene oxide (next referenced as PEO) and magnetorheological fluid Lord MRD served as reference liquids, for the characterization of APG513a.

5.1 Rheological behavior of PEO 5 wt% aqueous solution

The aqueous solution of 5 wt% PEO was prepared and measured for shear and creep with both geometries (C60 and MR) in the linear regime. For each measurement a minimal 5 runs were proceeded. In some cases, often caused due to inaccuracy in measuring geometry, more runs were needed. New samples were used for every run. Subsequently, dynamic measurements were also conducted. The flow curve was compared with the data obtained by Ladouani and Nemdili, [12], see Fig. 5.1. From the experimental flow curve the power-law coefficients were computed (L_2 norm):

$$\begin{aligned} \tau =& K\dot{\gamma}^n \\ K =& (6.216 \pm 0.501)\,\mathrm{Pa.s}^{0.586}, \qquad \mathrm{n} = 0.586 \pm 0.010 \end{aligned} \tag{5.1}$$

which is a typical shear-thinning index for a polymer aqueous solution, containing rather longer molecules. A good agreement is achieved between the measured data and the results obtained by Ladouani and Nemdili [12]. Our measurements were were carried out at 23°C and the PEO has a viscosity average of molecular weight of $M_v = 900\,000\,\mathrm{g\cdot mol^{-1}}$. Therefore, in comparison with Ladouani and Nemdili (Fig. 5.2), our $\tau(\dot{\gamma})$ curve lies close to the left curve (square symbols) for the PEO $\tau(\dot{\gamma})$ dependence for a volume molar weight of $M_v = 1000\,000\,\mathrm{g\cdot mol^{-1}}$.

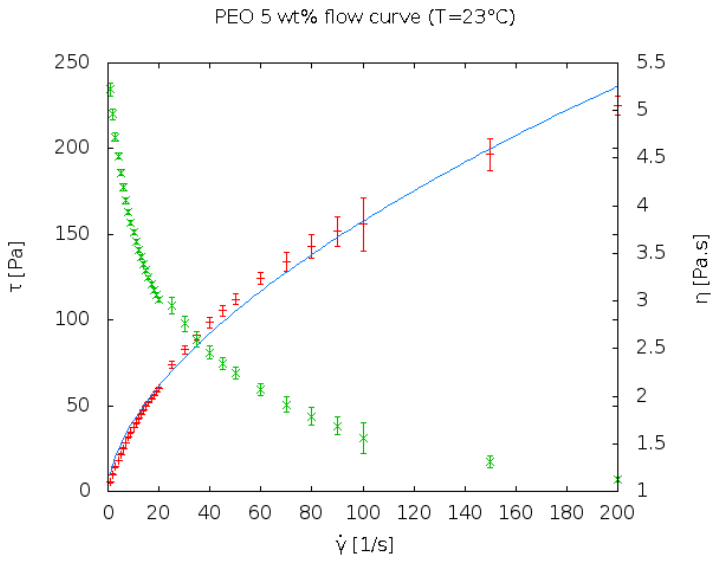

Figure 5.1: The $\tau(\dot{\gamma})$ dependence (flow curve, in red) and the viscosity dependence $\eta(\dot{\gamma})$ (in green). On the stress flow curve power-law, Eq. (5.1), was applied.

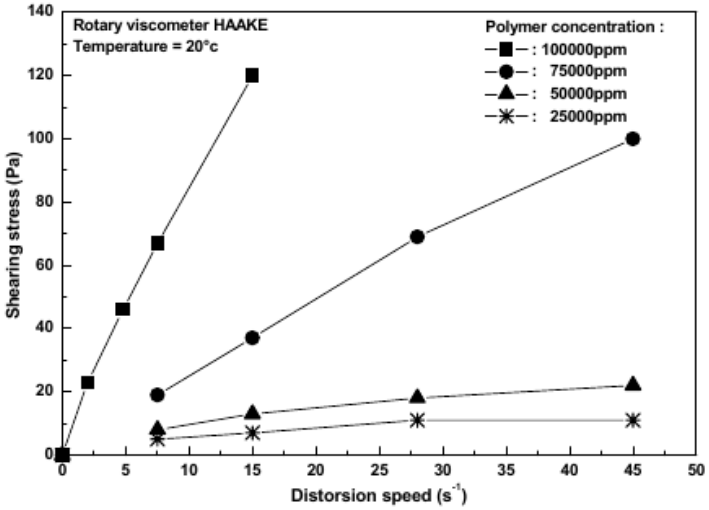

Figure 5.2: Flow curves ($\tau(\dot{\gamma})$ dependencies), as obtained by Ladouani and Nemdili [12].

Subsequently, the normal force were measured using the C60 and MR measuring geometries - with the geometry of parallel plates (here, with device MR) we can measure the differences of normal stresses $N_1 - N_2$ (see Eq. (3.59)), while the cone and plate geometry (here, with the device C60) allows for a measurement of the first normal stresses difference N_1 (see Eq. (3.65)). However, as shown in literature (for example [12]), N_2 is significantly smaller than N_1 and can thus be neglected. The results of both geometries are therefore comparable, as shown in Fig. 5.3. We can see very good agreement between the data

measured with the cone (C60) and the plate (MR) geometries. It can thus be concluded, that the contribution of the second normal stresses difference N_2 to our measurements, is also very small.

From our measurements the normal stress coefficients can be expressed in accordance with the power law, Eq. (3.7):

$$N_1 = K\dot{\gamma}^n \tag{5.2}$$

In our case, the function above was estimated from the data (Fig. 5.3) with coefficients

$$K = (0.670 \pm 0.015)\,\mathrm{Pa.s}^{0.211},$$

$$n = (0.211 \pm 0.001).$$

The small power-law index is in accordance to power-law results in the case of shear stress measurements (Eq .(5.1)). The parameter K and the power-law index are rather smaller. Because this parameter K contains information related to the shear modulus in hard matter, we can conclude that the PEO solution is rather viscous.

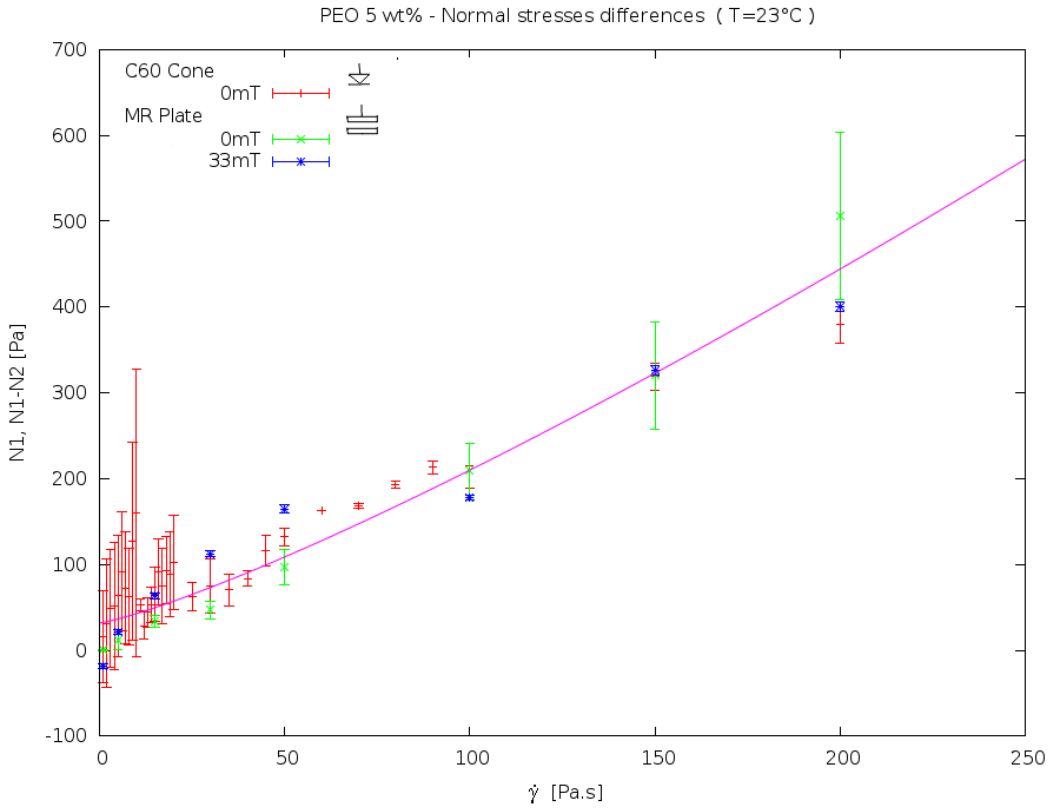

Figure 5.3: The first normal stress difference N_1 and normal stress differences $N_1 - N_2$ with respect to the shear rate $\dot{\gamma}$. Red: N_1 without a magnetic field, measured in the C60 geometry. Green: $N1 - N_2$ measured in the MR geometry, without a magnetic field. Blue: with a 33 mT magnetic field.

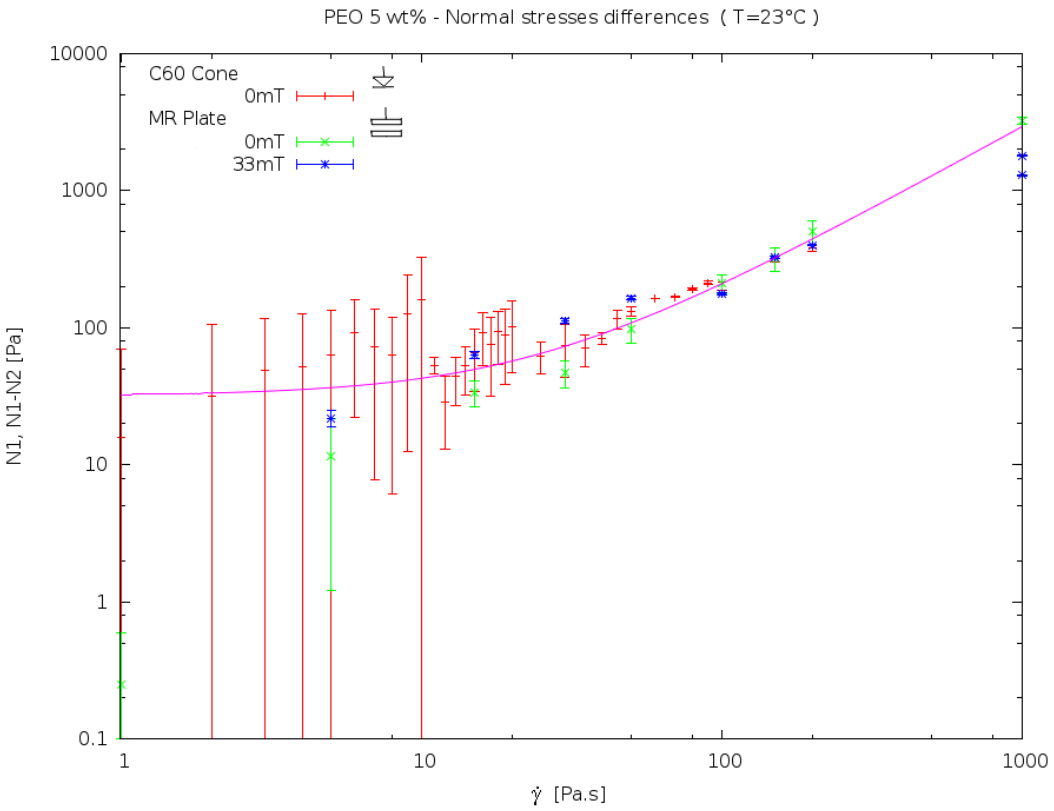

Figure 5.4: The first normal stress difference N_1 and normal stress differences $N_1 - N_2$ with respect to the shear rate $\dot{\gamma}$. Displayed in log scale to include a broader shear rate window. Red: N_1 measured in the C60 geometry, without a magnetic field. Green: $N1-N_2$ measured in the MR geometry without a magnetic field. Blue: in 33 mT magnetic field

The fluid dynamical experiments conclude this first set of measurements. One can see in Fig. 5.5, that the dynamical shear modulus is rather low. In this range of temperature and frequency the fluid is still within the flow regime where the viscosity and flow play the main roles. Therefore, the deformation is also non-recoverable. On the border of the measurement window, at 100 Hz, the fluid approaches the rubbery plateau which exhibits both the flow and elastic body attributes. For higher frequencies, a different slope and elastic plateau (glassy state) are expected.

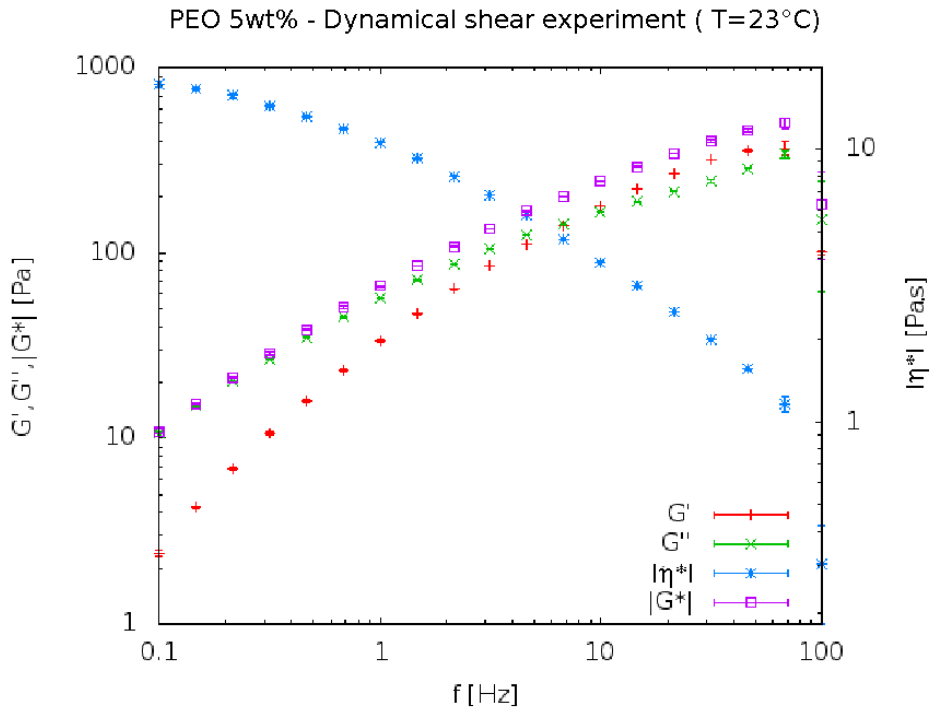

Figure 5.5: Storage and loss shear moduli (red and green), the complex modulus (purple) and complex viscosity (blue) as a function of frequency for the PEO 5 wt% in water at 23°C.

5.2 Magnetorheological behavior of fluid Lord MRF 140CG

The magnetorheological fluid LORD MRF 140CG was measured in steady shear flow and in oscillatory shear flow (linear regime, if not explicitly stated otherwise). This fluid was measured with the MR plate and the PP60 base plate. The measurements were conducted for magnetic field strengths in the range of (0 - 12.1) mT. For each measurement a minimal 5 runs were proceeded but usually more runs were needed. New samples were used for every run because the fluid may change its attributes during measurement. Due to the effect of In-Use-Thickening and the evaporation of the base fluid, the results cannot be easily compared those of other research groups or to the manufacturer specifications. For more details on In-Use-Thickening and the variation of magnetorheological fluid characteristics with time, the reader is referred to e.g. Carlson, [5].

The flow curves are displayed in Fig. 5.6. These flow curves were also fitted with the power law function:

$$\tau = K\dot{\gamma}^n \tag{5.3}$$

In these experiments, the power-law index is almost constant for different field strengths

and remains within a range of $n \in (0.6 - 0.7)$. The consistency coefficient K cannot be fitted very precisely but we can say it increases with an increasing intensity of the applied magnetic field. The consistency coefficient is one order higher than the one for PEO 5wt% aqueous solution which is in accordance to in-vivo observations. Both of the power-law rule coefficients for magnetorheological fluid LORD MRF 140CG are summarized in Tab. 5.1.

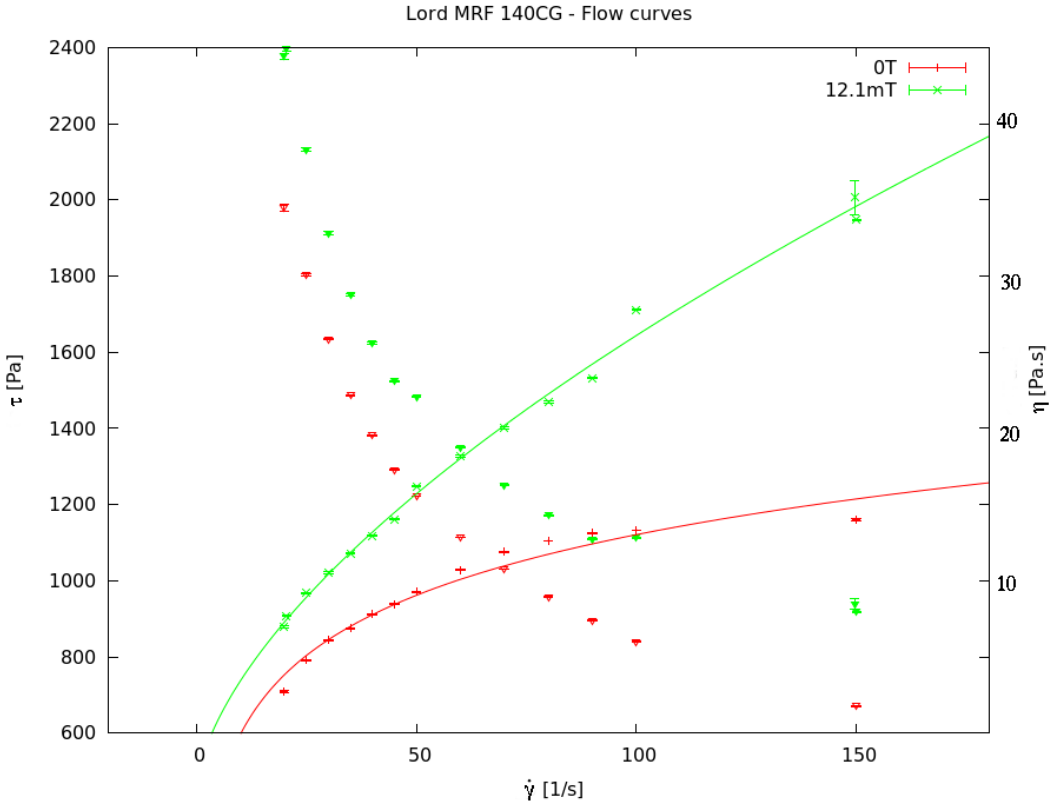

Figure 5.6: Experimental flow curves $\tau(\dot{\gamma})$ of Lord MRF 140CG without a magnetic field (red) and with a 12 mT magnetic field (green), crosses for shear stress and diamonds for viscosity, as displayed on the second axis.

The experimental flow curve can be compared with the flow curve provided by the producer [15]. This curve, obtained at a temperature of 40°C (which means lower viscosities at the same shear rates in comparison to the measured data), is displayed in Fig. 5.7. In comparison with Fig. 5.6 the range of stresses is one order lower which cannot be explained simply by the difference in measurement temperatures. However, the producer obtained this curve with a freshly fabricated fluid and I have used a sample which is several years old. This discrepancy is expectable because of the so-called thickening process. In our case, the sample must have already undergone the thickening process. This effect of a viscosity change over time is well known [5].

Table 5.1: Consistency coefficient K and power-law index n according to Eq. (5.3) for magnetorheological fluid Lord MRF 140CG.

B [mT]	K [Pa.s^n]	n [-]
0	43.42 ± 6.949	0.647 ± 0.029
2.1	54.18 ± 1.254	0.601 ± 0.004
9.6	36.27 ± 10.39	0.677 ± 0.052
12.1	70.19 ± 29.50	0.616 ± 0.072)

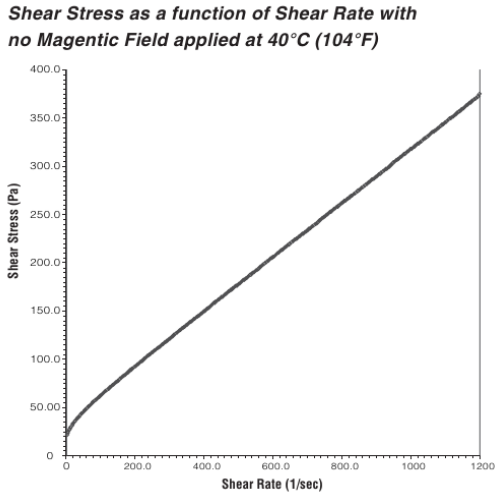

Figure 5.7: Flow curve $\tau(\dot{\gamma})$ for the fluid Lord MRF 140CG, as provided by the producer, [15].

We can see, that the fluid does not change its power-law index which mean it stays in the same shear-thickening state with or without the field. This fact can be due to the thickening process, as previously noticed. During this process, the microparticles in the fluid can dissolve, break down and aggregate. Naturally, the fluid was exposed to ultrasound and a mixing procedure before every measurement in order to minimize the ageing effect, however it could not be fully suppressed.

This result is further underlined by the results for the first difference of normal stresses, as is evident in Fig. 5.8. The normal stresses measurement displays the anisotropy of the fluid in zero magnetic field, which is not a common fluid property and which can related to the thickening process. Furthermore, the fluid exhibits a broadened anisotropy as the field increases.

A fit of the normal stresses differences N_1 was carried out according to the power law as given in Eq. (5.2):

$$N_1 = K\dot{\gamma}^n \tag{5.4}$$

The reaction of the fluid shows a tendency to lower the consistency coefficient K with an increasing magnetic field intensity and a simultaneous increase of the power-law index. In comparison to shear stress, the normal stress in the fluid exhibits a one order higher consistency coefficient and a lower power-law index (it reaches comparable values for a magnetic field flux density of 12.1 mT). Both coefficients are displayed in Tab. 5.2. We can observe a rather large uncertainty for the consistency coefficient. But the decrease of the consistency coefficient K with an increasing magnetic field is very interesting, because it means that the fluid no longer carries the elastic properties which contribute to the complex viscoelastic behavior. The opposite tendency would be expected - a larger magnetic field intensity should lead to a 'harder' and 'more solid-like' fluid. This property is only observed in the normal direction, not in shear (here the consistency coefficient increases with increasing field).

This following measurement was conducted both with the parallel plate geomtery (MR) and the cone-and-plate geometry (C60) with zero magnetic field. In this case, the very good correlation of C60 and MR measurements confirms the hypothesis of a negligible value of the second stresses difference N_2. In Fig. 5.8 the experimental normal stresses differences curves are depicted for various magnetic field strengths when using a MR parallel plate geometry.

Table 5.2: Coefficients of the power-law fit for normal stresses differences of magnetorheological fluid LORD MRF 140CG, according to Eq. (5.4)

B [mT]	K [Pa.s^n]	n [-]
0	155.3 ± 209.4	0.272 ± 0.169
2.1	115.9 ± 214.9	0.309 ± 0.259
9.6	5.841 ± 10.23	0.823 ± 0.329
12.1	1.46 ± 24.63	0.629 ± 0.195

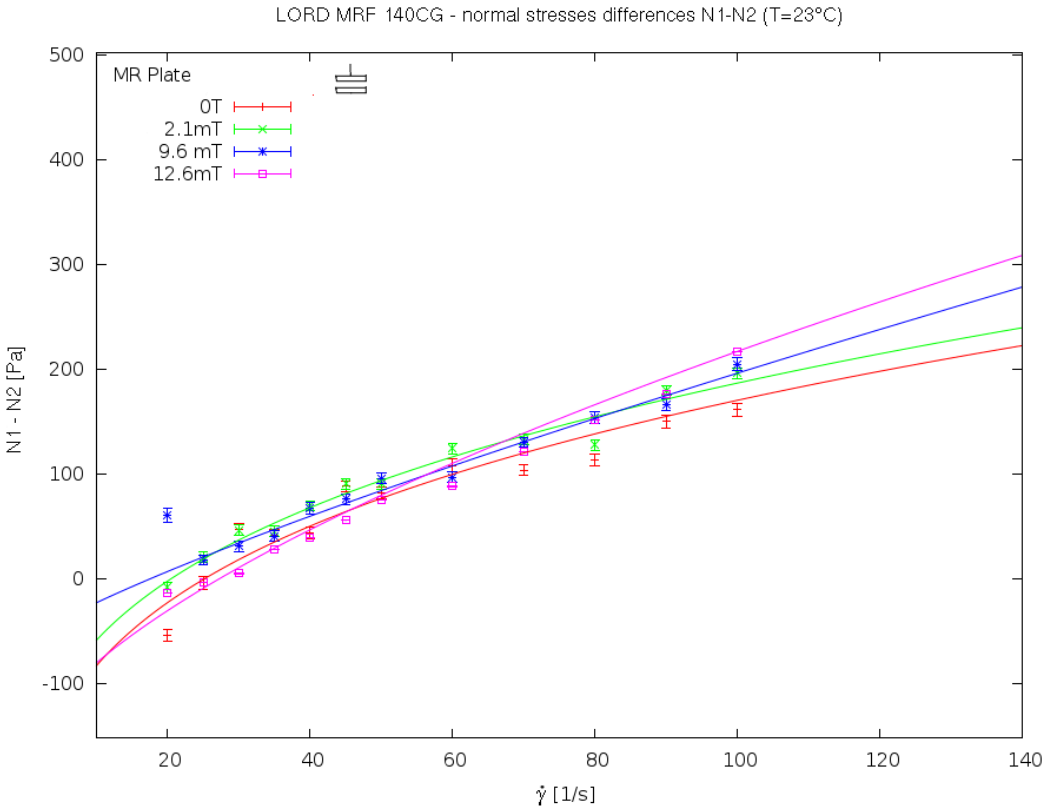

Figure 5.8: The measurement of normal stresses differences in magnetorheological fluid LORD MRF 140 GC at 23°C in the parallel plate geometry MR. Red: the normal stresses differences $N_1 - N_2$ as a function of shear rate $\dot{\gamma}$ with zero magnetic field. Green: in a magnetic field of magnitude 2.1 mT. Blue: magnitude of 9.6 mT. Purple: magnitude of 12.6 mT.

In order to reach lower shear rates dependencies for the shear stress curve and the normal stresses difference curves, the oscillatory shear experiments were conducted. As is evident from the results, the fluid is in a flow regime at room temperature (measured at 23°C) for a frequency window of $f = (0.1 - 100)$ Hz. As we stated above, the second

normal stresses difference N_2 can be neglected in our measurements and we can, therefore, work with the normal stresses differences results including only the first normal stresses difference N_1 (instead of the entire term $N_1 - N_2$ which is actually measured with the MR parallel plate geometry). Fig. 5.9 displays the comparison of the storage, loss and complex shear moduli (G', G'' and $|G*|$, respectively) along with the complex viscosity $|\eta*|$. The flow regime is evident here for larger loss shear modulus than storage shear modulus. The complex viscosity exhibits the shear thinning property.

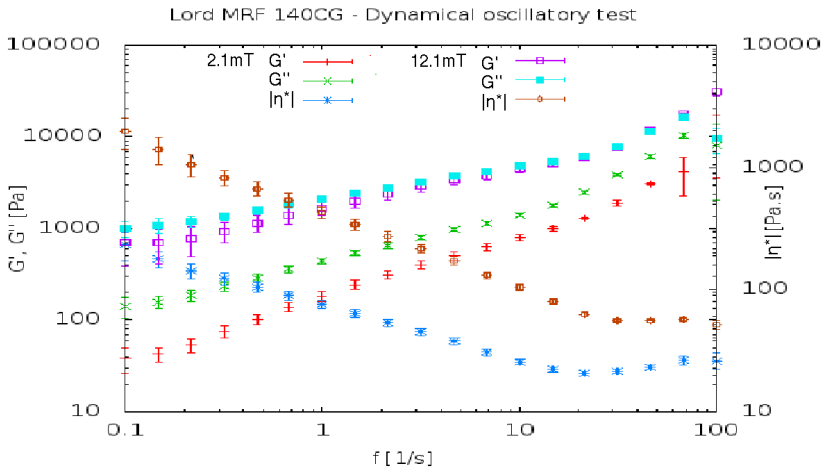

Figure 5.9: The oscillatory shear experiment for magnetorheological fluid Lord MRF 140CG at 23°C. The dependencies of the storage and loss shear moduli (G' and G'') on the frequency f are depicted (a) for a magnetic field intensity of 2.1 mT in red and green, respectively and (b) for 12.1 mT in purple and blue squares. The dependency of the complex viscosity on the frequency f is depicted with blue crosses on the secondary axis and with dark red circles for a magnetic field intensity of 12.1 mT.

The semi-empirical Cox-Merz, Eq. (3.67), and Laun's rule, Eq. (3.68), allow us to employ this data to obtain extended flow curves and the dependence of the first normal stresses difference on the shear rate $\dot{\gamma}$ (as discussed above, it is possible to deal with the results of the measured difference $N_1 - N_2$ as the pure N_1 value and it is subsequently possible to apply Laun's rule). The Cox-Merz rule, Eq. (3.67), compares the steady-state viscosity η with the complex viscosity $\eta*$ from the dynamical experiment, for the same angular velocity ω in the dynamical mode as the shear rate $\dot{\gamma}$ in the steady-state mode:

$$|\eta^*(\omega)| \equiv \eta(\dot{\gamma})|_{\dot{\gamma}=\omega} \tag{5.5}$$

This provides an extended viscosity dependency curve ($\eta(\dot{\gamma})$) according to the power law. The extension is presented in Fig. 5.10. We can observe a very good accordance which allows us to apply Laun's rule (more details on this problem are provided by Al-Hadithi, [8]).

Laun's rule is more complicated and compares the storage and loss part of the complex shear moduli, G' and G'', with the first normal stresses difference N_1, again for the same angular velocity in the dynamical mode as the shear rate in the steady-state mode:

$$N_1(\dot{\gamma})|_{\dot{\gamma}=\omega} \cong 2G'(\omega)\left(1+\left(\frac{G'(\omega)}{G''(\omega)}\right)^2\right)^n \tag{5.6}$$

For the application of Laun's rule, we need to use the model of the fluid in order to examine the power index n. We use the power-law with indexes as obtained from the experimental data (see Tab. 5.1). The entire Laun's rule relation (Eq. (3.68)) had to be shifted to lower values because of different calibration. The results are provided in Fig. 5.11. After applying the shift, the data correlate very well.

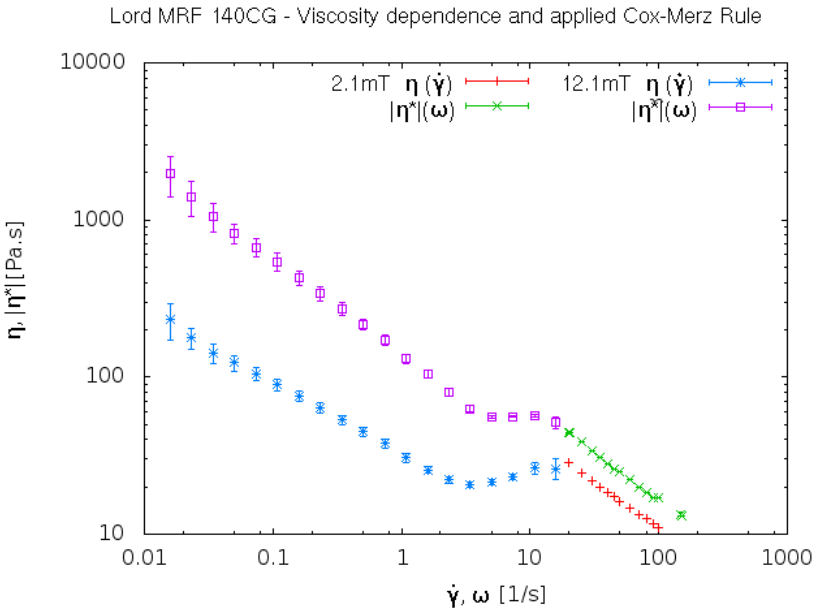

Figure 5.10: The Cox-Merz rule, Eq. (3.67), applied to the steady-state experimental viscosity curve, Eq. (5.6), and the dynamical complex viscosity curve, Fig. (5.9), for magnetorheological fluid Lord MRF 140 CG at 23°C. The steady-state viscosity, η, is depicted (a) for a magnetic field flux density of 2.1 mT, in red and (b) for 12.1 mT, in green. The complex viscosity $\eta*$ is depicted (a) for a magnetic field flux density of 2.1 mT, in blue and (b) for 12.1 mT, in purple.

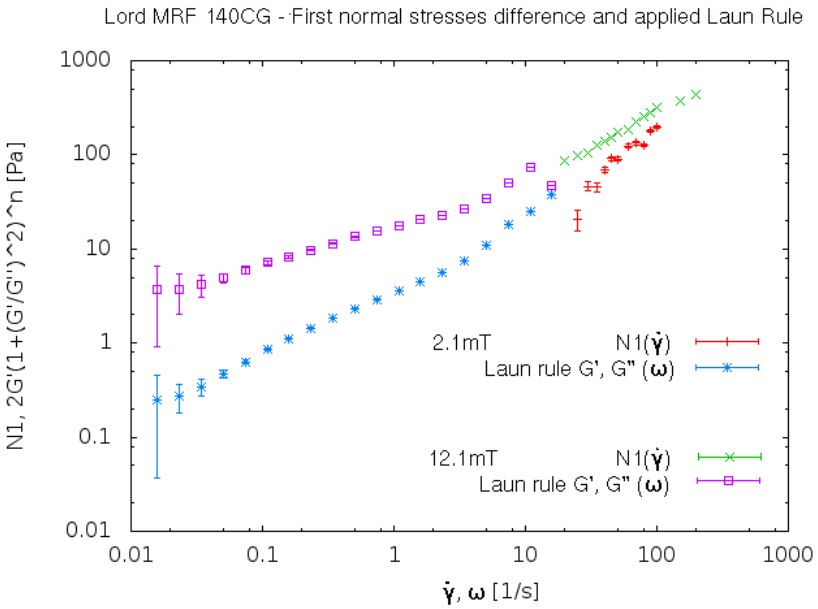

Figure 5.11: The application of Laun's rule, Eq. (3.68), on the steady-state experimental normal stresses differences curve, Fig. (5.8), and the dynamical storage and loss shear moduli curve, Fig. 5.9, in magnetorheological fluid Lord MRF 140 CG at 23°C. The steady-state first normal stresses difference N_1 is depicted (a) for a magnetic field flux density of 2.1 mT, in red and (b) for 12.1 mT, in green. The dynamical storage and loss shear moduli data is depicted (a) for a magnetic field flux density of 2.1 mT,in blue and (b) for 12.1 mT, in purple.

The application of Laun's rule, allows us to observe the influence of the magnetic field on the rheological properties of the fluid.

From the experimental viscosity curve in Fig. 5.10, the magnetoviscous effect can thus be expressed for a broader range of shear rates. Using the time-temperature superposition principle, the range of known viscosities for different magnetic field strengths can also be explained. According to the given graph, the magnetoviscous effect for the shear rate $\dot{\gamma} = 0.016s^{-1}$ is up to 850 %. An overview is displayed on a logarithmic scale in Fig. 5.12.

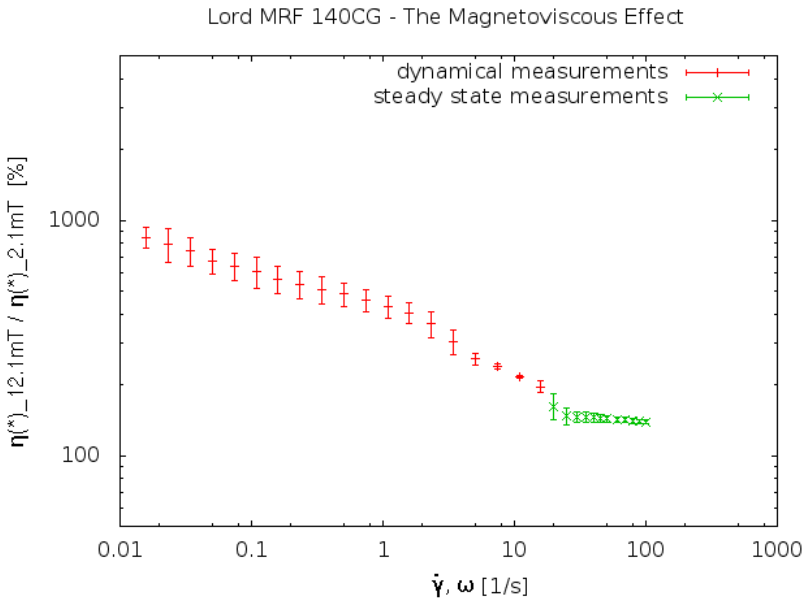

Figure 5.12: The dependence of the ratio $\eta_{12.1mT}/\eta_{2.1mT}$ on the shear rate $\dot{\gamma}$ (so-called magnetoviscous effect) using both the oscillatory (red) and steady-state shear flow (green) measurements. Computed using the Cox-Merz rule, Fig. 5.10, for magnetorheological fluid Lord MRF 140CG.

5.3 Magnetorheological behavior of APG513a OLD

In the magnetic cell the ferrofluid APG513a was measured in a parallel plate geometry (MR) within the linear regime (unless stated otherwise). This elder production line, which typically contains an increased amount of larger magnetite particles with diameter over 12 nm, was examined using steady-state shear and oscillatory shear mode as well as time-dependent measurements. The measurements were repeated several times due to technical problems with the Rosensweig instability, which operatively changes the amount of fluid under the plate and decreases the measured moment virtually. An overview of the flow curves $\tau(\dot{\gamma}, \vec{B})$, viscosities $\eta(\dot{\gamma}, \vec{B})$ and normal stresses differences $[N_1 - N_2](\dot{\gamma}, \vec{B})$ is provided in the following. For each measurement a minimal 5 runs were proceeded for verification. But due to inaccuracy in measuring geometry and due to instability of the fluid, very often more than 15 runs were needed. The measurements were sensitive to many factors. New samples were used for every run.

The flow curves $\tau(\dot{\gamma}, \vec{B})$ were measured for $|B| \in (0 - 67)$ mT, $\dot{\gamma} \in (1 - 1000)\,\mathrm{s}^{-1}$. The response to the magnetic field is not directly proportional to the magnetic field flux density. In Fig. 5.13 a complete overview is displayed. For slow and increasing shear rates $\dot{\gamma}$, the difference between the two shear stress responses $\tau(\dot{\gamma}, \vec{B})$ to the applied magnetic field flux densities increases. On the other hand, in the large shear rates regime, $\dot{\gamma} \in (200 - 1000)\,\mathrm{s}^{-1}$, this difference decreases with a decreasing field intensity and remains constant for larger

field intensities. The impact of the magnetic field on the shear stress (for smaller field flux densities (up to approx. 40 mT)) thus exhibits a maximum around $\dot{\gamma} \in (100 - 200)\,\mathrm{s}^{-1}$ or higher. Furthermore, with an increasing magnetic field flux density it the coupling to the shear rate is significantly weaker. We cannot rule out a maximum at higher shear rates, since this would lie outside the measurement range.

In Fig. 5.14, a detailed view is provided. In this figure a narrower range of shear rates, up to 100 s^{-1}, is shown and we can see the influence of the magnetic field on the shear stress response. Between 0 and 19 mT, and also between 43 and 54 mT, we can see a significant change in the response. Such changes can be caused by the formation of chain structures, which are not rigid enough for low fields and are thus destroyed due to the strain. In the second case, of stronger fields (43 and 54 mT), the chain structures are already built and can be characterized using a spacial ratio of these structures - the anisotropy level. Therefore, especially for these fluids, the experiment must be conducted with great care and the direction of shear rate change (increase or decrease) presents an important variable in the experiment. Concerning the ferrofluid APG513a OLD, no influence on the flow curves was observed.

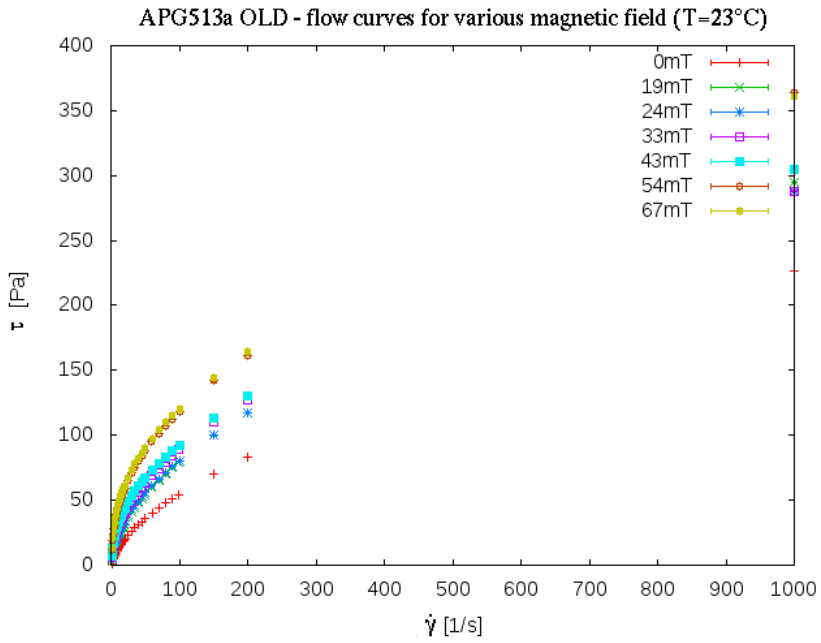

Figure 5.13: The flow curves $\tau(\dot{\gamma})$ of APG513a OLD for various magnetic field strengths, at 23°C.

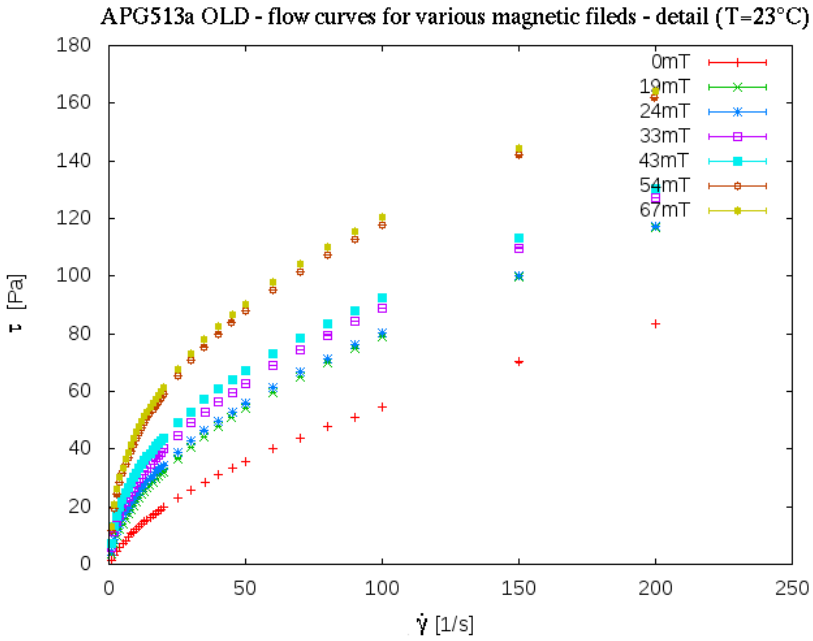

Figure 5.14: Detailed flow curves $\tau(\dot{\gamma})$ for APG513a OLD for various magnetic field strengths, at 23°C.

The obtained flow curves $\tau(\dot{\gamma})$ allow for the recovery of the viscosity. The relation between shear stress and viscosity is the rheological relation which is expected to obey the laws derived in chapter 2, Eq. (2.19). Because these are experimental viscosity curves $\eta(\dot{\gamma})$, the Cross model was used first to examine the course of the shear rate functions. The fitted viscosities are depicted in Fig. 5.15. The model was fitted for the experimental viscosity dependence on the shear rate in Fig. 5.16 - the fitted Cross model coefficients, Eq. (3.5),

$$\frac{\eta - \eta_\infty}{\eta_0 - \eta_\infty} = \frac{1}{1 + (K\dot{\gamma})^n},$$

are in Tab. 5.3.

The experimental viscosity curves $\eta(\dot{\gamma})$ show, that as in the case of magnetorheological fluid Lord MRF 140CG the power-law index stays in a narrow interval for any magnetic field applied. In this case the power-law index $n \in (0.6 - 0.8)$ which is a typical value for a fluid with larger, longer molecules (here with chains as well). The consistency coefficient increases with the increasing magnetic field and the fluid is then more shear-thinning under the influence of magnetic fluid.

Table 5.3: Cross model coefficients according to Eq. (3.5)

B [mT]	K [Pa.s^n]	n [-]
0	0.032 ± 0.002	0.860 ± 0.073
19	0.143 ± 0.028	0.694 ± 0.044
24	0.277 ± 0.046	0.657 ± 0.024
33	0.282 ± 0.061	0.713 ± 0.040
43	0.249 ± 0.027	0.771 ± 0.029
50	0.745 ± 0.097	0.699 ± 0.013
54	0.917 ± 0.092	0.667 ± 0.008
67	1.314 ± 0.166	0.662 ± 0.009

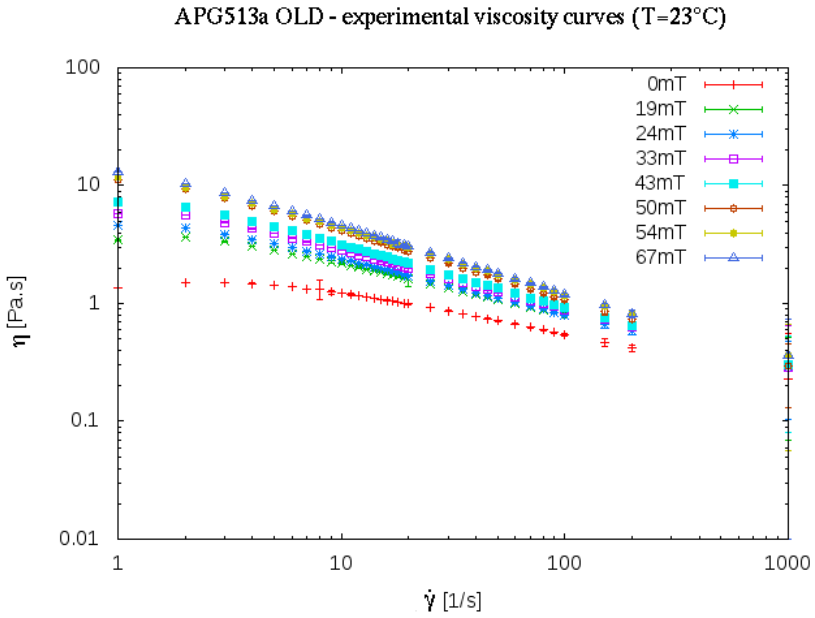

Figure 5.15: The viscosity curves $\eta(\dot{\gamma})$ of APG513a OLD for various magnetic field strengths and shear rates, at 23°C.

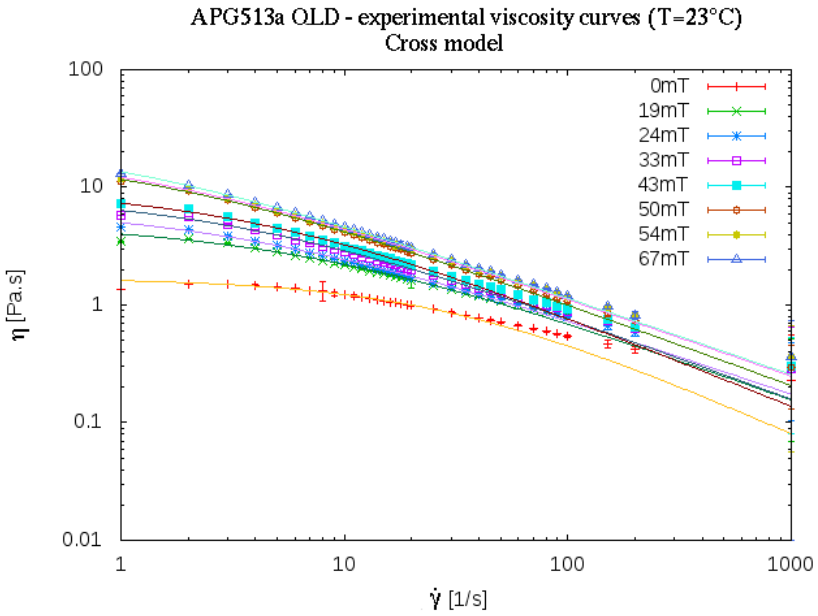

Figure 5.16: The viscosity curves $\eta(\dot{\gamma})$ of APG513a OLD for different magnetic field strengths and shear rates, at 23°C. The Cross model coefficients for the model curves are summarized in Tab. 5.3.

Next, the magnetoviscous effect for the APG513a was calculated. This experimental curves are obtained as ratio between viscosity of the fluid exposed to magnetic field to viscosity of the fluid in absence of the magnetic field (so-called reference viscosity). The magnetoviscous effect is displayed in Fig. 5.17. The magnetoviscous effect is quite strong for this liquid and reaches 800 % for lowest shear rate $\dot{\gamma} = 1\,\mathrm{s}^{-1}$ and strongest field B= 33 mT.

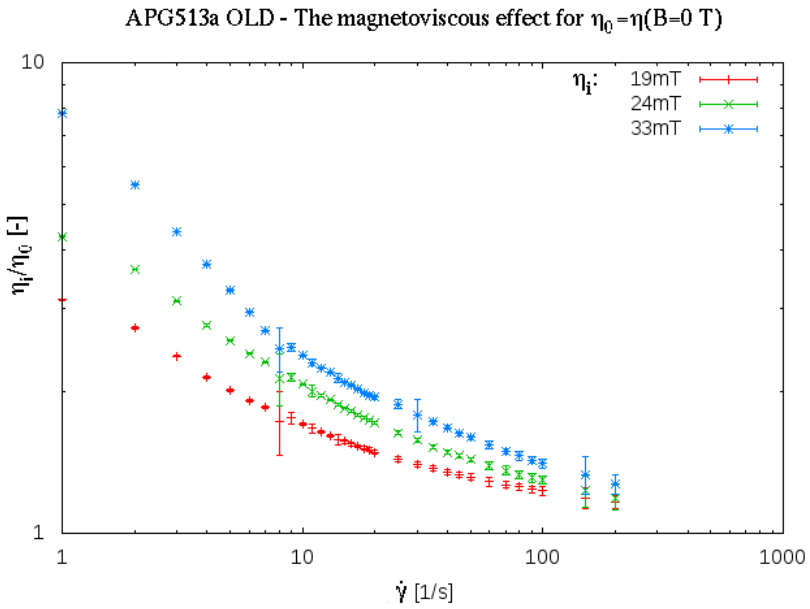

Figure 5.17: The magnetoviscous effect - the viscosity ratio η/η_0 in dependence on shear rate $\dot{\gamma}$ for ferrofluid APG513a OLD at 23°C. Viscosity η varies from 19mT (red), 24 mT (green) to 33mT (blue). The reference viscosity η_0 is the viscosity measured at megantic field absence (vis Fig. 5.16)

.

The fluid was further exposed to normal force measurements. This experiment was more difficult compared to the shear stress measurement. There are multiple reasons for this. For instance, the experiment is very sensitive to any variation of the gap between the parallel plates and there are also Rosensweig instabilities within the ferrofluid, when it is exposed to a magnetic field. These instabilities change the normal force locally and must be avoided for the measurement of the normal stresses differences. This means, that the free surface of the fluid has to be eliminated. For a parallel plate measuring geometry, the side of the sample has a free surface. We have thus employed a shallow cup, cut into the bottom plate. Next, the measured force is rather low in comparison to that of the fluids measured above (polymer PEO 5wt% aqueous solution and magnetorheological fluid Lord MRF 140CG). The measurement must therefore be calibrated very carefully and all secondary processes in the fluid will have a strong effect on the measurment. The fluid is also a better heat conductor (and therefore the measurement errors described in Chapter 3 play a more significant role, vis Fig. 3.4, Fig. 3.5 and further reading in Olagunju, [26]). Therefore, the gap must be estimated in accordance to the temperature variation and constraints given by the precession of the MR geometry. The gap between the plates was determined as $h = 0.5$ mm.

The results of the normal stresses differences $N_1 - N_2$ measurement are provided in Fig. 5.18.

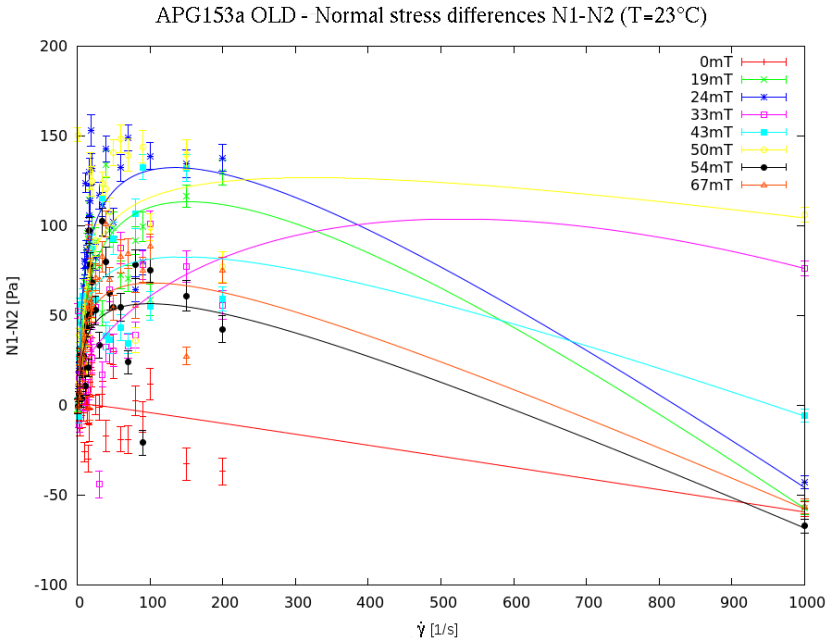

Figure 5.18: Normal stress difference $N_1 - N_2$ in dependence on shear rate $\dot{\gamma}$ in ferrofluid APG513a OLD at 23°C

In Fig. 5.18 we can observe the effect of constant contribution of the magnetic field flux density to the second normal stresses difference N_2 - according to the derived theory, the trace part of the stress tensor contributes a constant term BH - Eq. (2.18), where H is the magnitude of the applied magnetic field intensity and B the response of the material, the induced magnetic flux density. This response was previously observed in VSM measurement (in Fig. 4.4 and from experimental $M-H$ curve (fluid magnetization dependence on applied magnetic field intensity H) we arrive at a corresponding magnetisation function, Eq. (4.1). We can see that the magnetisation of the fluid in the range of $B \in (0-67)$ mT lies within an interval of $M \in (0-5)$ kA/m. Thus, the contribution of this constant term is significant and therefore, when a magnetic field is applied, the chains are formed within the fluid and contribute to the first normal stress difference N_1. However, they are destroyed at larger shear rates $\dot{\gamma}$ so that the constant in the term for the second normal stresses difference N_2 plays a more significant role. After the observed maximun, the entire experimental curve $N_1 - N_2$ decreases, as supported by our experiment.

For the normal stresses difference, a power-law model was also applied. This model was, however, adapted in order to reflect the theory, Eq. (2.18). Therefore a function of two terms was used where the first part accounts for the influence of N_1 (this term includes the bulk viscosity) and the second term describes N_2 and includes the constant term of magnetic field influence.

$$N_1 - N_2 = K_\alpha \dot{\gamma}^{n_1} + K_\beta \dot{\gamma}^{n_2} \tag{5.7}$$

This function was applied to the experimental $N_1 - N_2$ curves, but the fit was unstable.

Therefore, the first part, for which the first normal stress difference dominates the second part,

$$N_1 \gg N_2$$

was modeled separately. The power-law model was used:

$$N_1 = K_\alpha \dot{\gamma}^{n_1} \tag{5.8}$$

For this fit, shear rates $\dot{\gamma} \leq 40\,\mathrm{s}^{-1}$ were selected. The fit became unstable for the region of larger viscosities. From this part the power-law index n_1 was found to be very close to 1. On the basis of this result, the overall power-law model for the ferrofluid normal stress differeces can be described as

$$N_1 - N_2 = K_\alpha \dot{\gamma} - K_\beta \dot{\gamma}^{n_2}. \tag{5.9}$$

The model and experimental normal stress differences curves are displayed in Fig. 5.18 and 5.19.

In Fig. 5.18 we can observe the effect of a constant contribution of the magnetic field flux density to the second normal stresses difference N_2. This effect is in accordance with the derived theory, see Eq. (2.18). The term N_2 can rapidly change the course of the normal stress differences $N_1 - N_2$ because the value of Π_{33} contributes a constant BH term. The material response B can be obtained from the experimental curve (Fig. 4.3). Therefore the stronger the field is, the more the second normal stress difference N_2 will shift into the negative. In addition, this constant term in N_2 will play a more important role while the shear rate increases (the fluid is shear-thinning). All of these effect are supported by the experimental data, Fig. 5.18 and 5.19.

Model parameters fitted on the experimental curves are displayed in Tab. 5.3.

Table 5.4: Consistency coefficients K_α and K_β refering to normal stresses differences N_1 and N_2 and power-law index n_2 according to modified power-law model, Eq. (5.9).

B [mT]	K_α [Pa.s]	K_β [Pa.s^{n_2}]	n_2 [-]
0	-0,063 ± 0,074	-1,024 ± 91,90	0,193 ± 11,93
19	-0,365 ± 0,095	-43,92 ± 33,31	0,291 ± 0,132
24	-0,320 ± 0,069	-152,0 ± 183,0	0,140 ± 0,128
33	-2,250 ± 147,0	-3,842 ± 122,0	0,927 ± 4,570
43	-0,174 ± 0,107	-37,56 ± 91,80	0,221 ± 0,355
50	-0,072 ± 0,057	-606,0 ± 3230	0,031 ± 0,155
54	-0,198 ± 0,072	-64,39 ± 157,0	0,151 ± 0,276
67	-0,196 ± 0,052	-170,0 ± 503,0	0,080 ± 0,202

Tab. 5.4 shows some interesting results. The power-law index n_2 varies for this ferrofluid and model between 0.1 - 0.3 (excluding extreme values) and refers thus to a shear thinning

fluid with longer moleculs (chains). The index is not very sensitive to the magnetic field intensity. This value is however only one-third of the value for the shear stress mode. This means that the fluid is more shear-thinning in the normal direction than in the shear direction.

The consistency coefficients are one order higher than in the shear stress measurement and are negative. The consistency coefficient K_α is comparable to its value for shear stress direction and refers to the same attribute of the fluid as in the shear direction. However, the second consistency coefficient K_β is larger. The precision of this quantity was low. The fluid is more rigid with increasing K_β.

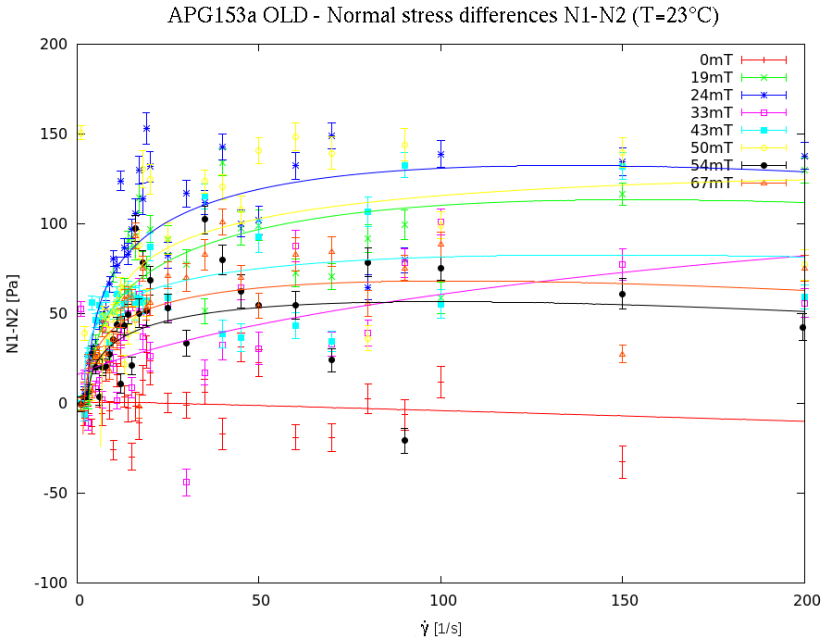

Figure 5.19: Normal stress difference $N_1 - N_2$ in dependence on shear rate $\dot{\gamma}$ and model functions, Eq. (5.9),in ferrofluid APG513a OLD at 23°C

To obtain a complete characterization of the normal stresses in the ferrofluid APG513a OLD, time-dependent measurements were conducted. These include dynamical shear and creep experiments.

An increased accuracy was achieved for the oscillatory experiments. This is very advantageous for the application of the Cox-Merz and Laun rules. A complete shear experiments better accuracy is held. Therefore, this experiment is very suitable for the use of the Cox-Merz and Laun rules. We have measured the complex shear modulus, with the storage and loss parts, and, thereby, also obtained the complex viscosity. These experiments were conducted at several different temperatures to extend the frequency range and also the shear strain window using the Cox-Merz and Laun rules. However, the temperature range is constrained by the rheometer properties and the fluid specifications. The rheometer was not capable (at the time of the experimental work) to cool down the sample below 10°C.

Furthermore, the fluid cannot be heated above 50°C, so that we end up with a usable temperature range of $T \in (15 - 40)\,°\mathrm{C}$. The temperature increments were chosen to be 5°C because this presents a good compromise between the number of measurement and the possibility to apply the time-temperature superposition principle (3.8).

For the creation of the master curve, in accordance to the William-Landau-Ferry equation and the time-temperature superposition principle, Eq. (3.8), the reference temperature $T_0 = 25°\mathrm{C}$ was chosen. The master curves were plotted with Gnuplot. To determine the accuracy, the $a_T(T)$ plot is depicted in Fig. 5.22 and a fit results in the function

$$a_{Tfit}(T) = 9.85x^{-0.07} - 6.72. \tag{5.10}$$

In Fig.(5.20), which covers the storage modulus G', and in Fig.5.21, which covers the loss modulus G'', the field induced change of the flow regime is clearly observed - for zero field, the fluid is fully in the flow regime, without an elastic element (as expected). For an increasing magnetic flux density, the regime is shifted towards the rubbery plateau and elastic ascension. Both the storage and loss moduli increase, as will be shown below.

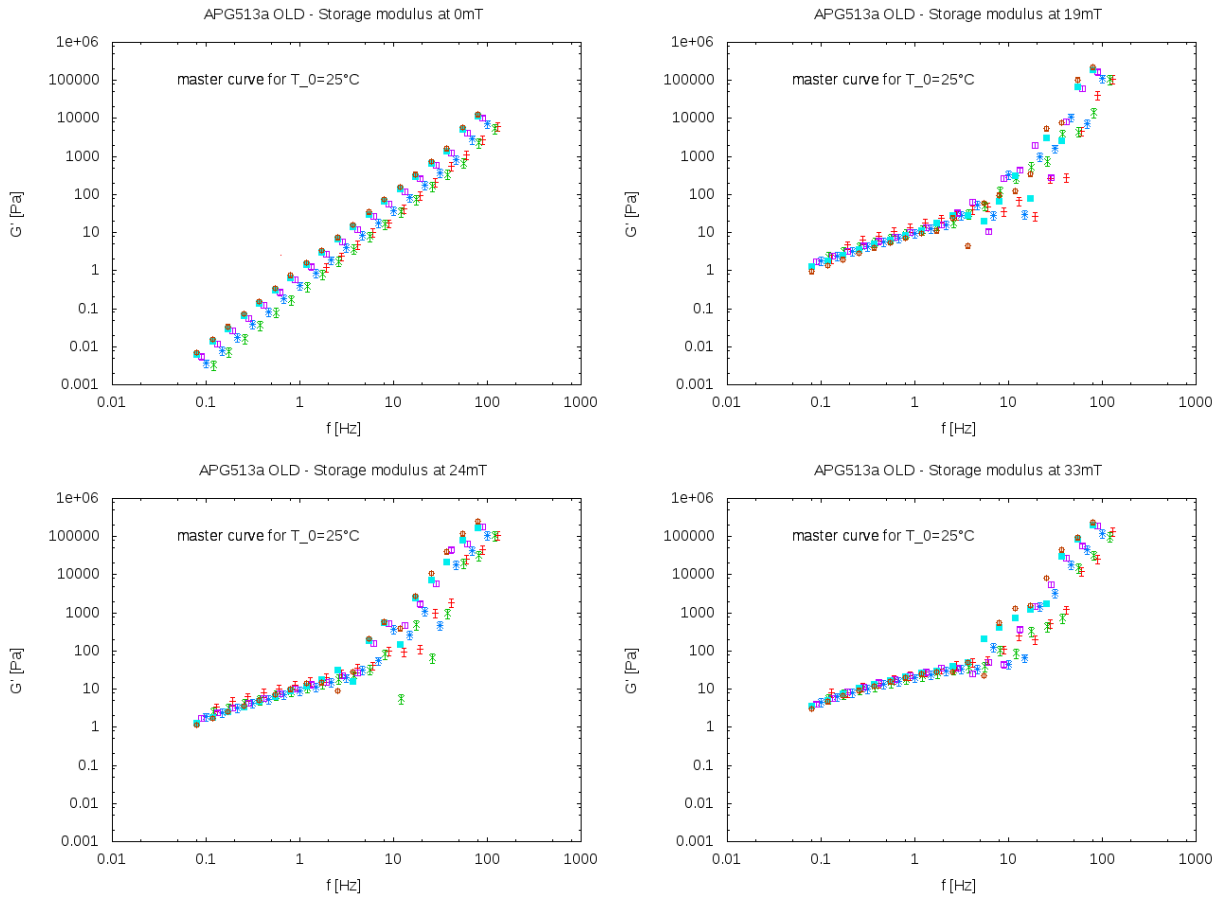

Figure 5.20: Master curves of the storage modulus G' in dependence on the magnetic field, at a reference temperature $T_0 = 25°C$. The fluid APG513a OLD was used. From left to right the master curves of G' in magnetic flux densities of B=0, 19, 24 and 33 mT.

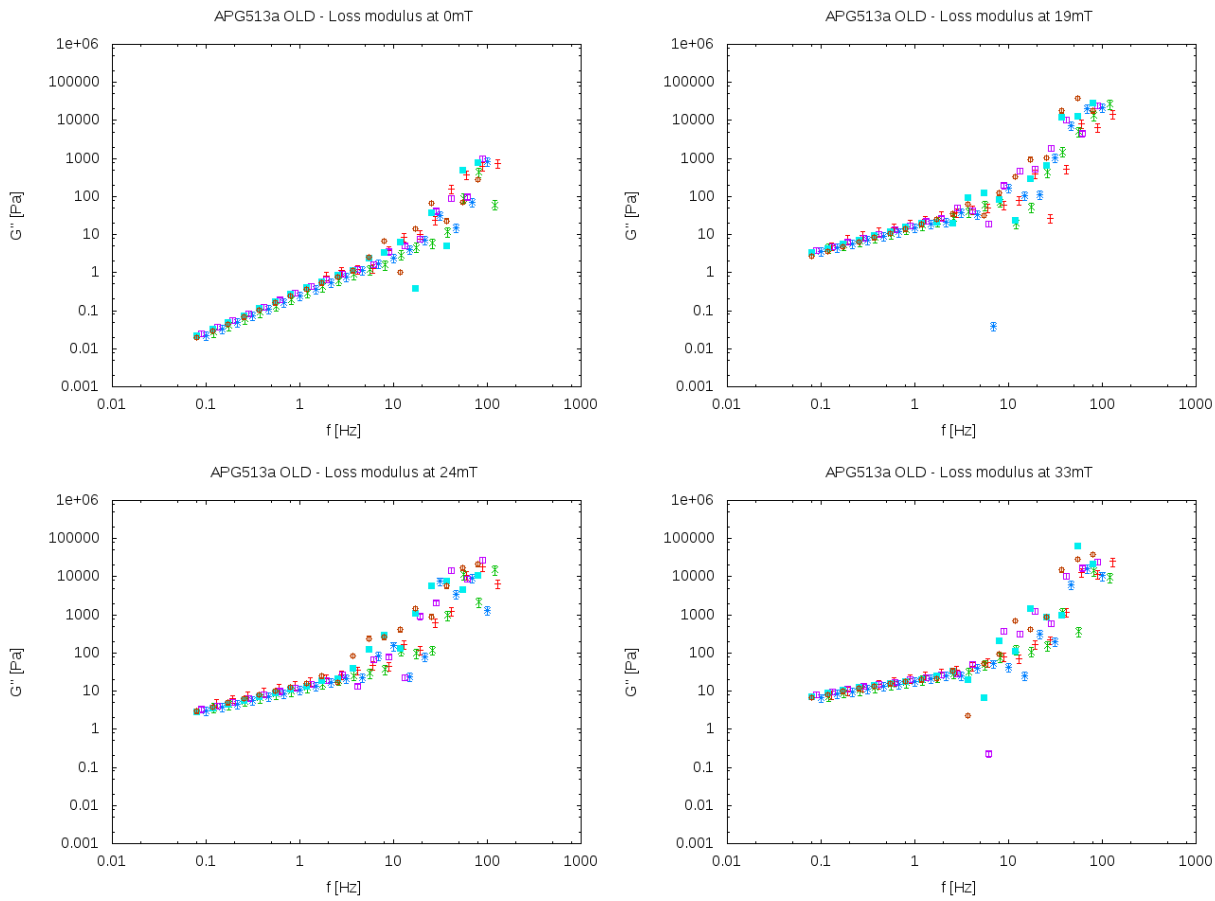

Figure 5.21: Master curves of the loss modulus G'' in dependence on the magnetic field, at a reference temperature $T_0 = 25°C$. The fluid APG513a OLD was used. From left to right the master curves of G'' in magnetic flux densities of B=0, 19, 24 and 33 mT.

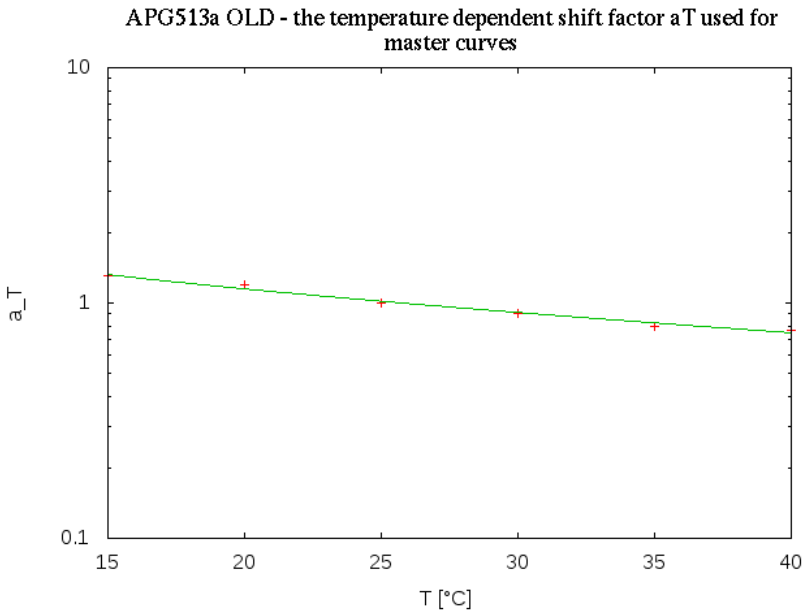

Figure 5.22: The shift factor a_T in dependence on the temperature for APG513a OLD, according to Eq. (5.10).

The master curves can be compared with each other and used to express the influence of the magnetic field. The comparison is provided in Fig. 5.23 for the different magnetic flux densities used in experiment. The storage and loss moduli are displayed for every magnetic flux density - it is interesting to observe, that the curves for the magnetic flux densities 19 mT and 24 mT are simply overlapping each other within the range of lower frequencies. Therefore, the mechanical properties of the fluid remain unchanged within this region.

Fig. 5.24 shows the comparison of the storage and loss moduli changes in the field. Only the minimal and maximal fields were chosen in the interest of lucidity. It can be observed, that the ferrofluid shifts from the flow regime at 0 T to a rubbery state at 33 mT.

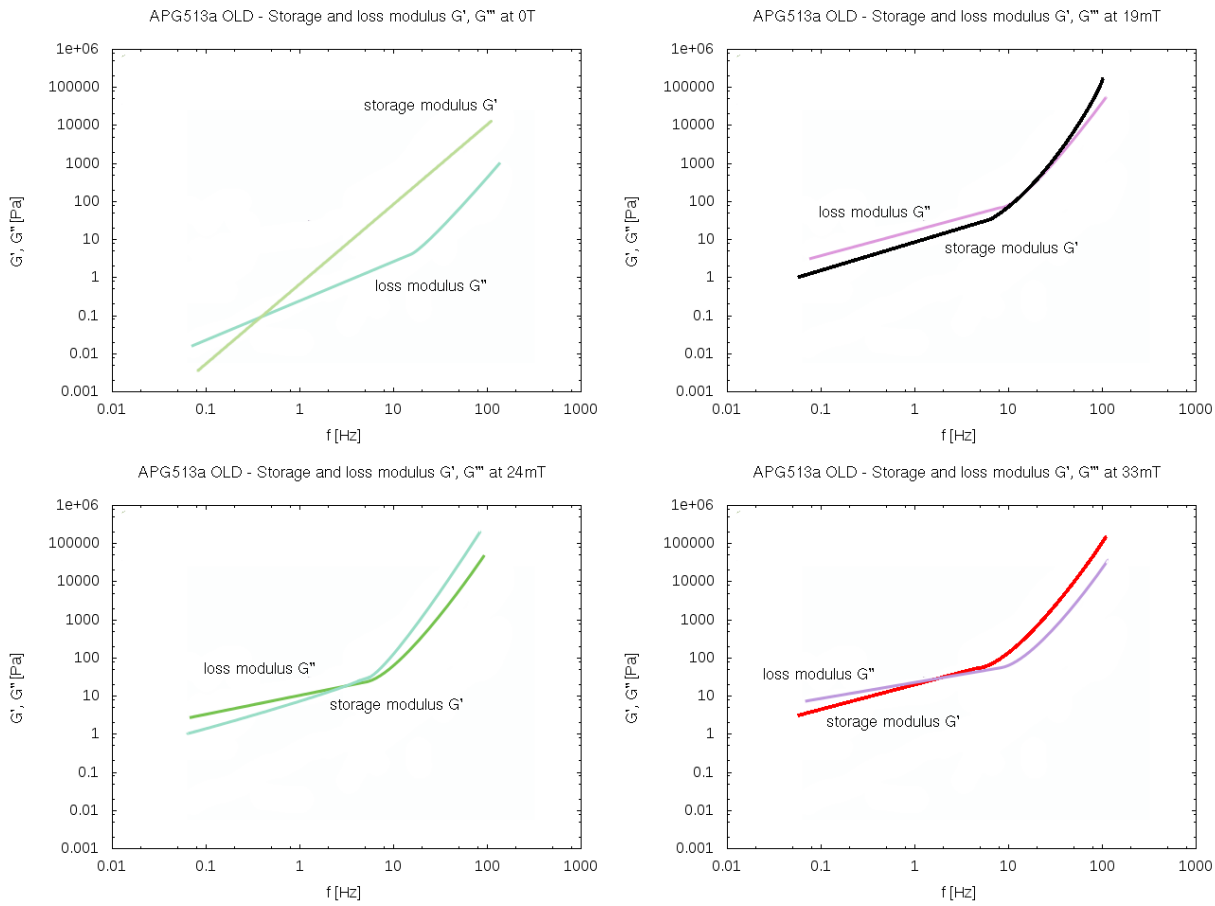

Figure 5.23: Master curves of the storage and loss moduli (G' and G'') in dependence on the magnetic field, at a reference temperature $T_0 = 25°C$. The fluid APG513a OLD was used. From left to right the master curves of G' and G'' in magnetic flux densities of B=0, 19, 24 and 33 mT.

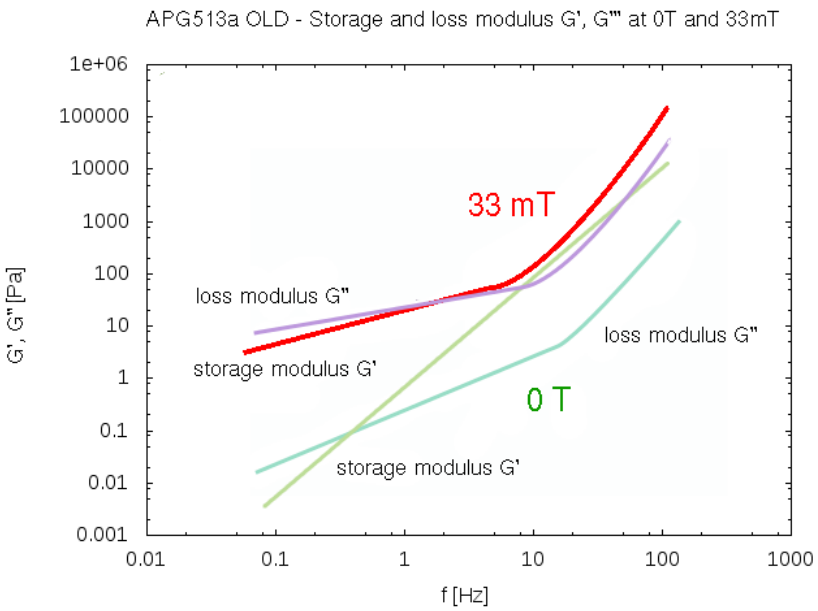

Figure 5.24: Master curves of the storage and loss moduli (G' and G'') without a magnetic field in light and dark green, respectively, and for $B = 33$ mT in red and purple, respectively. The reference temperature was $T_0 = 25°C$. The storage and loss moduli are displayed in dependence on magnetic field. The fluid APG513a OLD was used.

On the basis of the oscillatory measurements, the semi-empirical Cox-Merz rule can be applied. In accordance to the theory, Eq. (3.67), the plots in Fig. 5.25, and 5.26 express this rule. The accordance of both viscosities can be found within the range of errors for shear rates $\dot{\gamma} \in (1 - 100)\,\mathrm{s}^{-1}$. Hoever, the data obtained by steady-state shear experiments do not exhibit the same quality discussed above. The data obtained by steady-state shear experiments follow the same trend as the data obtained by the dynamical experiments within the given interval of shear rates (excluding the experiment done without any magnetic field presence). The experimental viscosity curves obtained in stead-state and dynamical mode for zero magnetic field display opposite trends. The experimental viscosity curve $\eta(\dot{\gamma})$ obtained from the dynamical measurements expresses the shear-thickening property while, in contrast, the experimental viscosity curve obtained from steady-state measurements expresses the shear-thicking property. With the Cox-Merz rule, we obtain the viscosity for lower shear-rates than $\dot{\gamma} = 1\,\mathrm{s}^{-1}$ and are therefore able to observe the same trend here. In the magnetic field, both experimental curves exhibit the shear-thinning property for avnarrow window of shear-rates $\dot{\gamma} \in (1 - 100)\,\mathrm{s}^{-1}$ and, subsequently, with an increase of the shear rate the behavior of the viscosity obtained by steady-state and dynamical measurements begin to differ. The experimental viscosity curve in steady-state mode exhibits the shear-thinning property for any shear-rate measured and any magnetic field applied (compare with Fig. 5.16). The experimental viscosity curve in dynamical mode exhibits a different behavior. For shear-rates above approx. 100 s^{-}1 the curves reache a local minimum and then begins to increase for increasing shear rates (the shear-thickening property).

Therefore, both curves differs in this range of higher shear rates.

This different behavior could be caused by the progress of the experiment. For steady state mode, the ferrofluid is exposed to a constant shear rate for longer periods of time (tens of seconds, minutes). It is probable, that in this time the fluid can relax (as we show later, the relaxation times for time-dependent experiments are very large, about tens of seconds, see Tab. 5.5). The chain formation and other processes are in equilibrium and the final viscosity value is the equilibrated viscosity as well.

The dynamical mode is different. The fluid is exposed to harmonicaly changing strain and the response of the fluid - shear stress is then measured for periods of applied frequency. The anisotropic strain in the fluid is thus very different from the strain in the steady state mode. The nanoparticles in the fluid can change the stress field strongly and thus change the reponse of the fluid for higher frequencies, where these bodies are not capable to move with the high frequency. According to the Cox-Merz rule, the values of viscosity for larger shear rates are compared with values of viscosity for larger frequencies. Thus, the difference increases with higher frequencies. When we compare the experimental viscosity curves for non-zero magnetic fields, the chain microstructure of the ferrofluid is still observed for larger shear rates / frequencies. Due to magnetic field, the chain structures form in the fluid and their rigidity increases with an increasing magnetic field intensity. Therefore the experimental viscosity curves differ very strongly for zero magnetic field and this difference decreases with an increase of the field intensity.

This result provides information on the magnetoviscous effect in the fluid and the experimental range of the applicability of the Cox-Merz rule.

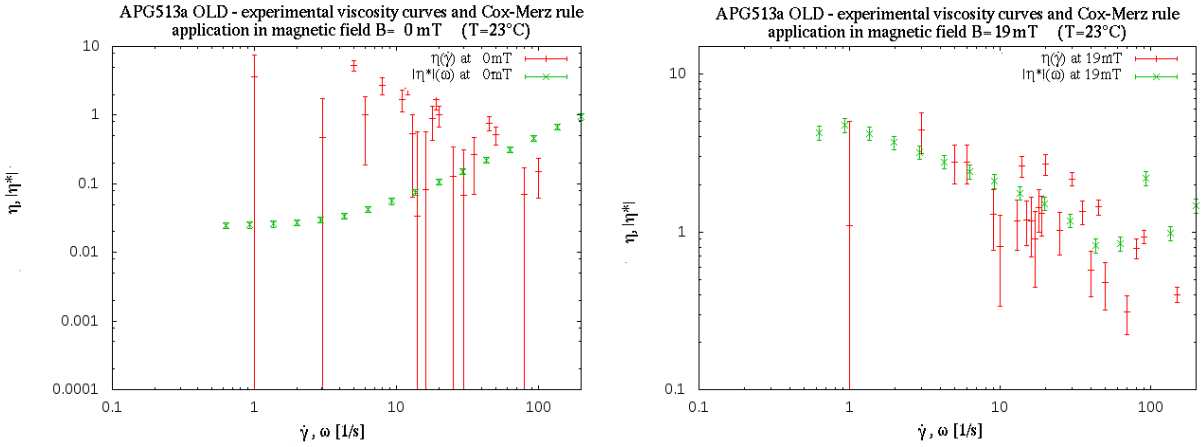

Figure 5.25: Experimental viscosity curves $\eta(\dot{\gamma})$ and $|\eta * |(\omega)$ in dependence on $\dot{\gamma}$ and ω for ferrofluid APG513a OLD exposed to two magnetic flux densities (from left: 0T and 19mT, respectively)- the Cox-Merz rule (Eq. (3.67)) was applied for this comparison of steady state viscosity η and dynamical complex viscosity $\eta*$.

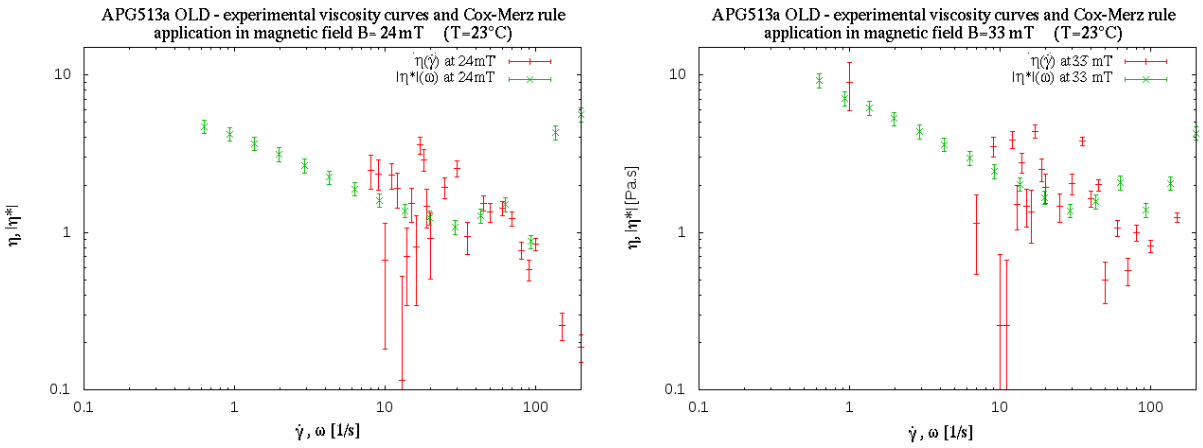

Figure 5.26: Experimental viscosity curves $\eta(\dot{\gamma})$ and $|\eta*|(\omega)$ in dependence on $\dot{\gamma}$ and ω for ferrofluid APG513a OLD exposed to two magnetic flux densities (from left: 24T and 33mT, respectively) - the Cox-Merz rule (Eq. (3.67)) was applied for this comparison of steady state viscosity η and dynamical complex viscosity $\eta*$.

The dynamical experiment was conducted in order to extend the shear rate window for normal stresses differeces. This can be done after the evaluation of the Cox-Merz rule range of applicability. The Laun rule can be then applied with the restrictions given by Cox-Merz rule [13].

As shown above, the Cox-Merz rule was applicable for APG513a OLD at magnetic flux densities of $B = 19$, 24 and 33 mT, respectively, and for shear rates $\dot{\gamma}$ in the range of 1 to 100 s^{-1}. In these ranges, the measured storage and loss shear moduli will be used in order to obtain the corresponding first normal stresses difference using Laun's rule. Subsequently, if we apply this rule for lower shear rates (up to 30-40 s^{-1}), the second normal stress difference N_2 is negligible in comparison to the first normal stress difference N_2 and thus the term $N_1 - N_2$ can be reduced to include N_1 only. Therefore, in the range of $\dot{\gamma} \in (1 - 40)\,\mathrm{s}^{-1}$ the values of N_1 are obtained by direct steady-state shear measurement and are compared with the N_1 values obtained from Laun's rule application on the dynamical measurement. In this range of shear rates a good accordance is therefore expected.

In contrast, for larger shear rates the second term N_2 cannot be neglected. The N_1 value obtained by the application of Laun's rule is compared with the $N_1 - N_2$ value obtained by direct steady-state shear measurements. This fact can be used for proof of the impact of the N_2 term on the $N_1 - N_2$ function of $\dot{\gamma}$ which was studied in theory (Eq.(2.18)) and steady state shear measurements (Tab. 5.4).

In Fig. 5.27 an overview of the application of Laun's rule to any measured magnetic field dependence of the normal stresses difference is displayed.

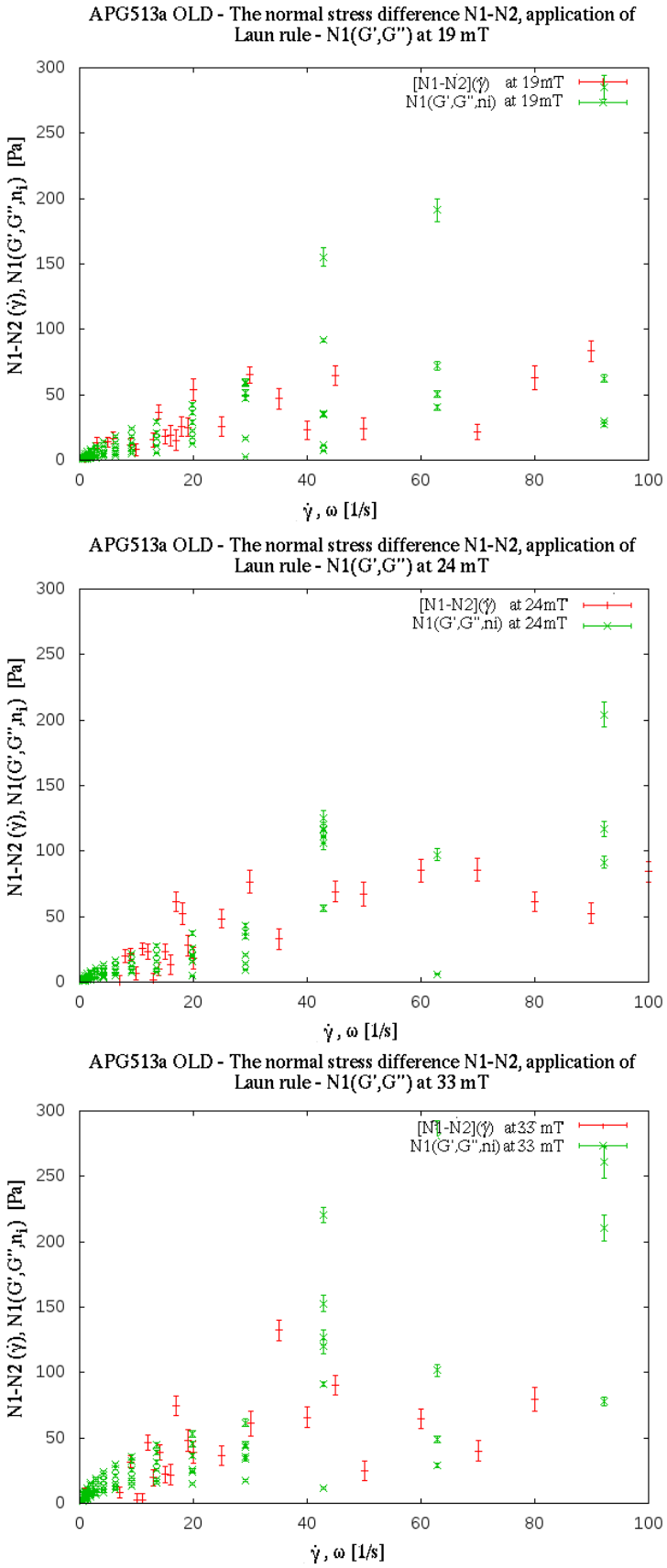

Figure 5.27: The comparison of normal stresses difference $N_1 - N_2$ from steady-state mode and $N_1 = 2G'[1 + (G'/G'')^2]^{n_i}$, where G', G'' are storage and loss moduli of the fluid, respectively. The index n_i is the power-law index for according magnetic filed as in the Tab. 5.4 for APG513a OLD at 23°C. The magnetic field varies from 19mT (top picture), 24mT (central picture) to 33mT (bottom picture).

The results obtained using Laun's rule are similar to the results obtained by Cox-Merz rule application. For lower shear rates, the experimental curves are correlate well qualitatively. The curves exhibit an increased correlation for stronger magnetic fields where the errors decrease and the curves approach each other. Because of the restricted range of shear rates, however, this process cannot give us new information for lower shear rates about the normal stress differences. As it was shown above, the second normal stress difference N_2 plays a role for shear rates larger than approx. 30-40 s^{-1}. In the range $\dot{\gamma} \in (50 - 100)\,s^{-1}$ the experimental curves are expected to differ due to the contribution of the term N_2. This is observable for magnetic flux densities B=24 and 33 mT but the shear rate window is restricted to values below $\dot{\gamma} = 100\ s^{-1}$ and thus we cannot obtain information about the N_2 term for higher shear rates.

The application of Laun's rule thus confirms qualitatively that the N_2 term is not negligible any longer for larger shear rates and that it even reaches values larger than the first normal stress difference N_1. However, due to the restrictions on the shear rate range no additional information besides the qualitative interpretation can be obtained.

The time-dependent measurements are completed with the creep experiment. According to the theory of viscoelasticity and in correlation to the micro-structure of loaded materials, the creep experiments can be described by the Burgers model among others (used mainly for the experimental data was fitted using the function

$$\gamma(t) = \tau \left[J + J_1 \left(1 - e^{-\frac{t}{t_\tau}} \right) + \frac{t}{\eta} \right] \tag{5.11}$$

The experiments were conducted under a stress of τ =50 Pa. The creep curves provided in Fig. 5.28.

Table 5.5: Coefficients of creep function (Burgers model, Eq. (5.11) for creep experiment done with ferrofluid APG513a OLD at 23°C

B [mT]	J [Pa^{-1}]	J_1 [Pa^{-1}]	t_τ [s]	η [Pa.s]
19	0,016 ± 0,003	-1,790 ± 0,044	17,889 ± 0,988	1,164 ± 0,001
24	0,010 ± 0,003	-1,667 ± 0,048	21,740 ± 1,234	1,250 ± 0,001
33	0,015 ± 0,013	-2,653 ± 0,121	27,771 ± 1,980	1,702 ± 0,003
43	0,012 ± 0,014	-1,526 ± 0,055	29,338 ± 1,565	2,138 ± 0,002
54	0,022 ± 0,011	-0,709 ± 0,021	21,453 ± 1,250	3,506 ± 0,003
67	0,015 ± 0,002	-1,097 ± 0,021	24,377 ± 0,848	4,130 ± 0,004

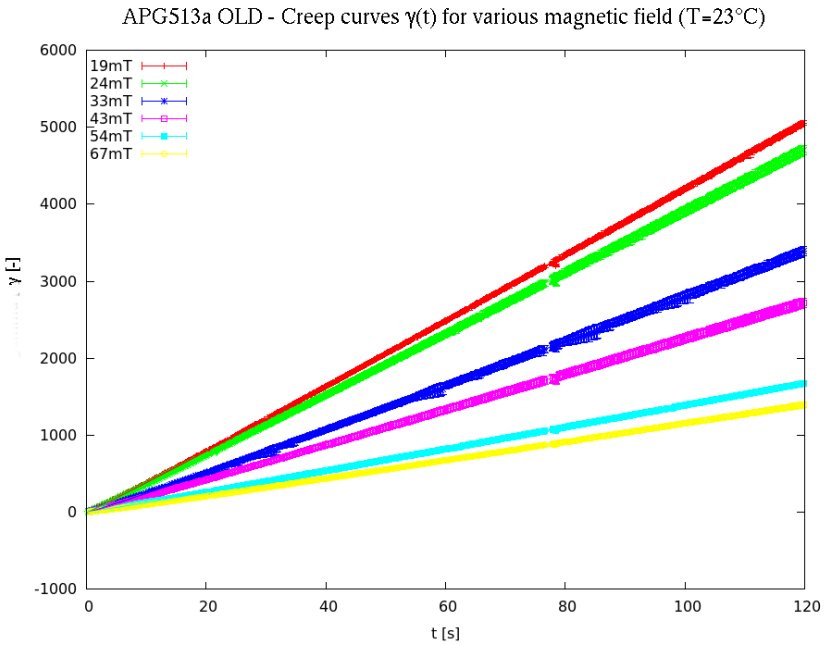

Figure 5.28: Creep experiment (strain dependence on applied shear stress $\gamma(\tau)$) at a shear stress $\tau = 50$Pa for ferrofluid APG513a OLD at 23°C exposed to magnetic flux densities from 19mT (red) to 67mT (yellow).

Very good accordance is found by this model at viscosity estimation. These viscosities can be compared with the viscosities obtained in the steady-state shear experiment at corresponding magnetic fields. A very good correlation of the two data sources is observed. The influence of the magnetic field is interesting - the curves form three groups which are separated by larger intervals. This is in accordance to steady-state measurements, where the same behavior was observed (vis Fig. 5.14). This behavior, which is similar for steady-state and time-dependent measurements, expresses a connection to a change in microstructure during the measurement. The structure is strongly dependent on the applied strain and at a specific point the equilibrated structure is no longer strong enough and is subsequently destroyed by the strain. However, for higher fields the structures are again sufficiently rigid, as is evident from the stress or strain response.

This behavior is also evident in the observed relaxation times. The relaxation time (the velocity of system response) increases with an increasing field, however, after a specific point it decreases again. The relaxation time definitely provides an important characteristic of the system. It even reaches tens of seconds which has a parallel in polymer systems where these relaxation times correlate with short chain parts relaxations. Such long relaxation times express the elastic behavior again and specify the scale on which the fluid is rigid and the scale on which the fluid can flow (after the relaxation time).

The main result of this part is then the multilateral character of the ferrofluid. As is evident from the shear axis, the fluid behaves as expected because the ratio of the elastic part to the viscous part increases with an increasing magnetic field. In the normal direction,

however, the fluid flows more freely for stronger magnetic fields. A different behavior of fluid for different time scales was found. From dynamical measurements, fluid becomes shear-thickening according to complex viscosity for higher frequencies which is in contrast to steady-state measurements. For a Cox-Merz rule application, only a narrow window of correspondence was found. In this range, on the other hand, fluid behaves very similarly to the steady-state shear mode, which supports the duality of the view and allows us to apply the Cox-Merz and Laun rules in a given range. Due to the narrow temperature window we were not able to extend the shear rates sufficiently to allow for an application of Laun's rule and to obtain additional results of qualitative behavior of second normal stress N_2. It was, however, possible to demonstrate that this is generally possible and it can be applied in the future.

The creep experiments served as further evidence to the observation, that the fluid is very specific. The shear modulus is very low and the fluid is polymer-like during the measurement. The ferrofluid in our experimental setup flows after a rather long relaxation time which can reach up to 30s. Based on this, the fluid can be considered more elastic than viscous and this property is very closely connected to the magnetic flux density. Therefore the ferrofluid exhibits many contrary attributes depending on the external parameters. Therefore, the ferrofluid anisotropy is very strong and this opens up a variety of applications in practice. Furthermore, it should serve to ignite further studies in the future.

Conclusion

This thesis provides a rheological approach to the study of ferrofluids. The work was focused on the normal stress differences in sample ferrofluids and their variation under the influence of an external magnetic field. To achieve this goal the following steps were taken:

- a magnetic cell, containing a set of adjustable permanent magnets, was designed to be used with a Haake Mars III rheometer
- a bottom plate for both a cone-and-plate and a parallel plate measuring geometry was designed
- a prototype of the measuring geometry in the parallel plate arrangment, the MR plate, was obtained
- the magnetic cell and measuring geometries were calibrated with silicon oils and subsequently tested using a PEO 5 wt% aqueous solution

These tests have shown that, with the installed magnetic cell and in the specific measuring geometry, the rheometer is able to measure in shear mode, steady-state mode and dynamical mode and can produce comparable result for the normal stresses differences. In the dynamical mode, precise curves were obtained for various magnetic field strengths and this demonstrated the usability of the device designed for magnetic field-dependent measurements of the normal force.

To allow for the application of the Cox-Merz and Laun rule for the ferrofluid/magnetofluid, which enable an extension of the measuring window for the normal stress differences, measurement of the magnetorheological fluid Lord MRF 140CG was used. This measurement:

- proved the ability of the measuring device/setup to obtain comparable results for magnetic fluids : Lord MRF 140CG was examined in shear steady-state mode and dynamical mode and the obtained results showed a good qualitative accordance with literature values
- showed, that the Cox-Merz and Laun Rules are applicable for the magnetic fluid and work very well for this sample by extending the measurement window of normal stress differences by 4 orders of magnitude

The main measurements were conducted for the characterisation of the ferrofluid APG513a OLD. This fluid was tested in several ways. All the experiments were carried out at various magnetic field strengths to examine the magnetic field dependence.

- The flow curves $\tau(\dot{\gamma})$ for APG513a OLD were obtained and evaluated using the Cross model

- This measurement allowed for a determination of the ferrofluid attributes and magnetic field dependence in the shear direction (Tab. 5.3). When exposed to a magnetic field, the fluid behaves like a viscoelastic body with a low consistency coefficient in the range of (0.032 - 1.314) Pa.s$^{0.69}$ (increasing with an increasing magnetic field strength) and a constant power-law index $n = (0.691 \pm 0.014)$.

- The normal forces were measured, the normal stresses differences were obtained and evaluated using a power law model which was modified in accordance with the derived rheological model.

- Two processes were observed for the normal stress differences. They are interpreted as a chain building process and a process containing a constant magnetic field contribution term. A strong impact of second normal stress difference is almost certain (Tab. 5.4). In this case, the consistency coefficients are comparable to shear direction of measurement but the power-law indexes vary for first process around 1 and for the second one between 0.1 - 0.3. The dependence of the power-law indexes on the magnetic field was not observed.

- Dynamic experiments were conducted and experimental shear modulus curves were obtained. Master curves were recorded for a reference temperature of $T_0 = 25°\mathrm{C}$. In accordance to the theory [8] and previous tests with Lord MRF 140CG the Cox-Merz Rule was applied. From the results, the different time-dependent behavior of the ferrofluid was found. The Cox-Merz rule could be applied only in a range of $\dot{\gamma} \in (1 - 40)\,\mathrm{s}^{-1}$. A dependence of the magnetoviscous effect on the shear rate for an extended shear rate window (Fig. 5.17). The magnetoviscous effect reaches 800% for $\dot{\gamma} = 1\,\mathrm{s}^{-1}$ and a magnetic flux density of B=33 mT.

- In correlation with the Cox-Merz Rule, Laun's Rule was applied in a range of correspondence, $\dot{\gamma} \in (1 - 40)\,\mathrm{s}^{-1}$ and a window of the dependence of the normal stress difference on the shear rate was obtained (Fig. 5.27). From these experimental curves a non-neglectable negative second normal stress N_2 was found. This result confirms the theory (Eq. (2.18)).

- Time-dependent creep experiments were conducted and the Burgers model was applied. Application of the Burgers model allowed for a determination of the compliances and relaxation times. These exhibited further ferrofluid attributes - long relaxation times $t_\tau \in (17 - 29)\,\mathrm{s}$ concerning the elastic behaviour of the fluid and small compliances which decrease for an increasing magnetic flux density (Tab. 5.5). These relaxation times can be connected with relaxation of shorter parts of chains, built under the magnetic field influence. These results provide an extended insight on the ferrofluid behavior under various conditions.

- These results also express a strong anisotropy of the ferrofluid. A chain formation process and a strong magnetic field influence, which result in the anisotropy, have

been observed. The fluid behaves qualitatively different when studied in shear direction or normal direction and behaves very differently for different time frames.

In summary, this work contributes to the knowledge of ferrofluid, specifically concerning the microstructure. An anisotropy was evident under the influence of a magnetic field - the fluid behaves very differently in dependence on the different orientation of the acting force and on different measurement directions. The work has demonstrated the applicability of Laun's rule for such ferrofluids. Therefore, it can provide a basis for further development of rheological models and for the design of practical applications in the industry.

Bibliography

[1] Barnes, H.A., Hutton,J.F., Walters, K. *An Introduction To Rheology*, Elsevier, Amsterdam, 2005, 3. ed., ISBN 0-444-87140-3

[2] Brdička, M., Samek, L., Sopko, B. *Mechanika kontinua*, Academia, Praha, 2000, 2. ed., ISBN 80-200-0772-5

[3] Böhme, G. *Strömungsmechanik nicht Newtonscher Fluide*, Teubner, Stuttgart, 1981

[4] Odenbach, S., Rylewicz, T., Heyen, M.: A rheometer dedicated for the investigation of viscoelastic effects in commercial magnetic fluids. *J. Magn. and Magn. Mat., vol. 201* (1999)

[5] Carlson, J. D. *What makes a Good MR Fluid*, Nice: 8th International Conference on Electrorheological (ER) and Magnetorheological (MR) Suspensions (2001)

[6] Dang, A., Ooi, L., Fales, J., Stroeve, P. Yield stress measurements of magnetorheological [U+FB02]uids in tubes, *Industrial & Engineering ChemistryResearch 39*, (2000) 2269–2274.

[7] Gazeau, F., Baravian, C., Bacri, J.-C., Perzynski, R., Shliomis, M.I. Energy conversion in ferrofluids: Magnetic nanoparticles as motors and generators, *Phys. Rev. E 56* (1997) 614

[8] Al-Hadithi, T.S.R, Barnes, H.A., and K.Walters, The relationship between the linear (oscillatory) and nonlinear (steady-state) flow properties of a series of polymer and colloidal systems. *Colloid and Polymer Science, 270* (1992) 40-46.

[9] Kim, Y.S., Kim, Y.H. Application of ferro-cobalt magnetic fluid for oil sealing, *Journal of Magnetism and Magnetic Materials 267*, (2003) 105–110.

[10] Kulicke, W.M., Kiss, G., Porter, R.S., Rheometers for Molten Plastics, *Rheol. Acta 16*, (1977) 568-597.

[11] M.I.Kolte, H.K.Rasmussen, O.Hassager. Transient filament stretching rheometer II: numerical simulation, *Rheol. Acta 36* (1997) 285–302.

[12] Ladouani, A., Nemdili, A. Experimental Study of Effects of Polymer Additives on the Performance of a Centrifugal Pump, *SCIENTIFIC BULLETIN of the "POLITEHNICA" University of Timişoara, Romania* (2004) 205-210

[13] Laun, H.M. Prediction of elastic strains of polymer melts in shear and elongation. *J Rheol 30* (1986) 459–501

[14] Lesieur, S., Grabielle-Madelmont, C., Menager, C., Cabuil, V., Dadhi, D., Pierrot, P., Edwards, K. Evidence of surfactant-induced formation of transient pores in lipid bilayers by using magnetic-fluid-loaded liposomes, *Journal of the American Chemical Society 125*, (2003) 5266–5267.

[15] *MRF-140CG Magneto-Rheological Fluid*, Lord Technical Data, 2008. Online available at: ftp://www.lara.unb.br/Projects/rleg/protese/materiais/rheo/LORD%20Magnetorheological/DS7

[16] Ch.W.Macosko. *Rheology - Principles, Measurements and Applications*, John Wiley and Sons, 1994

[17] Milner, S. Relating the shear-thinning curve to the molecular weight distribution in linear polymer melts. *Journal of Rheology, 40* (1996) 303

[18] Musacchio, S. *Effects of friction and polymers on 2D turbulence*, Torino: Universitá degli studi di Torino, 2003

[19] G.H.McKinley. Dimensionless Groups For Understanding Free Surface Flows of Complex Fluids, *Society of Rheology, Rheology Bulletin 74* (2005) 6-9.

[20] S. Odenbach (ed.). *Colloidal magnetic fluids : basics, development and application of ferrofluids*, Springer-Verlag, Berlin - Heidelberg, 2009, ISBN 97-835-4085-3862

[21] A. Zubarev. Statistical Physics of Non-dilute Ferrofluids *in* S. Odenbach (ed.). *Ferrofluids : magnetically controllable fluids and their applications*, Springer-Verlag, Berlin - Heidelberg, 2002, ISBN 97-835-4043-9783, p. 143 - 161

[22] S. Odenbach, S. Thurm. Magnetoviscous Effects in Ferrofluids *in* S. Odenbach (ed.). *Ferrofluids : magnetically controllable fluids and their applications*, Springer-Verlag, Berlin - Heidelberg, 2002, ISBN 97-835-4043-9783, p. 185 - 201

[23] Odenbach, S., Störk, H. Shear dependence of field-induced contributions to the viscosity of magnetic fluids at low shear rates, *Journal of Magnetism and Magnetic Materials Vol.183* (1998) 188-194

[24] Pop, L.M., Odenbach, S. Investigation of the microscopic reason for the magnetoviscous effect in ferrofluids studied by small angle neutron scattering, *J. Phys.: Condens. Matter 18* (2006) 2785–2802

[25] Olagunju, D.O., Cook, L.P., McKinley, G.H. Effect of viscous heating on linear stability of viscoelastic cone-and-plate flow: axisymmetric case, *J. Non-Newtonian Fluid Mech. 102* (2002) 321–342

[26] Olagunju, D.O. Secondary flow in non-isothermal viscoelastic parallel-plate flow, *J. of Engineering Mathematics, Vo. 51, No. 4* (2005) 325-338

[27] Papathanasiou, T.D. Explicit Corrections for the Effect of Viscous Heating in Circular Couette Viscometers, *International Journal of Thermophysics, Vol. 19*, (1998) 71–88.

[28] Pinarbasi, A., Muharrem, I. Viscous heating effects on the linear stability of Poiseuille flow of an inelastic fluid, *J. Non-Newtonian Fluid Mech. 127*, (2005) 67-71

[29] Pop, L.M., Hilljegerdes, J., Odenbach, S., Wiedenmann, A. The microstructure of ferrofluids and their rheological properties, *Applied Organometallic Chemistry 18*, (2004) 523–528.

[30] Rahn, H., Inmaculada Gomez-Morilla, I., Jurgons, R., Alexiou, Ch.,Eberbeck, D., Odenbach, S. Tomographic examination of magnetic nanoparticles used as drug carriers, *Journal of Magnetism and Magnetic Materials 321* (2009) 1517–1520

[31] Raikher, Y.L., Stepanov, V.I. Nonlinear dynamic susceptibilities and [U+FB01]eld-induced birefringence in magnetic particle assemblies, *Advances In Chemical Physics, Vol.129* (2004) 419-588

[32] Reimers, M. J. *Sliding Plate Rheometer Studies of Concentrated Polystyrene Solutions*, McGill University, Montréal, 1996

[33] R.E. Rosensweig. Basic Equations for Magnetic Fluids with Internal Rotations from S. Odenbach (ed.). *Ferrofluids : magnetically controllable fluids and their applications*, Springer-Verlag, Berlin - Heidelberg, 2002, ISBN 97-835-4043-9783

[34] Scherer, C., Figueiredo Neto, A.M. Ferrofluids: Properties and Applications, *Brazilian Journal of Physics, vol. 35* (2005) 718-727

[35] Shliomis, M.I. Ferrohydrodynamics: Retrospective and Issues, from S. Odenbach (ed.). *Ferrofluids : magnetically controllable fluids and their applications*, Springer-Verlag, Berlin - Heidelberg, 2002, ISBN 97-835-4043-9783

[36] G. Schramm. *Introduction to Practical Viscometry*, Buchler Instruments, Frankfurt, 1987

[37] C.Tropea, A.L.Yarin, J.S.Foss. *Handbook of Experimental Fluid Dynamics*, Springer-Verlag, Berlin - Heidelberg, 2007

[38] Wiśniewski, A. The Possibility of use of the magneto-rheological fluids in armours, *Biuletyn naukowy Problemy techniky uzbrojenia No. 117* (2011) 169-176

List of Tables

List of Figures

Attachments

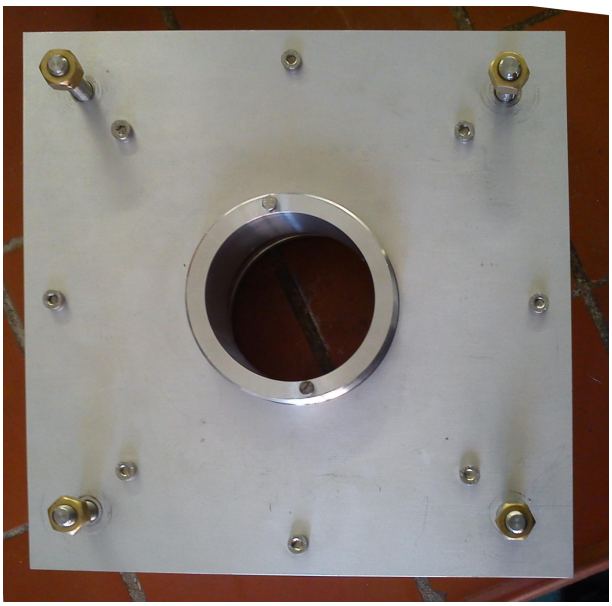

Figure 5.29: My designed magnetic cell - top view

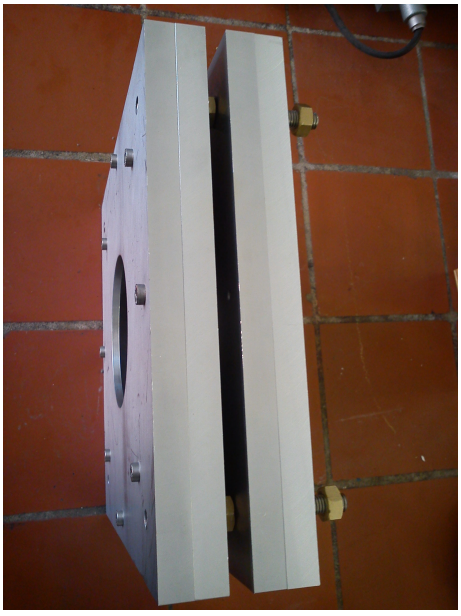

Figure 5.30: My designed magnetic cell - side view

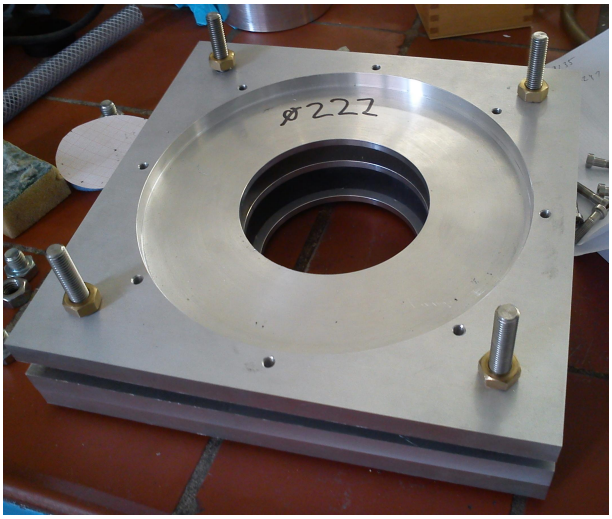

Figure 5.31: My designed magnetic cell - top view, placing of one F30 magnet

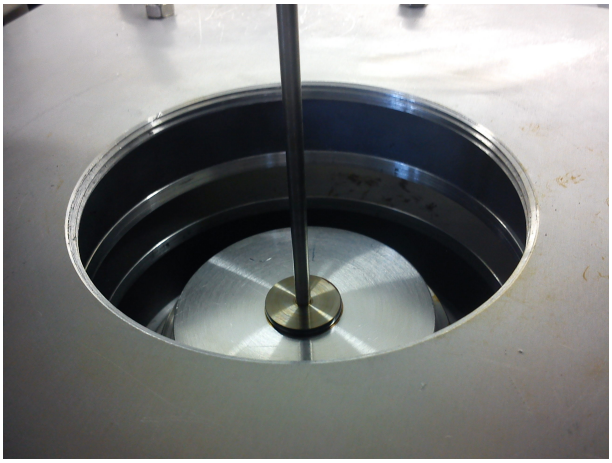

Figure 5.32: My designed magnetic cell, measuring geometry MR and custom base plate

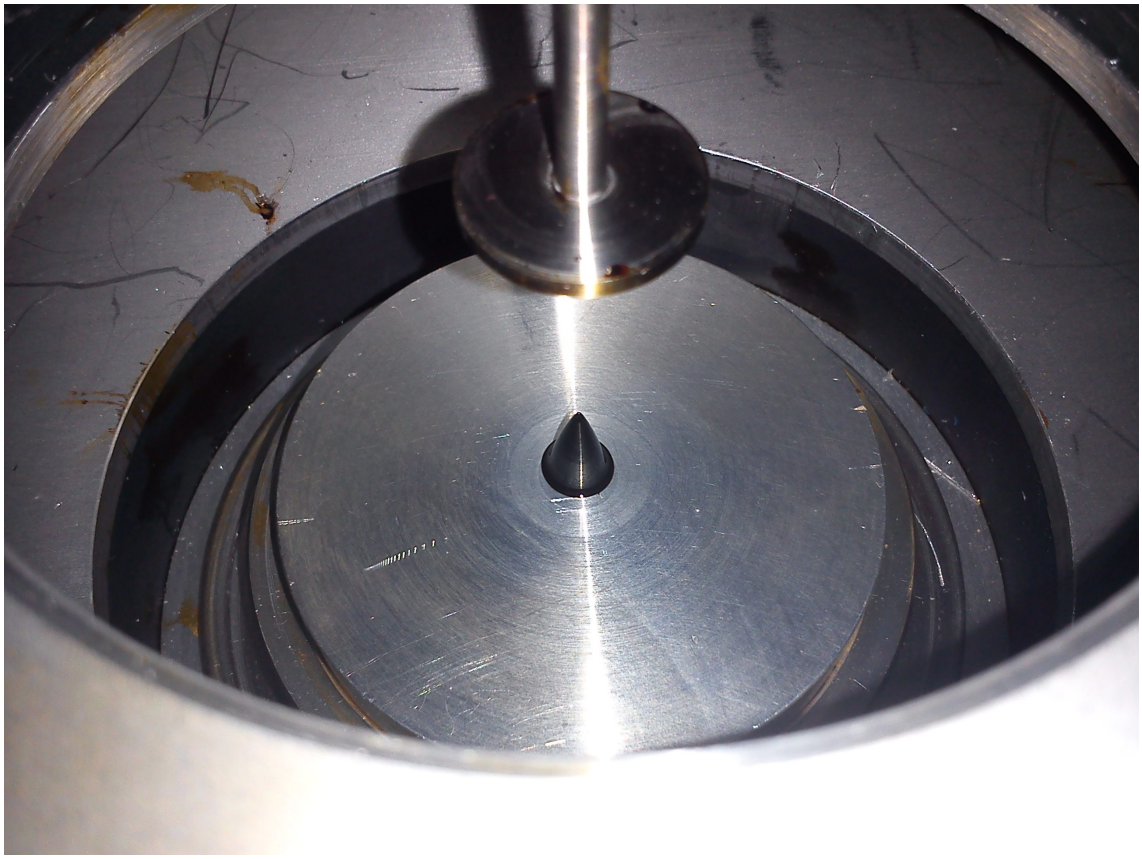

Figure 5.33: Sample of ferrofluid APG513a OLD - one droplet in a homogeneus magnetic field (an example of Rosensweig instability)

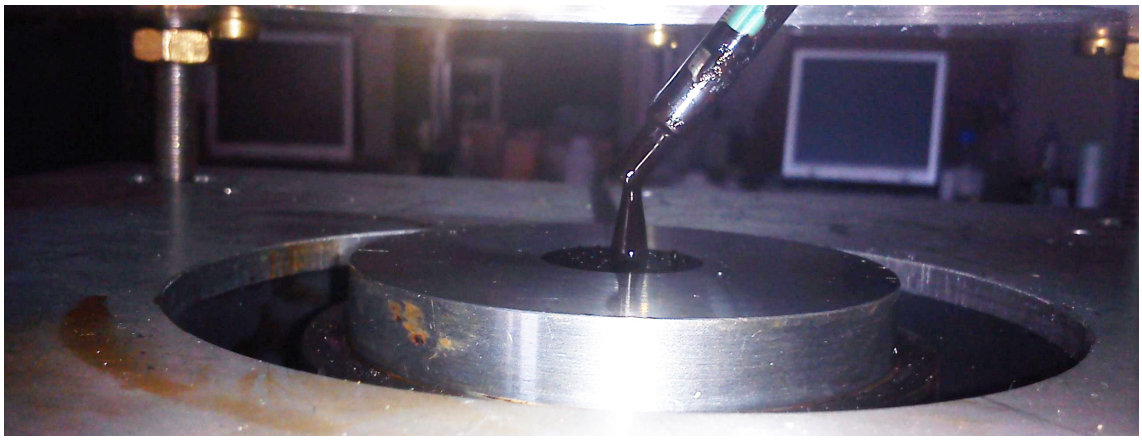

Figure 5.34: Sample of ferrofluid APG513a OLD - practical problems to leave the droplet in the measuring area

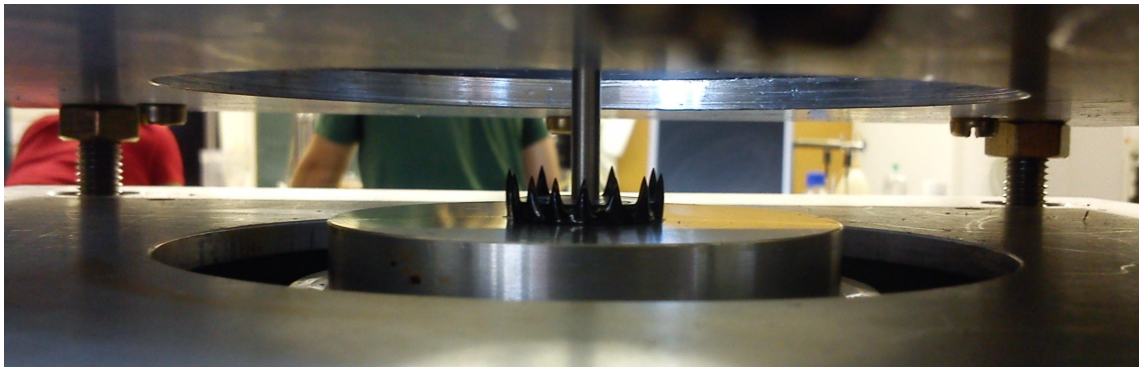

Figure 5.35: Rosensweig instabilities during measuring of ferrofluid APG513a OLD in magnetic field - side view

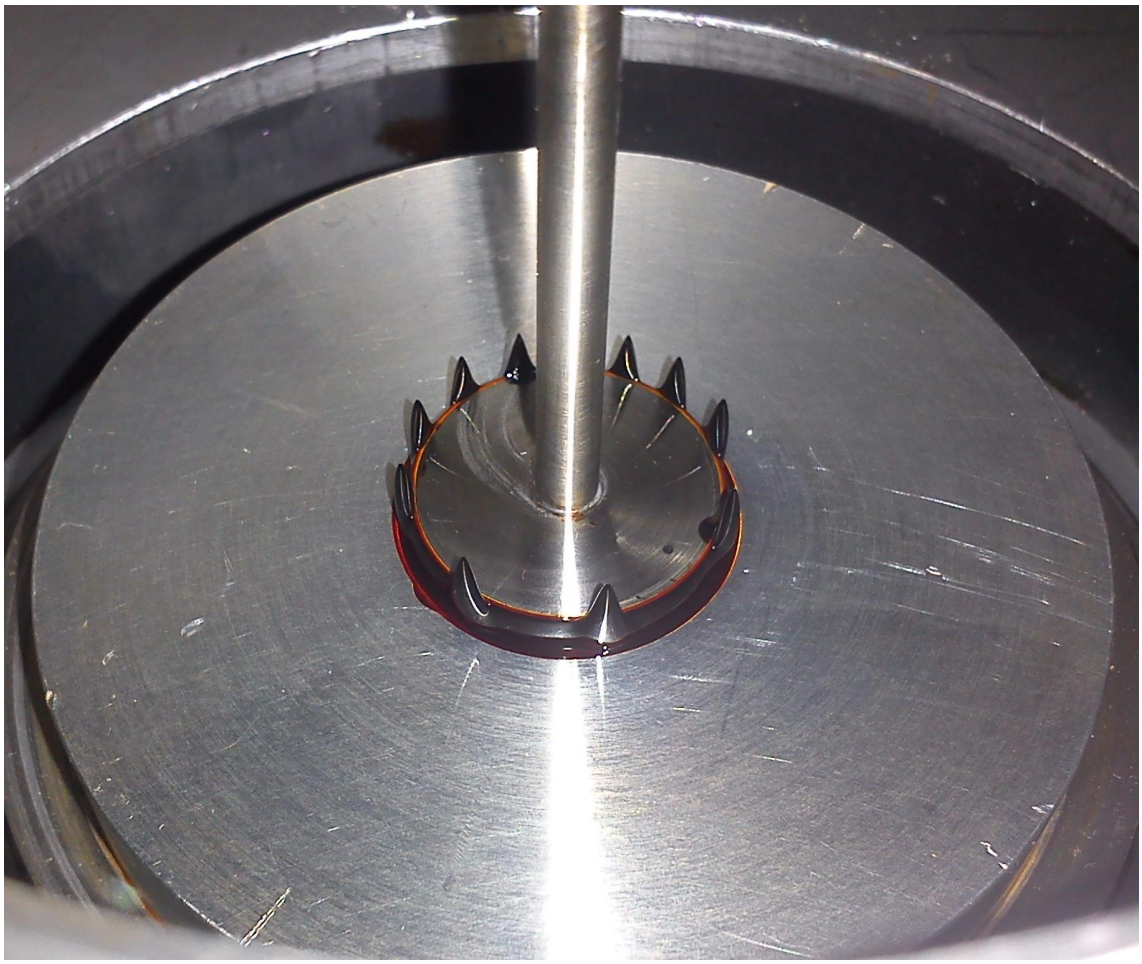

Figure 5.36: Rosensweig instabilities during measuring of ferrofluid APG513a OLD in magnetic field - top view